Title	A Study on Rudder-Bulb-Fin System Applied to KVLCC2 Tanker in Calm Wate
Author(s)	Truong, Quang Tho
Citation	大阪大学, 2019, 博士論文
Version Type	VoR
URL	https://doi.org/10.18910/73581
rights	
Note	

Doctoral Dissertation

A Study on Rudder-Bulb-Fin System Applied to KVLCC2 Tanker in Calm Water

TRUONG QUANG THO

July 2019

Graduate School of Engineering

Osaka University

CONTENTS

List of symbols

IMO	International Maritime Organization
ESDs	Energy-Saving Devices
ITTC	International Towing Tank Conference
NMRI	National Maritime Research Institute
ZB-F	Twisted Rudder-Bulb with Fins
JMU	Japan Marine United Corporation
MHI	Mitsubishi Heavy Industries
RBFS	Rudder-Bulb-Fin System
CFD	Computational Fluid Dynamics
EFD	Experimental Fluid Dynamics
LNG	Liquefied Natural Gas
LPG	Liquefied Petroleum Gas
KVLCC2	KRISO Very Large Crude Carrier 2
L_{PP}	Length between Perpendiculars
B_{WL}	Breadth at water line
D	Depth of Ship
	Propeller diameter
T	Draft (fully loaded condition)
∇	Displacement
C_B	Block coefficient

C_M	Mid-ship section coefficient
A_e/A_0	Expanded blade area ratio
CFDShip-Iowa	The CFD code developed by Iowa University
USURP	Unique Surfaces Using Ranked Polygons
FP	Fore Perpendicular
AP	Aft Perpendicular
r_{hub}	Hub radius
RANS	Reynolds-Averaged Navier-Stokes
DES	Detached Eddy Simulation
ASM	Algebraic Stress Model
PISO	Pressure-Implicit Splitting Operator
BET	Blade Element Theory
DOF	Degree of Freedom
Re	Reynolds number
Fn	Froude number
g	Gravitational acceleration
$f_{b_i}^*$	Non-dimentional body-force vector
f_{b_i}	Force per unit volume
ρ	Water density
ν	Kinematic viscosity
L	Length of ship
U_0	Inlet velocity

U_r	Resultant inflow velocity at propeller plane
U_t	Tangential velocity at propeller plane
β_i	Hydrodynamic pitch angle
w_t	Tangential induced velocity at propeller plane
C_L, C_D	Lift and drag coefficient
k_1	Correction coefficient for blade-to-blade interaction
r_e	Radius of the representative blade section
R'	Propeller radius
α	Angle of attack
α_0	Zero lift angle
dL	Sectional lift force
dD	Sectional drag force
dT	Sectional thrust
dQ	Sectional torque
fb_x	Body-force component in x-direction
fb_θ	Tangential body-force
T	Propeller thrust
Q	Propeller torque
N	Number of propeller blade
n	Number of propeller revolution
Δx	Grid spacing in x-direction
H	Pitch of blade

H_e	Effective pitch of blade
S-PIV	Stereoscopic Particle Image Velocimetry
AOA	Angle of Attack
NACA	National Advisory Committee for Aeronautics
m	Maximum ordinate of the mean line in fraction of the chord
p	Chord-wise position of m
(x_c, y_c)	Abscissa and ordinate of point on the mean line
c	Chord
(x_u, y_u)	Upper points of a wing section
(x_l, y_l)	Lower points of a wing section
2D	Two Dimensional
3D	Three Dimensional
y_t	Thickness distribution of a wing section
t	Thrust deduction
$1\text{-}w$	Wake fraction
η_H	Hull efficiency
E%, D%	Comparison error
R	Total resistance
R_T	Total resistance with propeller
R_0	Total resistance without propeller
C_t	Resistance coefficient
A	Total surface wetted area

J	Advance coefficient (V_a/nD)
J_a	Advance ratio on advanced speed
J_s	Advance ratio on Ship speed
K_Q	Torque coefficient
K_T	Thrust coefficient
P_D	Delivered power
η_D	Quasi-propulsive efficiency
η_H	Hull efficiency
η_o	Propeller open water efficiency
η_R	relative rotative efficiency
ψ	Trim angle
z/L_{PP}	Trim at fore perpendicular (non-dimentionalized by L_{PP})
L1	Distance between AP and rotating center
P	Pressure
Q	Q-criterion
Ω_{ij}	Vorticity tensor
S_{ij}	Rate-of-strain tensor
GB	Gigabytes
OpenMPI	Open source Message Passing Interface

List of tables

List of figures

CHAPTER 1: INTRODUCTION

The energy, materials, food and industrial products required for human living have been transported almost by sea transport. Therefore, shipbuilding industry plays an important role in operating the transportation networks. Grasp the reality of the situation, many companies in the world have built series types of cargo ship to meet the needs of the marketplace. However, with the rapid advent of number of new ships, it has led a number of difficulties such as complex system or environmental pollution. An increasing number of ships in the world has resulted in the degradation of the quality of air and seawater. This is due to the fact that the amount of carbon dioxide emission released from ships and industries has increased significantly as well as the rapid exhaustion of the earth's natural resources and the increase of fuel price. From this urgent situation, it is indeed necessary to create a vessel with lower carbon emission and better fuel efficiency that directly leads to reduce costs in the process of operation as well as contribute to protecting the global environment. It became the springboard and the true inspiration for researchers and developers in shipbuilding industry field. Thus, several kinds of energy-saving devices (ESDs) around ship stern place are developed and introduced by companies as well as researchers at universities for a few recent decades. Although the researchers or designers have the different methods, it normally leads to the same purpose; that is, to reduce the requirement power for ship which directly leads to reduce costs in the process of operation as well as contribute to protecting the global environment.

The International Towing Tank Conference report (ITTC 2017) cited from International Maritime Organization (2009) that about 28 % of propulsion can be lost before it is delivered to the propeller shaft for a small cargo ship. Recommendations of the ITTC lead to proposal methods for energy-saving devices in mainly reducing total resistance and propeller efficiency. The ITTC also presents a comprehensive introduction and various methods in order to increase the efficiency of vessel.

Hoang et al. (2009) researched about skin-friction drag reduction using an active method, i.e. gas injection. The research was focused on the effect of air lubrication method on frictional resistance reduction using a real ship-cement carrier Pacific seagull with both ballast and fully loaded conditions. A long slender model was also conducted at National Maritime Research Institute (NMRI) towing tank to prepare indispensable parameters for real ship experiment. The experiment showed that total resistance could be decreased at the maximum of 11% for ballast condition and 6% for fully loaded condition by using air lubrication (i.e. 7% and 4% energy-savings, respectively).

Nguyen et al. (2016) presented several types of rudder with small changing at trailing edge; four rudder models with different wedge shapes; wedge10-beta30, wedge10-beta45, wedge10-beta60 and wedge10-beta30a (in which the first number represents wedge width and the other is angle of wedge) were designed and simulated using a commercial code, Ansys Fluent. The remark was added that when increasing the wedge angle, the drag could be reduced meanwhile the value of lift/drag ratio increased. The wedge10-beta60 rudder gives smaller drag and higher lift/drag ratio compared to the other cases.

Kim et al. (2014) developed a ZB-F twisted rudder for a 320m long container ship at 20knots by viscous simulation. They pointed out that the rudder-bulb should not be installed together with contra-rotating propellers as well as propeller boss cap tip. The bulb-fin not only improved the effective wake but raised the propulsive efficiency by 2.95% as well.

JMU (Japan Marine United) and MHI (Mitsubishi Heavy Industries, Ltd) designed a counter-rotating propeller that consists of two propellers (rotation about the same axis in opposite directions). A grim wheel was proposed using the central part (turbine shaped) to drive the outer propeller portion. The propulsive efficiency was improved by recovering the energy loss due to rotational flow behind propeller.

The “ultimate rudder” was developed by Nakashima Propeller Co., Ltd. The RANS simulation was performed using a commercial CFD code (CRADLE SCRYU/Tetra) with unstructured grids. The rudder-bulb extends upstream and close to propeller boss, using a system that is designed in order that the rudder can be easily rotated. The results of this research show that the hub vortex can be eliminated mostly and the improvement of hull efficiency was 4.1% compared with the conventional rudder.

Obtaining the best combination of low resistance and high propulsive efficiency is also one of the goals that we are heading. Generally, this can be attained by proper matching of the ship hull, engine, and propeller or by combination of several ESDs. There are some possible technical devices that can be decrease significant emissions but may not in high economic efficiency. The author focused on ESDs for reducing the energy loss as well as gaining extra thrust from propeller rotational flow. The rudder-bulb is known as a popular ESD device for a long time ago in every corner of the shipbuilding industry field whereas Rudder-Bulb-Fin system (RBFS) is still as relatively new concept. A few kinds of research about RBFS had been reported recently. Kawasaki heavy industries, Ltd. has offered a Rudder-Bulb system with fins, the energy-saving effect of which achieves approximately 2%-7% and had been already applied on many real ships including LNG (liquefied natural gas), LPG (liquefied petroleum gas) and bulk carriers. Matsumoto and Sakamoto (2009) also succeeded in about 2% fuel consumption reduction with a patent dressing a finned rudder. The location of port fin is higher than starboard's one and the fin length for both sides is not as long as the propeller radius. Among their designs, one type of port side fin was designed with an upward inclination. Compared with the conventional rudder; the experiment showed that the ship required less horsepower in maintaining the same speed.

The objective of present study is to create and develop the Rudder-Bulb-Fin geometry designed for KVLCC2 tanker as one of the energy-saving devices. The results of this dissertation will convincingly proof the benefits of Rudder-Bulb-Fin system and its improvement. The dissertation is arranged in 5 chapters. The dissertation begins with a chapter of brief introduction about the current situations in shipbuilding field and researches related to ESDs.

Chapter II describes the methodology which is used in this research with its boundary conditions. The explanations on the Osaka University propeller model and mesh generation are added in this chapter. The body-force propeller model which provides the propulsive force and required torque for the ship was used throughout this research. A brief introduction about Experimental Fluid Dynamics (EFD) using the KRISO Very Large Crude Carrier 2 which is often called KVLCC2 with a model scale of 1:100 is also provided, since the Computational Fluid Dynamics (CFD) result is validated against the EFD data in order to have an authenticity of the research. Both CFD and EFD have the same test conditions. The experiment was conducted at Osaka University towing tank with fully loaded condition at Froude number of 0.142 correspond to the 3.2m long ship model.

Chapter III presents the methodological approach of this research and the reason why it is necessary to improve the system through the fundamental principle of prediction.

Various comprehensive fin geometries in adjusting angle of attack, changing mean camber line or thickness distribution are also presented with its shapes and dimensions. Several simulations with those different fin geometries were simulated by CFDShip-Iowa code.

The results are thoroughly analyzed in chapter IV for all the cases of rudder-fin and compared with EFD data. The detailed analysis of the self-propulsion factors and flow field in the vicinity of ship stern are given. Furthermore, various factors such as pressure distribution on rudder-fin, vortex shedding or flow separation on rudder-fin's surface are added in this episode. A huge flow separation region occurred under the starboard side fin around the middle span. The main hub vortex was found under the port side fin. These problems can be completely solved by the design of changing angle of attack, shape of fin and fin's location. The research proved convincingly the positive influence of fin's shape, angle of attack, thickness parameters on propulsion efficiency. The optimal designs were also discussed.

Finally, chapter V summarizes the salient features of the research and points out the necessary things that need to be done in the near future.

CHAPTER 2: METHODOLOGY - CFD AND EFD

2.1 Computational Fluid Dynamics

2.1.1 Ship Model

The ship model for simulation is KRISO Very Large Crude Carrier 2 which is often called KVLCC2 with a model scale of 1:100. The ship model was tested at a design speed of 0.795 m/sec which having the Froude number of 0.142. The model scale Reynolds number is 2.55×10^6. The 3-D hull of KVLCC2 model and the lines plan can be seen in Figure 2-1 and Figure 2-2. Also, primary dimensions of ship and propeller are listed in Table 2-1 below (SIMMAN 2008).

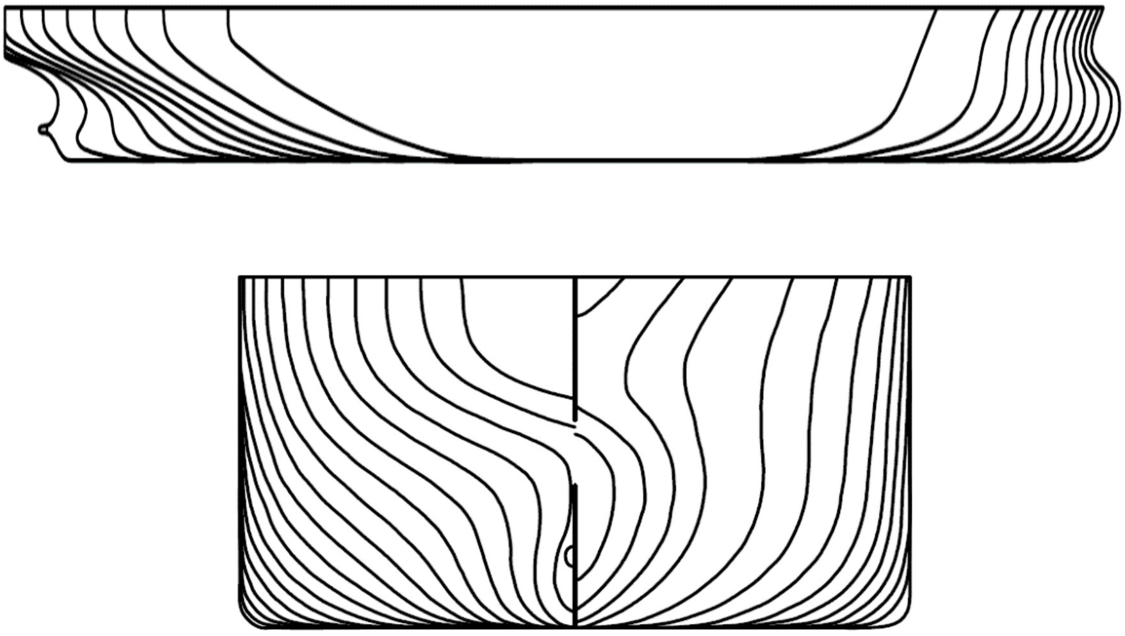

Figure 2- 1 Lines plan of KVLCC2

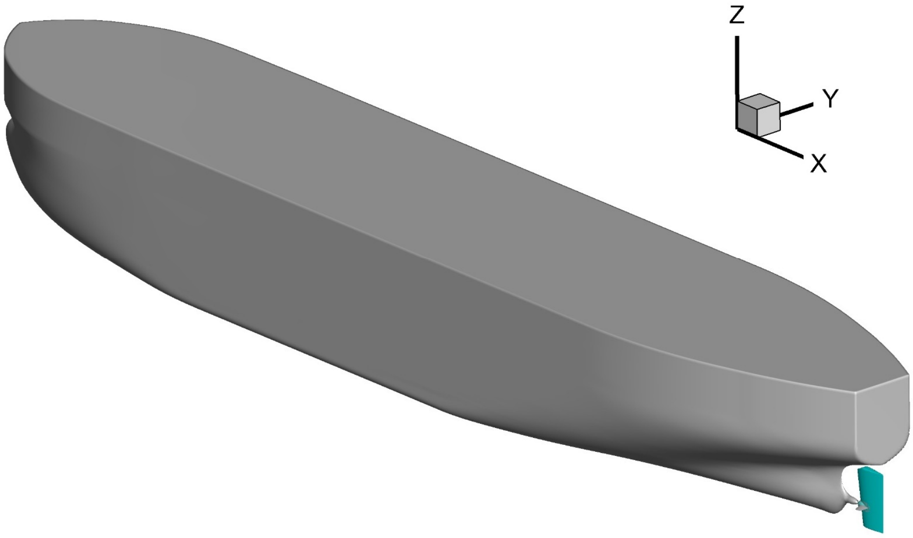

Figure 2- 2 3-D hull model of KVLCC2

Table 2- 1 Principal particulars of KVLCC2, propeller and rudder

Main particulars	**Symbol**	**Full scale**	**Ship model**	**Unit**
Length between perpendiculars	L_{PP}	320	3.2	m
Breadth at water line	B_{WL}	58	0.58	m
Depth	D	30	0.3	m
Draft (fully loaded condition)	T	20.8	0.208	m
Displacement	∇	312622	0.313	m^3
Block coefficient	C_B	0.8098	0.8098	…
Mid-ship section coefficient	C_M	0.9980	0.9980	…
Propeller				
Diameter	D	9.86	0.0986	m
Expanded blade area ratio	A_e/A_0	0.431	0.431	…

No. of blades	N	4	4	No.
Pitch ratio (0.7R)	p/D	0.721	0.721	…
Hub ratio		0.155	0.155	…
Rotation direction		Right hand	Right hand	…
Rudder				
Type		Horn	Horn	...
Area		273.3	0.02733	m^2
Lat. Area		136.7	0.01367	m^2

2.1.2 Grid Generation

The structured grid was generated using Pointwise software (Pointwise, 2010) and used along with multi-block overset techniques to simplify the grid generation complexity. The whole computational domain consists of 11 overset grid blocks for conventional rudder and added more 4 blocks for rudder-fin, all the blocks related to the ship body are generated by a hyperbolic grid generator. A propeller disk is needed for propeller modelling. The fins have two overset parts; that is, one side of fin is connected to the rudder-bulb surface and the other side linked to tip. The wake refinement was built surrounding the ship stern to increase grid resolution and background grid that defines the overall domain of the computation and far-field boundary conditions. Since the wall function is not used in this research, the non-dimensional grid size normal to the solid surface is taken as 10^{-6} ($y^+<1$) to capture the boundary layer and turbulence. The grid is finer near water surface and ship body to obtain smoother surface deformation. Among the blocks, the numerical connectivity is generated by SUGGAR. To integrate the area, forces and moments properly, USURP (Unique Surfaces using Ranked Polygons) code is performed to supply weights on the cells overlapping on the solid surface. The total grid points are around 9 million and the detail of grids for each block is shown in the following table.

Table 2- 2 Details of grids

Block name	**Type**	**I_{max}**	**J_{max}**	**K_{max}**	**Total**
Hull (port)	O-grid	154	50	144	1108800
Hull (starboard)	O-grid	154	50	144	1108800
Stern (port)	O-grid	55	50	40	110000
Stern (starboard)	O-grid	55	50	40	110000
Hub (port)	O-grid	55	50	40	110000
Hub (starboard)	O-grid	55	50	40	110000
Propeller	O-grid	35	111	105	407925
Rudder (port)	O-grid	44	45	97	192060
Rudder (starboard)	O-grid	44	45	97	192060
Fin (port)	O-grid	101	42	47	199374
Tip (port)	O-grid	101	37	21	78477
Fin (starboard)	O-grid	101	42	47	199374
Tip (starboard)	O-grid	101	37	21	78477
Wake refinement	H-grid	151	81	81	990711
Background	H-grid	216	121	151	3946536
Total					8 942 594

2.1.3 Computational Domain and Boundary Conditions

By considering the increase of computational time, the half computational domain was used in some applications. In these computations, however, the flow is asymmetric due to the different geometries between both rudder sides, the whole computational domain is required to envelope the flow field around ship body and downstream. The non-dimensional computational domain which showed in Figure 2-3 with boundary conditions is a rectangular prism and extends range in 3-direction; $-0.5<x/L_{PP}<2.35$, $-1<y/L_{PP}<1$ and $-1<z/L_{PP}<0.22$, where x, y, z are the components of the Cartesian coordinate. The ship bow (FP) is located at $x/L_{PP}=0$ and the stern (AP) is located at $x/L_{PP}=1$. X-coordinate is taken as positive towards the aft of the ship. Y-coordinate is taken positive towards starboard direction and Z is positive in upward direction which can be seen clearly either in Figure 2-3 or Figure 2-4. The undisturbed free surface is located at $z/L_{PP}=0$.

For inlet boundary condition, the free inflow velocity is set as non-dimensional ship speed ($u/U_0=1$). The exit boundary condition is used for the outlet. The far-field boundary conditions are implemented on the domain of top and bottom. Zero gradient boundary condition is applied for all the solid surfaces. The detail is described in Table 2-3 and noted that the rotating hub is considered as shown in Figure 2-5. The hub rotation is in the same direction as the propeller rotates. Each grid on the hub surface is set at the same number of revolution with the propeller and its effect is introduced into the RANS code. With $u/U_0=0$ imposed on the hub surface, the tangential velocity components (v/U_0 and w/U_0) are specified according to the propeller angular velocity: $2\pi r_{hub}n$ where r_{hub} is hub radius and n represents the propeller revolution rate.

Table 2- 3 Boundary conditions

	u	V	w	p	k	ω
Inlet	U_0	0	0	$\nabla p=0$	10^{-7}	9.0
Outlet	$\nabla^2 u=0$	$\nabla^2 v=0$	$\nabla^2 w=0$	$\nabla p=0$	$\nabla k=0$	$\nabla \omega=0$
Bottom	U_0	$\nabla v=0$	$\nabla w=0$	0	$\nabla k=0$	$\nabla \omega=0$
Top	U_0	0	0	$\nabla p=0$	$\nabla k=0$	$\nabla \omega=0$
Sides	$\nabla u=0$	$\nabla v=0$	$\nabla w=0$	$\nabla p=0$	$\nabla k=0$	$\nabla \omega=0$
No-slip	0	0	0	$\nabla p=0$	0	$\frac{60}{\mathrm{Re}\,\beta \Delta y^2}$

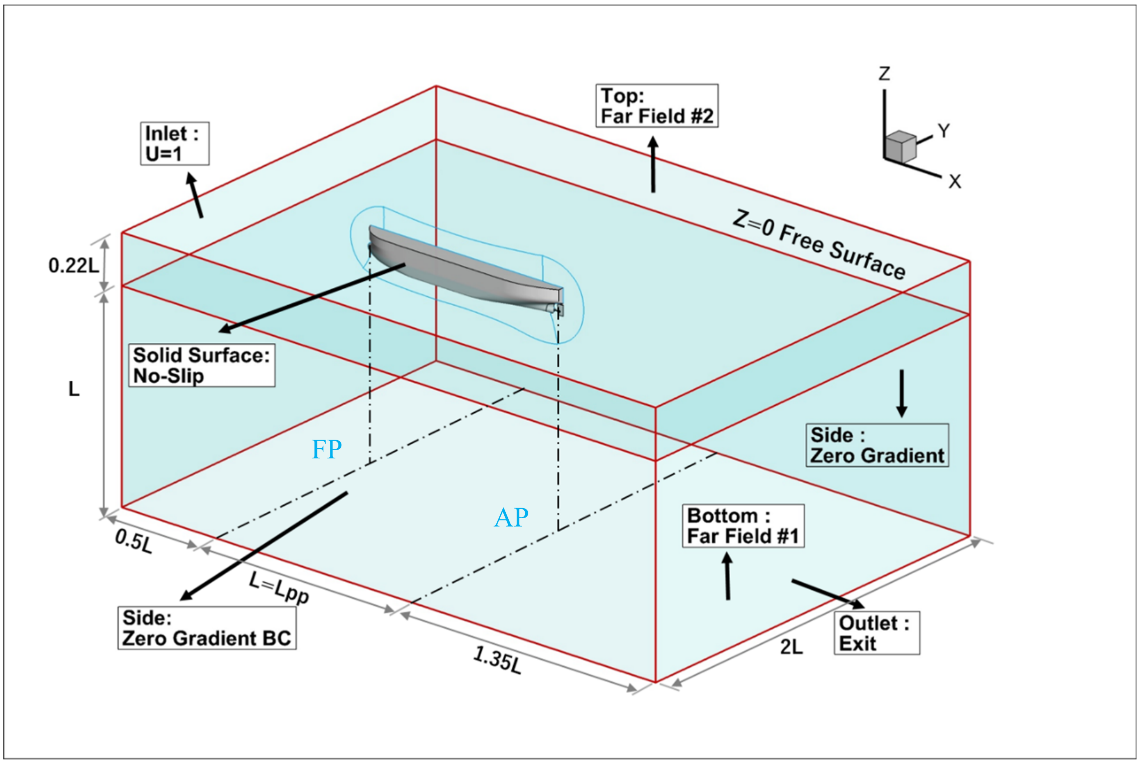

Figure 2- 3 Computational domain and boundary conditions

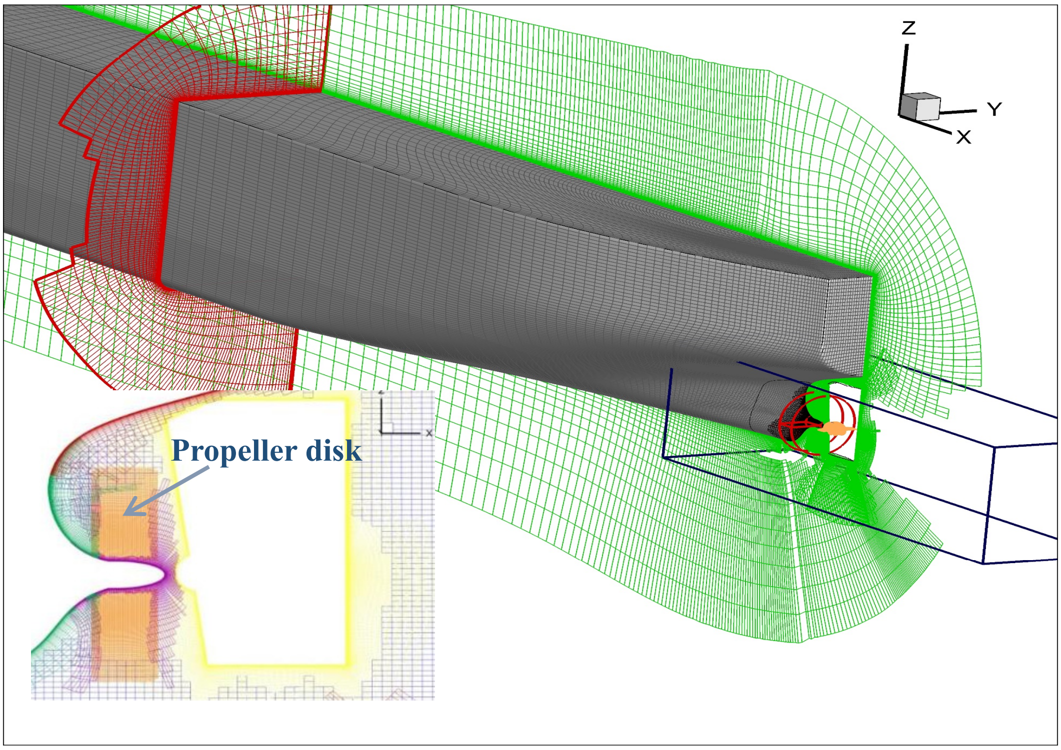

Figure 2- 4 Overset grid system

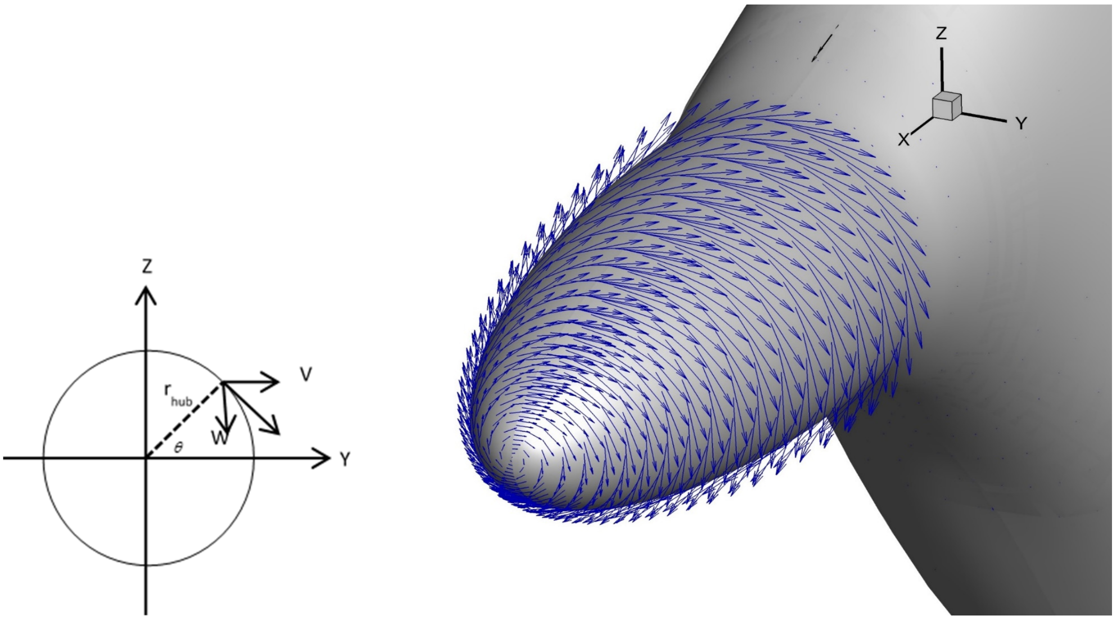

Figure 2- 5 Hub rotation

2.1.4 Overview of CFDShip-Iowa Version 4.5

CFDShip-Iowa is a general-purpose CFD simulation software that has been developed at the Iowa University for supporting research projects as well as transition to Navy laboratories, industries and universities. CFDShip-Iowa code has been leading ship hydrodynamics CFD code for over 20 years, which has been verified and validated for many applications in flow around ship. CFDShip-Iowa uses body-fitted structured multi-block grids in a finite difference approach to accommodate complex geometries and dynamic motions. The Reynolds-averaged Navier-Stokes computer program allows researchers to predict the flow phenomenon around a virtual ship model, prototype and its motions under different conditions. CFDShip-Iowa is one of the most advanced computational fluid dynamics computer codes in the word for ship hydrodynamics.

CFDShip-Iowa version 4.5 is an incompressible URANS/DES solver designed for ship hydrodynamics. The equations are solved in either absolute or relative inertial non-orthogonal curvilinear coordinate system for arbitrary moving but non-deforming control volumes. Turbulence models include blended k-ε/k-ω based isotropic and Algebraic Stress Model (ASM) based anisotropic RANS and DES approaches. A single-phase level-set method is used for free-surface capturing. It also provided captive, semi-captive, full 6-degree of freedom capabilities for multi objects with child/parent hierarchy. Not only the fully discretized propeller but also body-force propeller model can be employed for propulsion. Incompressibility is enforced by a strong pressure/velocity coupling, achieved using either Pressure-Implicit Splitting Operator (PISO) or projection algorithms. However, the velocity/pressure coupling is solved by the projection method for all the simulations of this project. The equations related to fluid phenomenon are solved in an inertial earth-fixed system while the equations related to rigid body are solved in the ship coordinate. All equations of motion are solved in a sequential form and iterated to achieve convergence within each time step.

2.1.5 Mathematical Model

2.1.5.1 Governing Equations

In fact, the governing equations can be illustrated by many ways depending on the coordinate systems are applied. For Cartesian coordinates, the continuous continuity and momentum equations in non-dimensional tensor form are defined as follows. All equations are non-dimensionalized by reference velocity U_0, length *L*, and density ρ

$$\frac{\partial U_i}{\partial x_i} = 0 \tag{1}$$

$$\frac{\partial U_i}{\partial t} + U_j \frac{\partial U_i}{\partial x_j} = -\frac{\partial p}{\partial x_j} + \frac{1}{\mathrm{Re}} \frac{\partial^2 U_i}{\partial x_j \partial x_j} - \frac{\partial}{\partial x_j} \overline{u_i u_j} + f_{b_i}^{*} \tag{2}$$

Where

$U_i = (\mathrm{U}, \mathrm{V}, \mathrm{W})$	The Reynolds-averaged velocity components
$x_i = (x, y, z)$	The independent coordinate directions
$p = \frac{p - p_\infty}{\rho U_0^2} + \frac{z}{Fn^2}$	The piezometric pressure coefficient
$\overline{u_i u_j}$	The Reynolds stresses which are a two-point correlation of the turbulent fluctuation u_i

$f^*_{b_i} \quad (=\frac{f_{b_i}L}{\rho U_0^2})$	The non-dimensional body-force vector. f_{b_i} is a force per unit volume which represents the effect of the propeller
$Fn=\frac{U_0}{\sqrt{gL}}$	The Froude number
$\mathrm{Re}=\frac{U_0 L}{\nu}$	The Reynolds number

2.1.5.2 Blade Element Theory

The body-force propeller model which provides the propulsive force and required torque for the ship was used throughout this research. The body-force propeller is predicted that not only simplifies the complex geometries but reduces the computational time as well. Figure 2-6 illustrated the way how the propeller actually generates thrust by absorbing a certain amount of power or torque. The simulations were performed with and without propeller effect to predict total resistance and self-propulsion factors. For with-propeller cases, the body-force propeller model based on the quasi-steady assumption and blade element theory (BET) using the total velocities (u/U_0, v/U_0, w/U_0). The velocities, which are provided by URANS solver, were used as the inflow to calculate the lift and drag on each blade element. In numerical simulations, propeller's parameters such as pitch angle and chord length distribution (as shown in Fig. 2-9) which are non-dimensionalized by propeller diameter are applied. The lift coefficient is obtained by Eq. 5, where k_1 is an empirical correction for finite blade width and α is the AOA against the zero-lift line. Drag coefficient is constant value as C_D=0.02. The local thrust (*dT*) and torque (*dQ*) on each blade element inside the propeller disk (cylindrical block) can be calculated from C_L and C_D. The longitudinal and tangential body-forces (fb_x, fb_θ) would be based on the average effect of *dT* and *dQ* among *N* blades, propeller rotation perimeter (*2πr*) at certain radius (*r)*.

$$U_r = \sqrt{u^2 + (2\pi nr - U_t)^2} \tag{3}$$

$$\beta = \tan^{-1}\left(\frac{U_t}{2\pi nr - w_t}\right) \tag{4}$$

$$C_L = 2\pi k_1 \sin(\alpha + \alpha_0) \tag{5}$$

$$C_D = 0.02 \tag{6}$$

$$k_1 = 1.07 - 1.05\left(\frac{c(r_e)}{R'}\right) + 0.375\left(\frac{c(r_e)}{R'}\right)^2 \tag{7}$$

$$dL = \frac{1}{2} C_L U_r^2 c(r) \tag{8}$$

$$dD = \frac{1}{2} C_D U_r^2 c(r) \tag{9}$$

$$dT = dL \cos\beta_i - dD \sin\beta_i \tag{10}$$

$$dQ = (dL \sin\beta_i + dD \cos\beta_i).r \tag{11}$$

$$fbx = \frac{dT.N}{\Delta x.2\pi r} \tag{12}$$

$$fb_\theta = \frac{dQ.N}{\Delta x.2\pi r^2} \tag{13}$$

The quasi-steady assumption effect is useful in ship applications such as seakeeping and ship maneuvers. The momentum equations in URANS solver would be solved along with those body-forces as the source terms. The components of total propeller forces and moments would be considered in the equations of motions in the 6 degrees of freedom

(6DOF) solver. Several coordinate transformations are required in the code since the flow field, 6DOF motion and the propeller are solved in different coordinates, namely earth coordinate, ship coordinate and shaft of propeller coordinate, respectively.

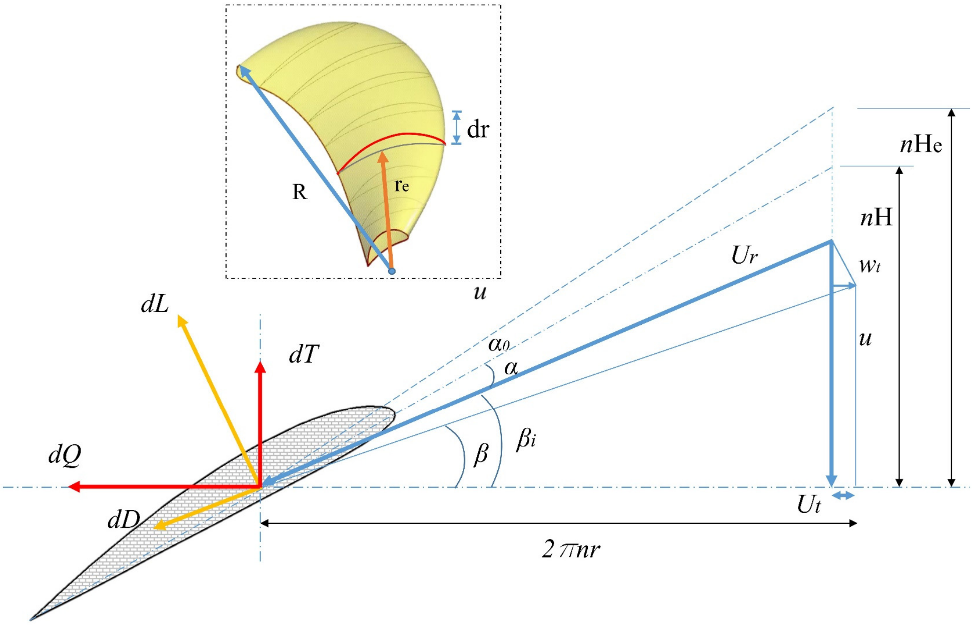

Figure 2- 6 Blade element theory

The concept of using total velocities is useful in many kinds of ship applications as well. The main advantages are: (1) induced velocity subtraction is not required, (2) free vortex is not assumed and fixed. In traditional propeller code, the governing equation is Laplace’s equation: $\nabla^2\phi = \nabla\vec{u} = 0$ with boundary condition $\hat{n}.\vec{u}=0$ based on potential flow theory. When coupling the propeller code and URANS, a procedure or technique of induced velocity subtracting is required as mentioned by Simonsen and Stern (2005). The inflow velocity becomes known after subtracting induced. The unknown induced velocity $\vec{u}_{induced}$ can be solved by known normal vector $\hat{n}$ on body geometry and inflow velocity

$\vec{u}_{inflow}$ via a linear system $[\hat{n}][\vec{u}_{induced}]=[-\hat{n}.\vec{u}_{inflow}]$. In the next step, many methods to solve induced velocity; for instance, small perturbation method like lifting line and lifting surface/vortex lattice method, or panel method/boundary element method based on Green's third identity. In most of those methods, the induced velocity on body geometry is induced by bound vortex and free vortex which is a linear superposition, i.e. $\vec{u}_{induced}= \vec{u}_{bound\text{-}vortex} + \vec{u}_{free\text{-}vortex}$. The strength of bound vortex is unknown on body geometry. It means that the helical pitch and shedding direction of free vortex have to be assumed and fixed in a certain shape. The induced velocity subtraction is not needed anymore since the total velocity is used. The free vortex is included in the total velocity solved by RANS and the bound vortex strength would be solved in the propeller code. It is possible to implement this concept in any inviscid propeller code such as: $[\hat{n}][\vec{u}_{bound\text{-}vortex}] = [-\hat{n}.\vec{u}_{RANS}]$, where $\vec{u}_{RANS}= \vec{u}_{free\text{-}vortex} + \vec{u}_{inflow}$. It is beneficial for applying the propeller model to the present work because the free vortex would be disturbed by the rudder and energy-saving devices.

2.2 Experimental Fluid Dynamics

The experiments were conducted in a towing tank of Osaka University having dimensions of 100m length, 7.8m width and 4.35m depth. The towing carriage runs between both ends of the tank that can run with maximum speed of 3.5m/sec. During the experiments, the environmental conditions are also considered such as the average water temperature is around 15.8^0 C and average air temperature is about 13.6^0 C. The ship model is KRISO Very Large Crude Carrier 2 which is called KVLCC2 with a model scale of 1:100. The ship model for experiment was tested at a design speed of 0.795 m/sec which having the Froude number of 0.142 corresponding to 3.2 m ship model length. The model was free to heave and pitch during the tests. The heave and pitch values are measured using the potentiometers which are installed at both fore and aft perpendiculars of the ship. The moving carriage towed the ship model at a constant speed, in this process, the model resistance is measured by resistance dynamometer which was attached at the center of ship gravity.

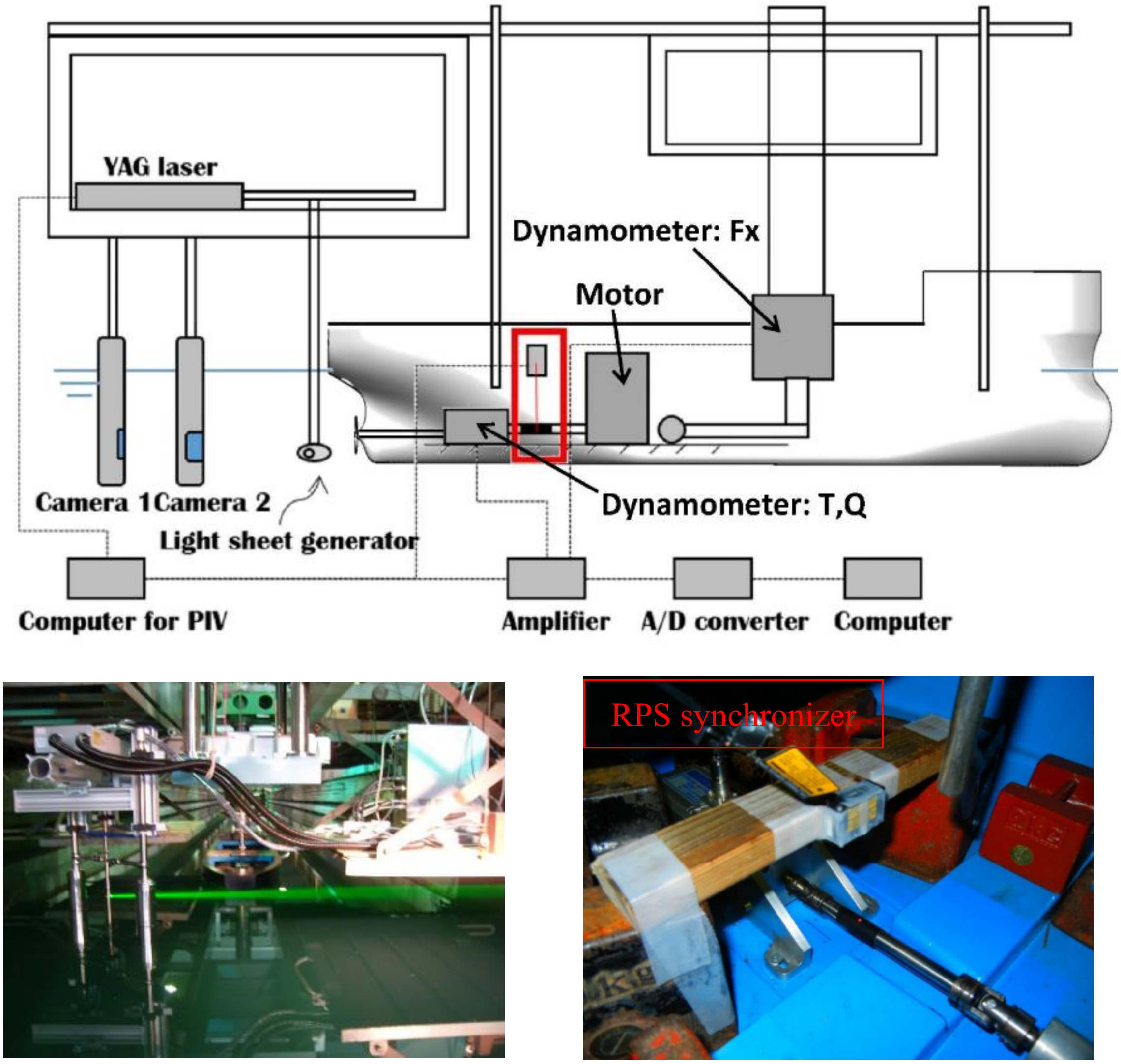

Figure 2- 7 Schematic layout and equipment of model towing test

The underwater S-PIV system is used to measure the velocity field of ship wake. The laser sensors were mounted at the bow and stern to detect their vertical displacements to obtain sinkage and trim. The propeller revolution rates were determined by self-propulsion test; 16.5 RPS for conventional rudder case and 16.3 RPS for rudder-fin case, and the flow field was measured at the corresponding RPS. A RPS synchronizer was designed to trigger the S-PIV laser and two underwater cameras followed the phase of the propeller rotation. The trip wire at 10% chord position of propeller is attached for small size propeller mode. The measured flow field would be further phase-averaged. A dynamometer was attached at the center of gravity of the ship to measure the total resistance. The thrust and torque of propeller through the shaft were recorded by another set of dynamometer.

The propeller model in experiment is MOERI tanker KVLCC2 with four bladed. For propeller model, two propeller models with opposite rotational direction were made for flow field measurement on both sides of ship. In the case of having rudder or rudder-fin, the S-PIV laser would be blocked by the rudder body. A mirror image process was developed to combine both sides of measured image with respect to the center line.

Figure 2- 8 KVLCC2 propellers model

[left for anticlockwise, right for clockwise]

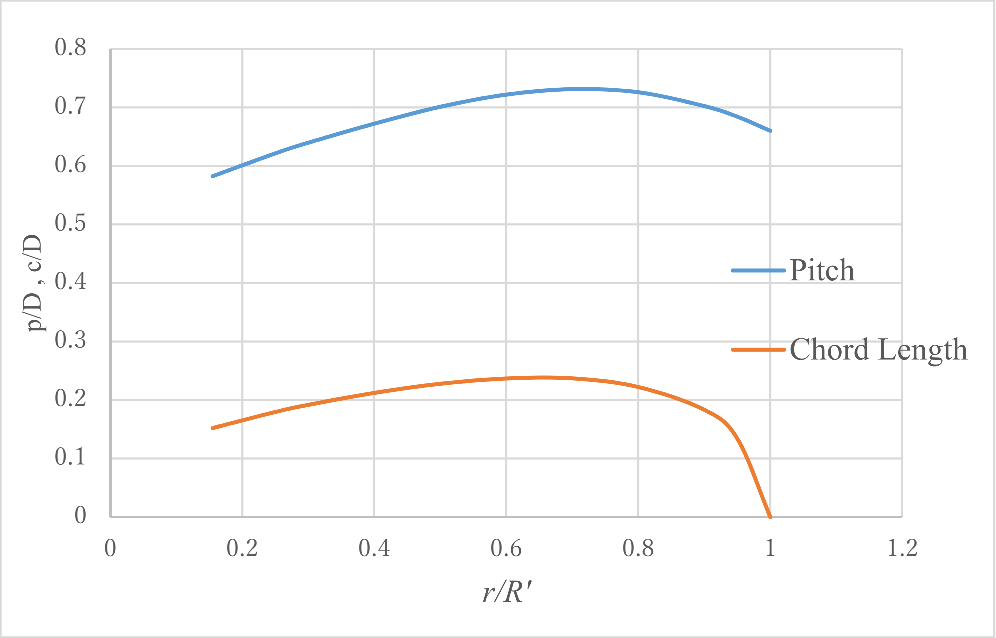

Figure 2- 9 Chord length and pitch distribution of KVLCC2 propeller

In numerical calculations, the propeller model is represented by the pitch and chord length distributions which are non-dimensionalized by the propeller diameter, can be seen in Fig. 2-9.

CHAPTER 3: RUDDER-BULB-FIN SYSTEM

3.1 Methodological Approach

The idea of Rudder-Bulb-Fin system and its improvement are approached through the traditional way; that is, by analyzing the flow field around the downward in the event of conventional rudder. The velocity at several sections near propeller disk (Figure 3-1) in contour and graph with its non-dimensional value is displayed in Fig. 3-2.

The flow behind propeller trends to move up on port side and move down opposite on other side. The range of sizable different velocity along y-direction can be seen in the graph from around -0.5 to 0.5 at the position in which close to rudder center ($y/L_{PP}=0$). It is predicted that a little loss energy can be converted into thrust by adding a pair of horizontal fins. The fundamental principle of this prediction is shown in the diagram (Fig. 3-3).

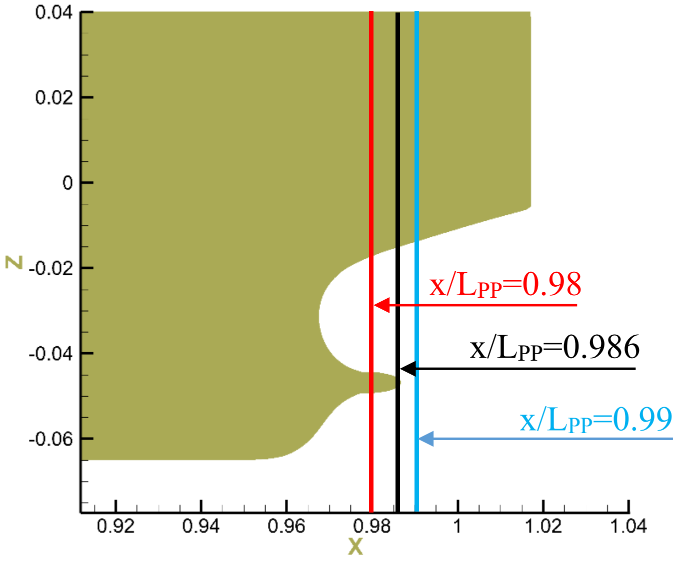

Figure 3- 1 Cross section of measurements

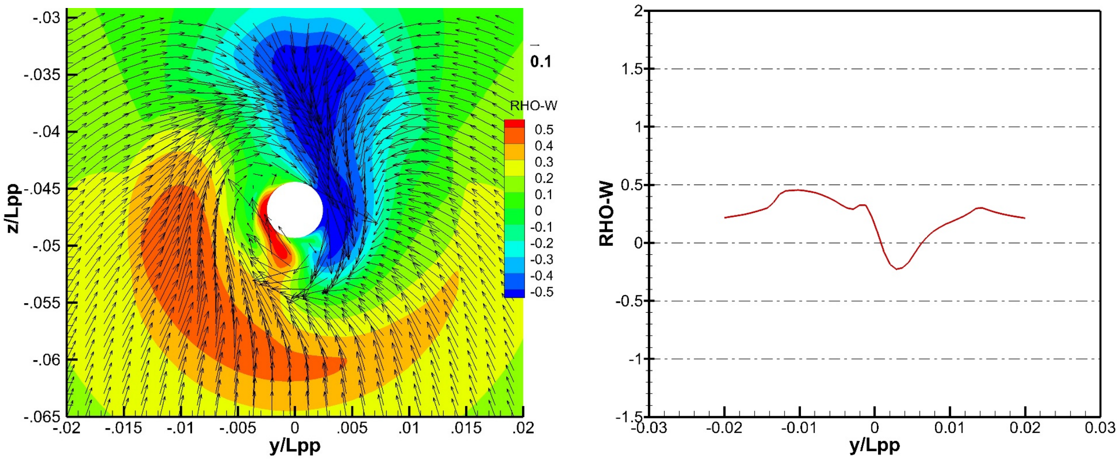

x/Lpp=0.98

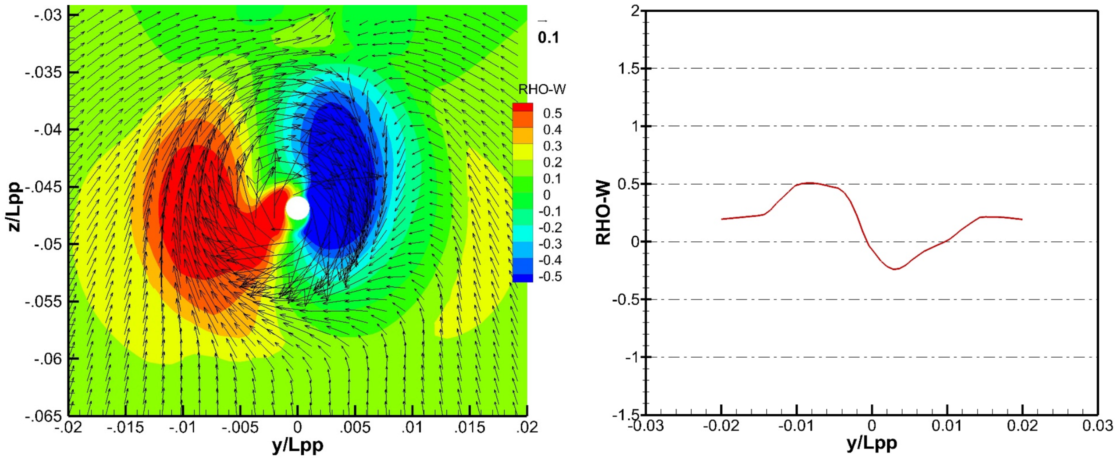

x/Lpp=0.986

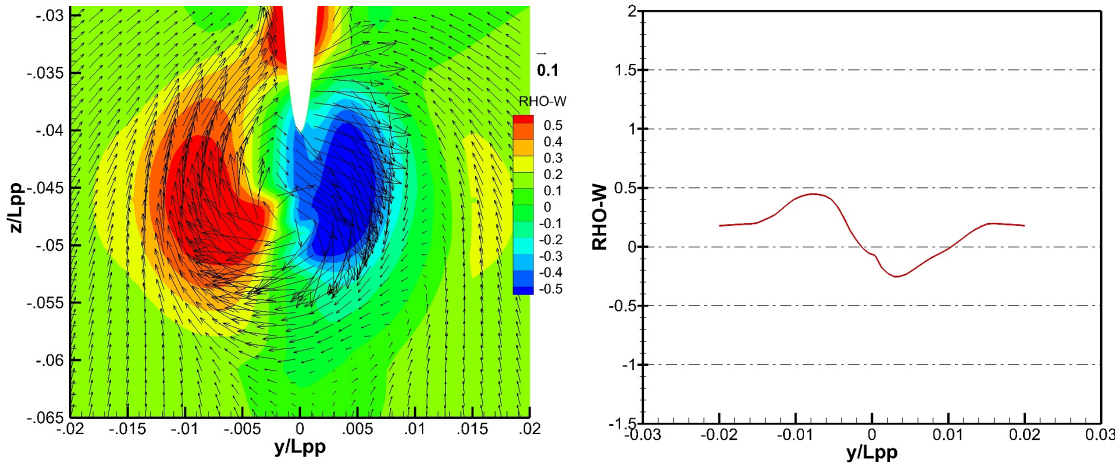

x/Lpp=0.99

Figure 3- 2 Velocity distribution

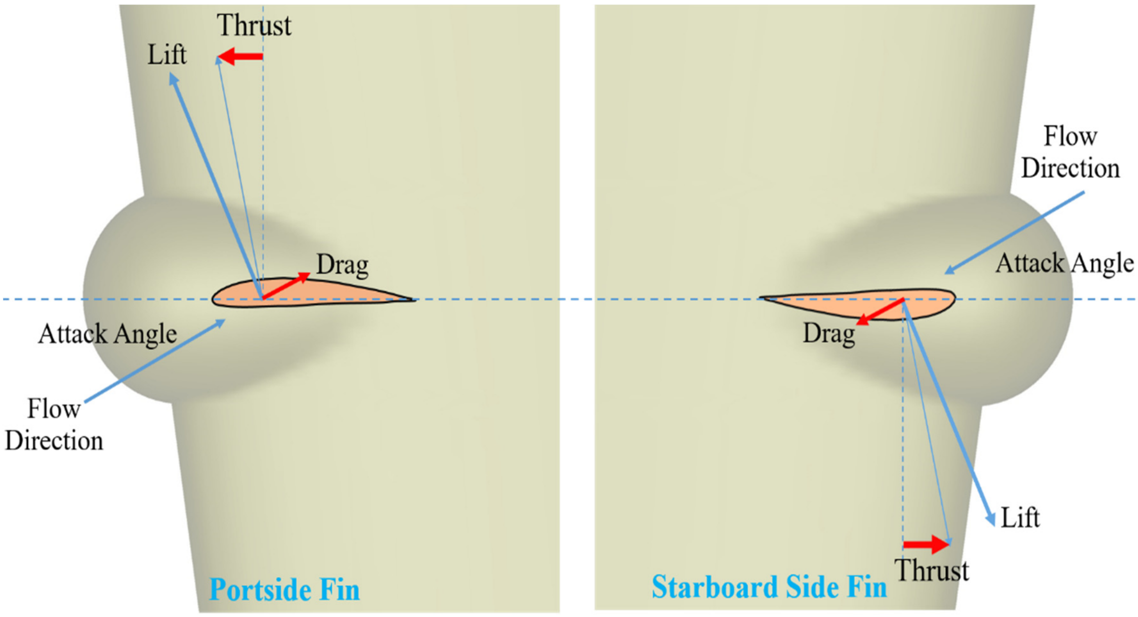

Figure 3- 3 Diagram for thrust generation

Fig. 3-3 describes how the additional thrust is created by adding a horizontal fin on the rudder-bulb. According to Bernoulli’s Principle, after separating at the stagnation points start from leading edge, the flow travels under and over the fin. The consequence of this is that the flow below the fin has a higher pressure than the flow above the fin for port side fin and vice versa for starboard side. And this different pressure creates the lift which is projected onto the horizontal component is thrust as shown in Fig. 3-3. With the same airfoil, the magnitudes of the lift and drag are dependent on the angle between the chord line and direction of water flow.

3.2 Rudder-Bulb-Fin geometry

The dimension of Rudder-Bulb-Fin system is described in detail through Figure 3-4. The fin is attached on the rudder-bulb surface for both sides. The fin length is designed proportionate to the propeller radius. The suction is facing up for port fin and down for starboard fin which is clearly observed in the red (orange) area either Fig. 3-3 or Fig. 3-4.

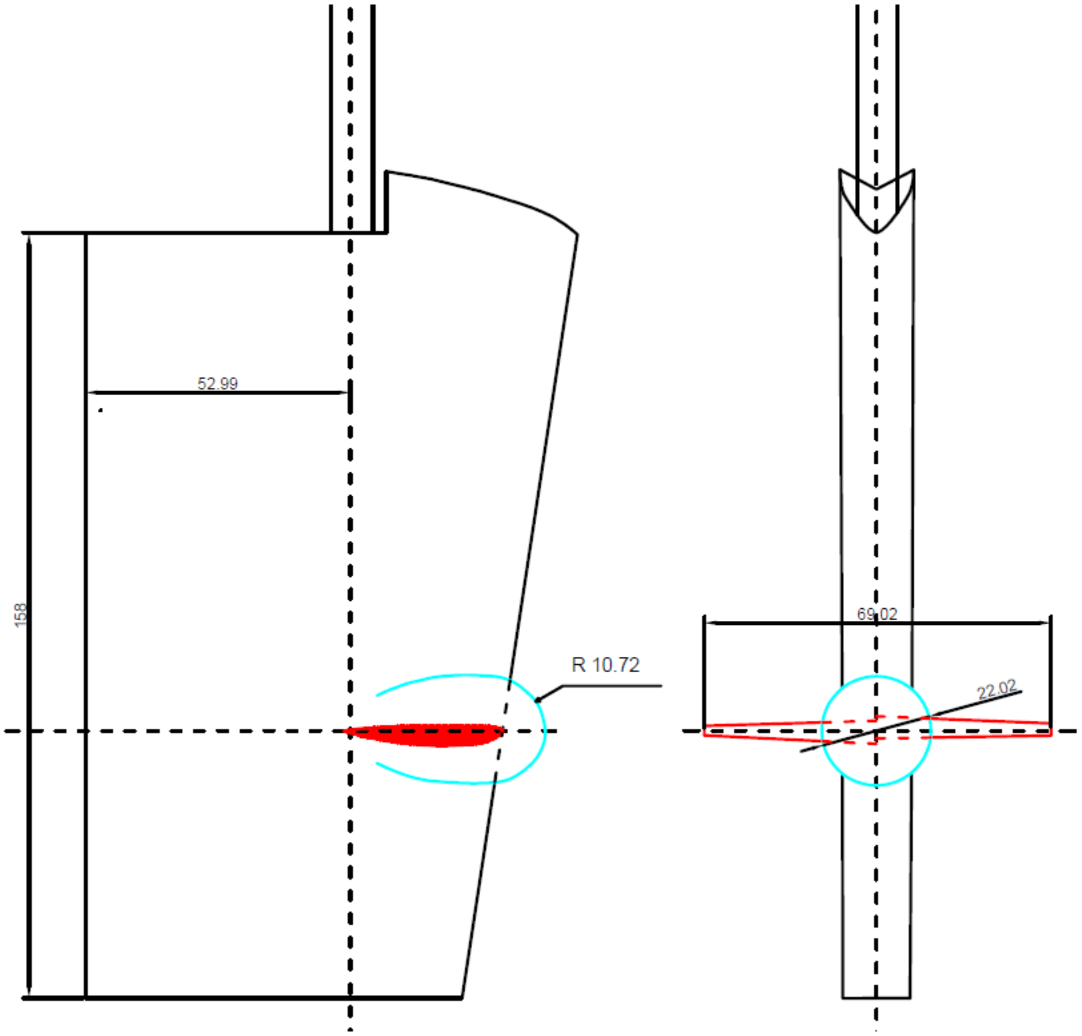

Figure 3- 4 Dimension of Rudder-Bulb-Fin

3.3 Different Attack Angle of Fin

3.3.1 Small Changing Angle of Attack

The ideas of this part concentrated on the different benefits among small changing attack angle which were adjusted from -2 to 1 degree with 1-degree increment for both sides of rudder-fin. Several cases based on different AOA of fins were simulated using CFDShip-Iowa code with a propeller model. The detail of change can be seen in figure below. The rotating axis was defined at mid-chord of center-plane's section.

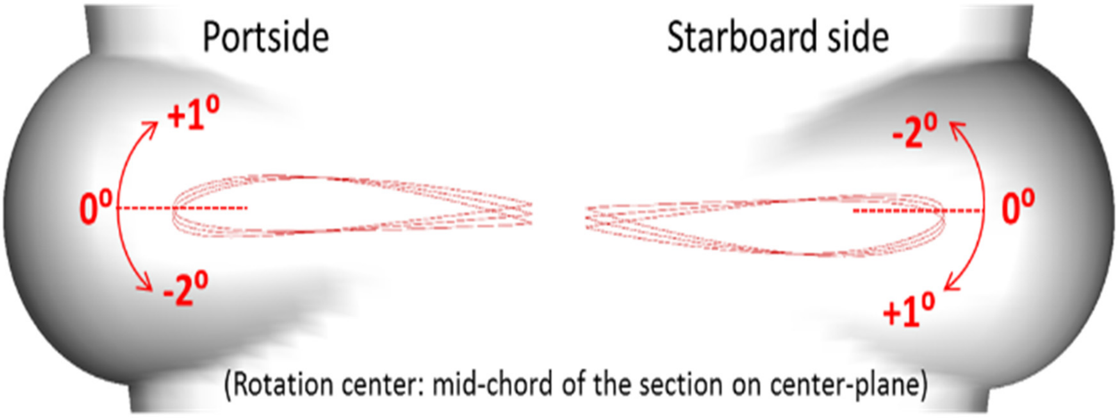

Figure 3- 5 Variation of attack angle for both fins

Totally 32 simulation cases in small changing attack angle group were carried out with- and without propeller. For each combination, the re-mesh process was required for the fin body block and overset grid connectivity was re-built by Suggar code.

3.3.2 High Changing Angle of Attack

The angle between the flow direction and the chord line is normally called the attack angle and it has a large effect on generating lift. The lift/drag ratio is also mentioned in "Theory of Wing Sections" by Ira H. Abbott (1949) that the lift/drag (or lift coefficient by drag coefficient) ratio based on the attack angle. For small attack angle, the flow over the airfoil is essentially smooth and the magnitude of the drag is nearly constant. The frictional drag is highly dependent on the flow conditions. The free form vortices and turbulence occurs in laminar flow, resulting in minimum frictional drag. The separation point moves up the leading edge of airfoil and the turbulent flow occurs when increasing the angle of attack. The maximum lift normally receives when the angle of attack is around 15~20 degrees based on specially designing for airfoil. The attack angle is always considered and adjusted to meet the most efficient angle of attack. The phenomenal of flow passing through the fins is same as a wing. Fig. 3-6 shows how the fluid flows through the fins and the effect of attack angle to lift/drag ratio.

Based on the propeller rotation (i.e., right hand side in this research), the flow behind propeller trends to going down on starboard surface and going up on port side surface. The value of flow angle is predicted a bit higher than the most efficient angle of attack. Thus, by considering a decrease of lift magnitude and an increase of drag magnitude, a decision with changing 6-degree attack angle was taken for that purpose, see Fig. 3-7 for more details.

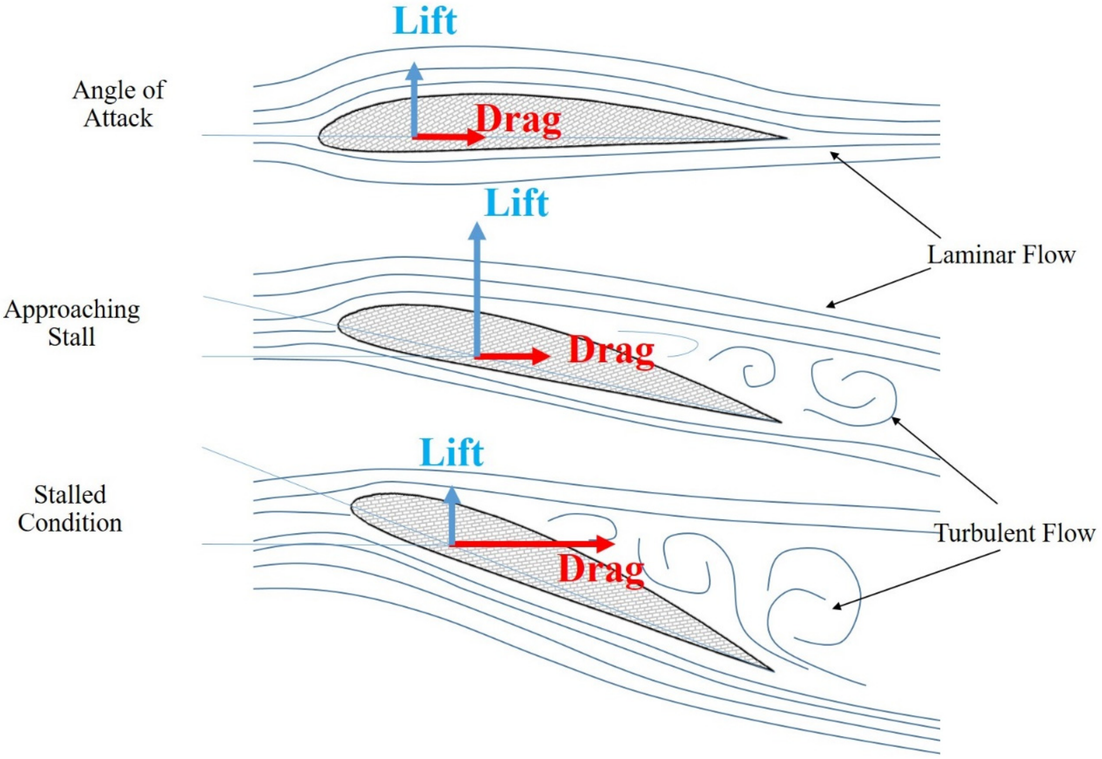

Figure 3- 6 Flow separation on fin section

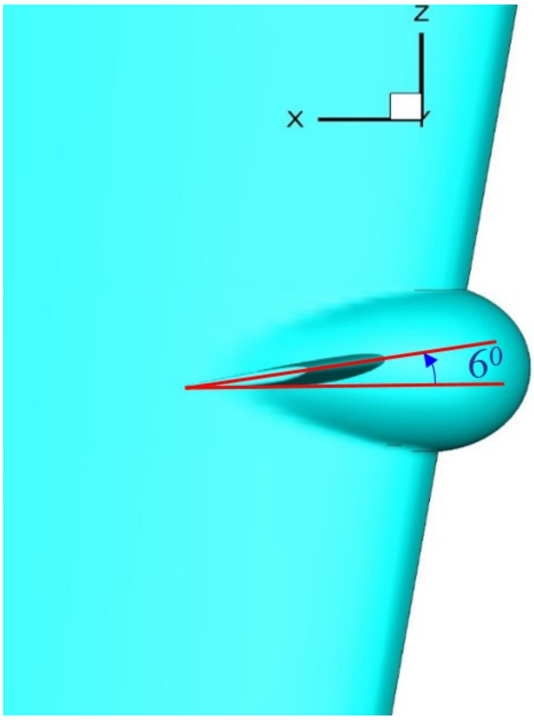

Figure 3- 7 Starboard side fin (rotated 6-degree up)

3.4 Twisted Fin

The idea of twisted fin comes from the different flow separation on several sections of span-wise fin. The twisted fin is expected that can be improved the upper and lower fin's surface flow field in which large flow separation occurs. The AOA of foil section for starboard fin is adjusted from three to zero degree corresponding from root to tip linearly whereas the port side fin maintains as original.

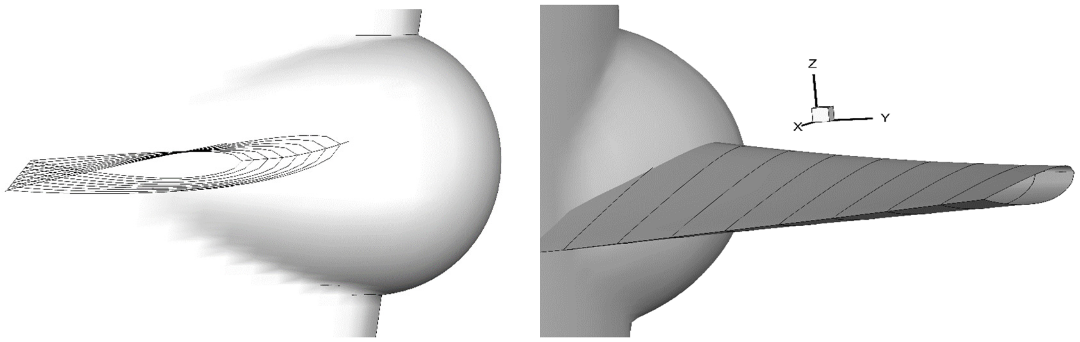

Figure 3- 8 Demonstration of twisted fin [starboard side]

3.5 Cutting Starboard Side Fin

In general, the flow behind propeller is going down on starboard and going up on port side surface. Nonetheless, for starboard side fin, the flow in the vicinity of fin-tip trends to moving up. It means that the force which provided by fin-tip is not thrust (the same force magnitude but opposite direction). Another reason is that the wetted area is slightly decreased by making shorter the length of starboard fin which directly effects to total resistance.

The length of starboard side fin is shorter than the original, the results of 3 cases with different AOA and starboard fin length are shown. The difference is described through

Fig. 3-9. The starboard side lengths were cut as Fig. 3-9; that is, the fin lengths for those cases are y/L_{PP}=0.008 (green), y/L_{PP}=0.007 (red) and y/L_{PP}=0.005 (blue) with the starboard fin length gradually decreased. Those cases were named fin-cut0.008, fin-cut0.007 and fin-cut0.005 respectively, for easy identification. Notice that the starboard side fin (fin-cut0.007 and fin-cut0.005) has the attack angle that rotated up 6-degree while the port side fin still maintains as original one for all cases.

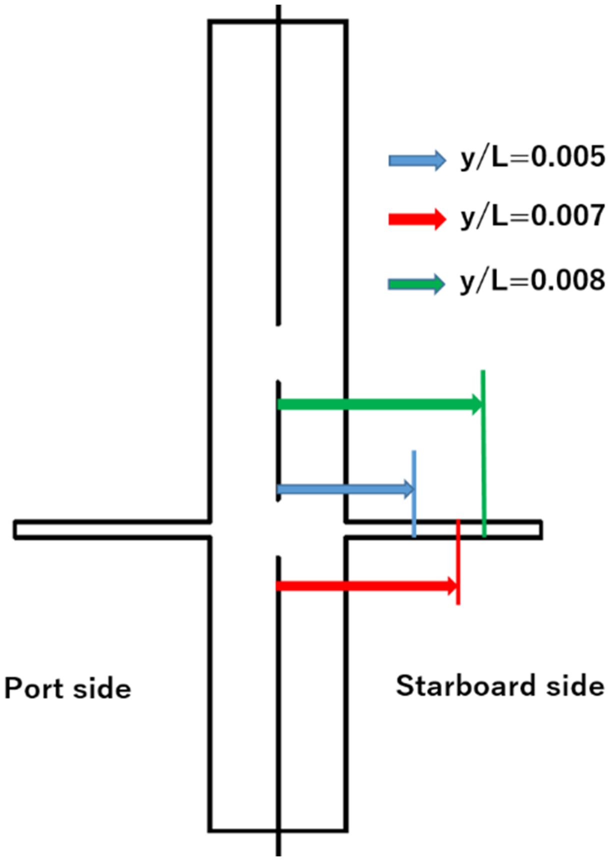

Figure 3- 9 Geometric diagram of cutting starboard side fin

3.6 Mean Camber Line and its Combination

3.6.1 Mean Camber Line

Several cambered wing sections are developed and introduced by the National Advisory Committee for Aeronautics (NACA) and each NACA foil provides different value to lift/drag ratio. The cambered 4-digit NACA foil had been chosen in the research of this time. The mean camber line is determined by the formula as follows (Ira H. Abbott et al. (1949)).

$$y_c = m\frac{x_c}{p^2}(2p - \frac{x_c}{c}) \qquad \text{for} \quad 0 \leq \; x < p \qquad (14)$$

$$y_c = \frac{m}{(1-p)^2}(1-2p+2px-x^2) \qquad \text{for} \quad p \leq \; x \leq 1 \qquad (15)$$

Where: m is maximum ordinate of the mean line in fraction of the chord (first digit)

p represents the location of maximum camber divided by 10 (second digit)

The fin-foil section has a maximum camber of 5 percent of chord located at the position of 40 percent of chord from the leading edge with a maximum thickness of 12 percent as a fraction of the chord (hereinafter, NACA5412). The position of upper points (x_u, y_u) and lower points (x_l, y_l) are defined by the following relationship and plotted in 2D Cartesian coordinate as shown in Figure 3-10.

$$x_u = x_c - y_t \sin\theta \qquad x_l = x_c + y_t \sin\theta$$

$$y_u = y_c + y_t \cos\theta \qquad y_l = y_c - y_t \cos\theta$$

Where y_t is thickness distribution and $\theta = \tan^{-1}(\frac{dy_c}{dx_c})$

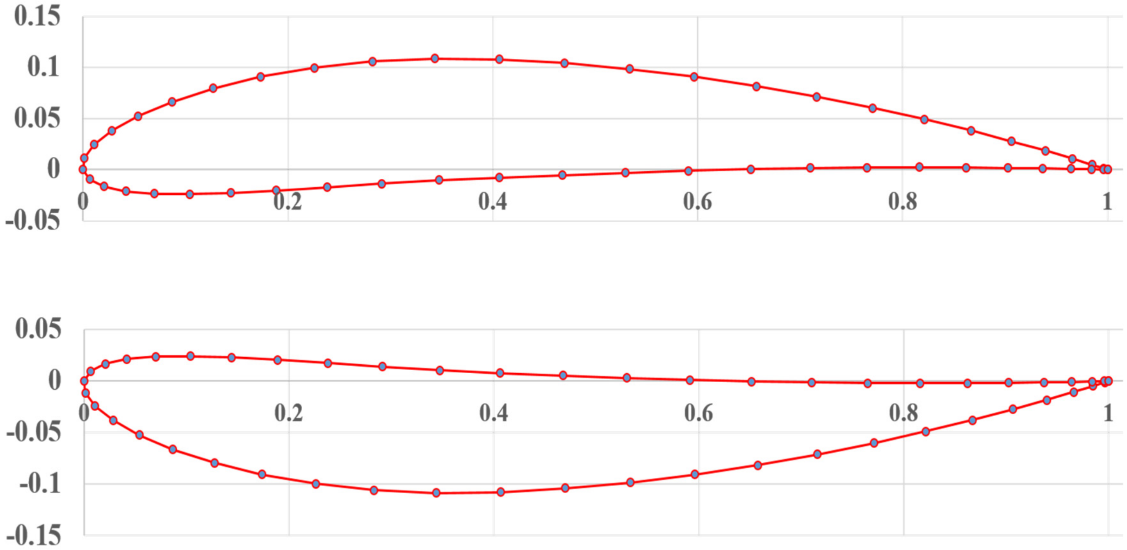

Figure 3- 10 Airfoil section of NACA5412 [upper curve for port side and lower curve for starboard]

3.6.2 Comparison with other Factors

It is common knowledge that the fin-lets might reduce the fin-tip vortices and increase the efficiency of fin. In this part, the cap of tip was rounded end in order to slightly improve the efficiency of the end of the fin. Note that the mean camber line at the end of tip still maintains as the shape of the original one. The results of five kinds of RBFS in changing mean camber line and adjusting AOA are shown:

- The NACA5412 (1) which attack angle maintains as original (hereinafter NACAps0_sb0)
- The NACA5412 (2) which starboard fin is rotated 1-degree up (hereinafter NACAps0_sb1)
- The NACA5412 (3) which starboard fin is rotated 6-degree up (hereinafter

NACAps0_sb6)

- The NACA5412 (4) which starboard fin is rotated 1-degree up and port side fin is rotated 1-degree down (hereinafter NACAps1_sb1)
- The NACA5412 (5) which starboard fin is rotated 6-degree up and port side fin rotated 6-degree down (hereinafter NACAps6_sb6)

In addition, the port side fin is moved down to the position of which the hub vortex is located in order to reduce strength of hub vortex or even totally eliminate the existed hub vortex. These cases are named NACAps0-sb0_0.004z0.003x, NACAps0-sb6_0.004z 0.003x, NACAps6-sb6_0.004z0.003x based on the changing of cambered foil, attack angle and position in x- and z-direction. Those designs using NACA5412 as shown above and the position of port side fin moved down $x/L_{PP}=0.003$ in x-direction and $z/L_{PP}=0.004$ in z-direction. More detailed information can be seen in Fig. 3-11.

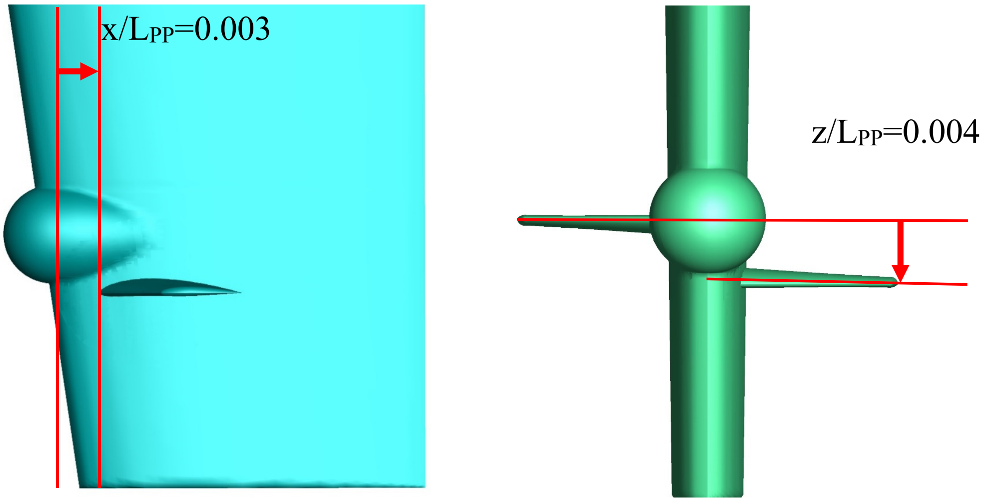

Figure 3- 11 View of new fin's position

CHAPTER 4: RESULT ANALYSES

The results of the following cases are shown in this dissertation:

(1) Comparison between conventional rudder and rudder-fin for both CFD and experimental data.

(2) Small changing attack angle. The research concentrated on the different benefits among small changing angles of attack which were adjusted from -2 to 1 degree with 1-degree increment for both sides of rudder-fin.

(3) High changing AOA. The angle between the flow direction and the chord line is called the AOA and it has a large effect on generating lift by horizontal fins. Following from the success of changing small attack angle and by considering a decrease of lift, a decision with changing 6-degree attack angle was taken for that purpose

(4) Twisted fin. The AOA of foil section for starboard side is adjusted from three to zero degree corresponding from root to tip linearly whereas the port side fin maintains as original one.

(5) Cutting starboard side. The starboard fin length is shorter than those of port side fin.

(6) NACA5412 and its combinations. The cambered 4-digit NACA foil, as a design of NACA, has been chosen in the research of this time.

(7) New position of fin. The port side fin is moved down 0.004 in z-direction and downward 0.003 in x-direction.

4.1 Conventional Rudder and Rudder-Fin

4.1.1 Validation between CFD and EFD results

4.1.1.1 Flow Field Analysis

Firstly, the simulation result would be validated against experimental data and then the simulation flow field can be analyzed in detail and further applied to the other applications. The axial velocity profile (*u/U_0*) and cross flow vector (*v/U_0, w/U_0*) of simulation and experiment are showed in Fig. 4-1 at stern section and Fig. 4-2 at downstream. In those figures, the flow fields are extracted on the section of AP position ($x/L_{PP}=1$) across the rudder surface and downstream ($x/L_{PP}=1.025$). The simulation and experiment data show good agreement on the flow pattern for both types of rudder. The axial velocities are accelerated by the propeller to 1.6 times ship speed. The upward flow in the outer area of the flow field is observed. The hub vortex would tend to move to the left side, i.e. port side, in the upward flow. Also, the propeller rotational flow would be interfered by the rudder body in the center line. Thus, the hub vortex attaches on the port side surface of the rudder and a downward flow is caused on the starboard side surface. Another vortex on the starboard side a bit away from the rudder, e.g. $y/L_{PP}\sim0.01$, is induced by the downward flow. For the rudder-fin, the vortices are truncated by the fins, especially the starboard side one. The hub vortex location is lowered due to the fin and bulb. Compared to the conventional rudder, the hub vortex area is smaller and axial velocity in its core decreases, which is more clear in experiment. The flow along the port side fin surface forms an upward jet and downward jet along the starboard surface which led by the propeller rotation. The high speed propeller flow was deformed in the same way.

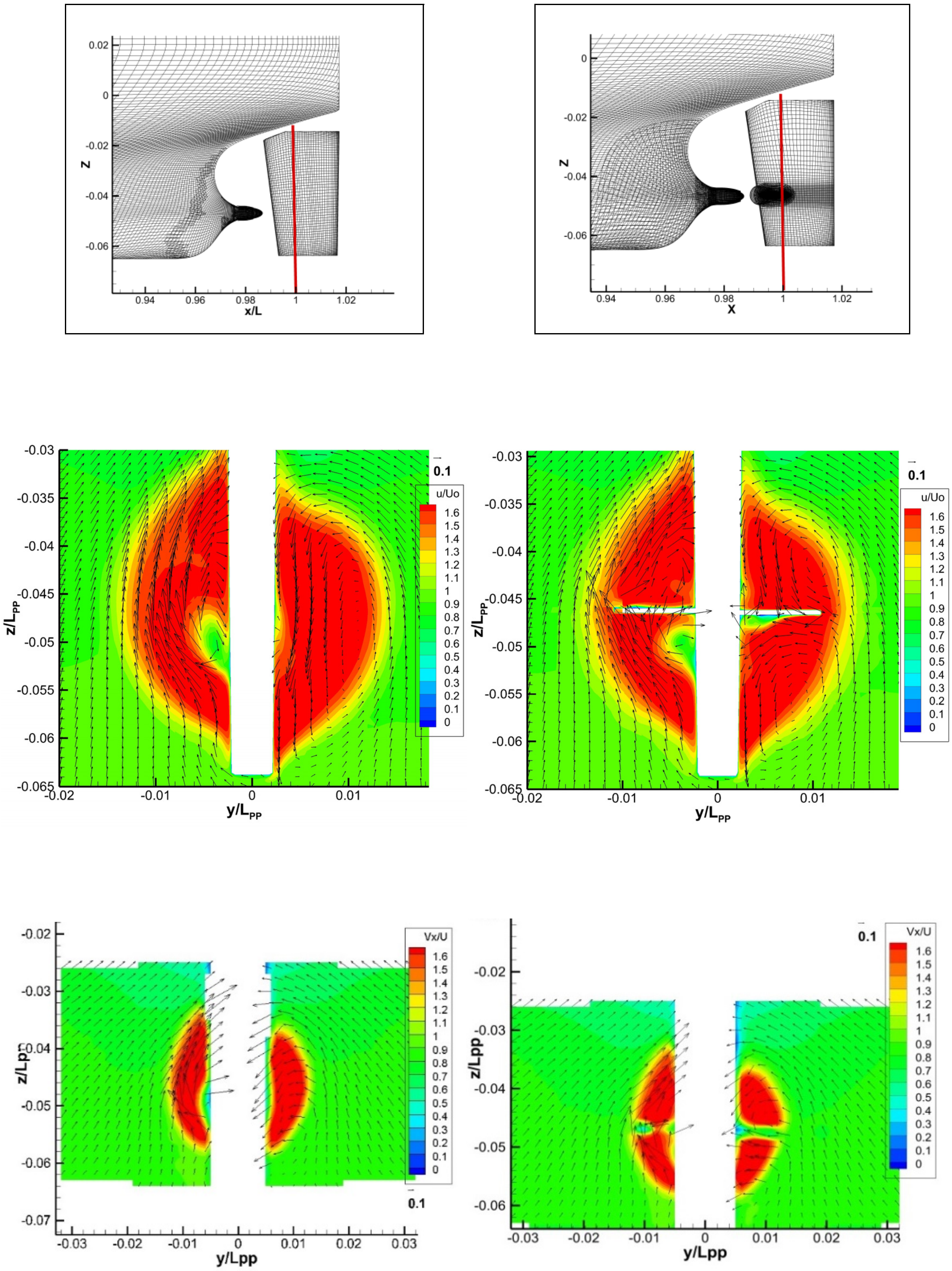

Figure 4- 1 Axial velocity profiles and cross flow vectors at x/LPP=1 for conventional rudder and rudder-fin [up for simulation and down for experiment]

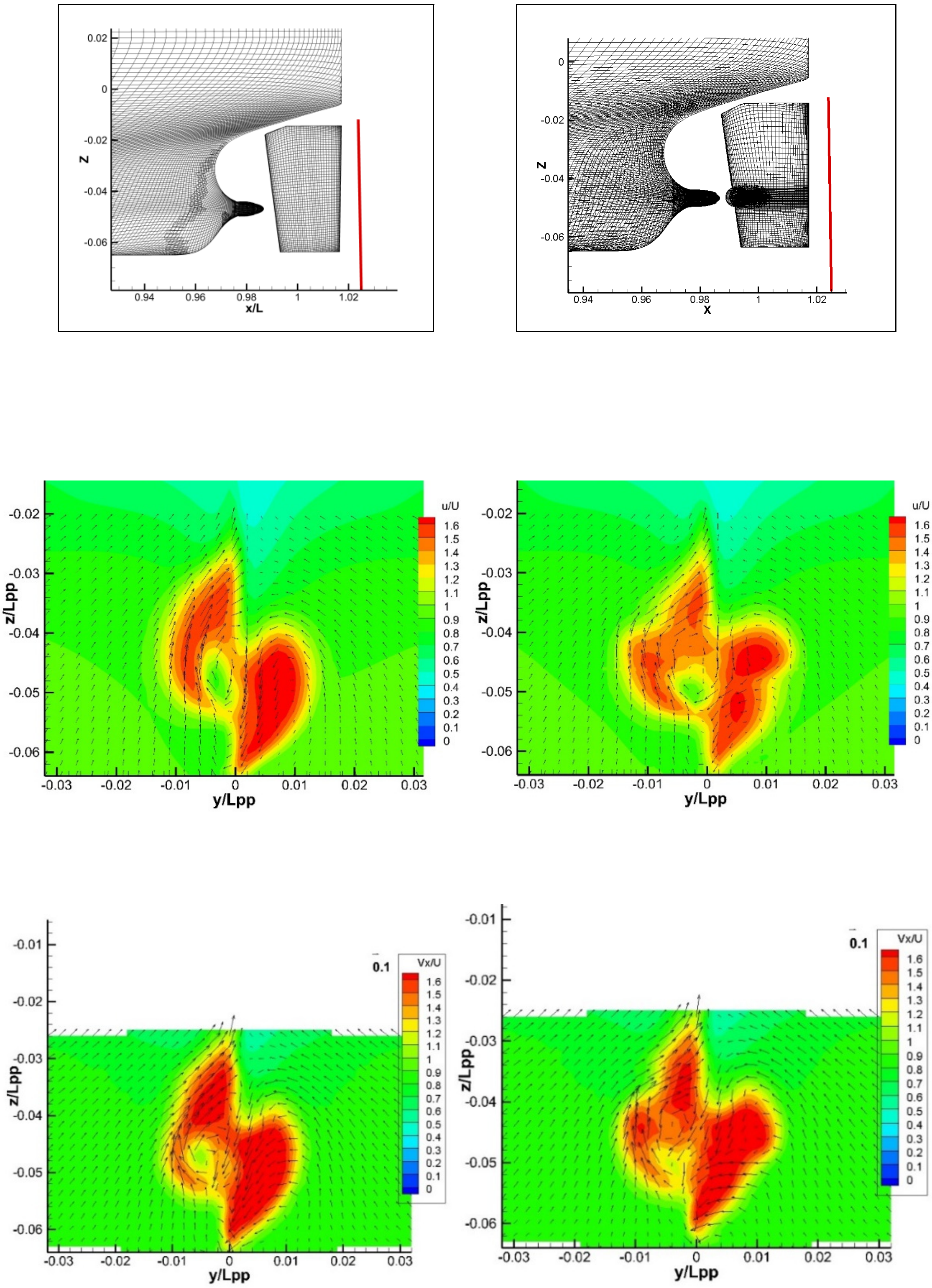

Figure 4- 2 Axial velocity profiles and cross flow vectors at x/L_{PP}=1.025 for conventional rudder and rudder-fin [up for simulation and down for experiment]

In Fig. 4-2, the flow fields are extracted on the section behind the trailing edge of rudder ($x/L_{PP}=1.025$). The figure layout is maintained the same as Fig. 4-1. The upward jet on port side and downward jet on starboard side are clearer here. The high speed propeller flow deforms much more in the downstream. The hub vortex strength decreases due to rudder bulb is clearer as well. Its area and velocity around the core are smaller in the event of bulb-fin's existence. The effect of fin to the flow pattern is obvious. Compared to the smooth round shape of the high speed area on the conventional rudder, the shape on rudder-fin case is twisted severely by the fin and concave is formed on both sides corresponding to the fin position. The flow field shows good agreement between simulation and experiment at the section $x/L_{PP}=1$ and $x/L_{PP}=1.025$ generally. The pattern and trend are basically the same. However, the simulation shows some numerical dissipation. Compared with experiment, the simulation has smaller contour area of $u/U_0=1.6$. The flow velocity drops faster in simulation.

4.1.1.2 Self-Propulsion Factors

The predicted self-propulsion factors would be validated against measured data in Table 4-1. Thrust deduction factor has small error between simulation and experiment, around 2% under-predicted. It indicates the hull-propeller interaction, i.e. the resistance difference between with and without propeller cases, was predicted well whether the fins were attached on the rudder or not. The larger (but acceptable) error appears for effective wake factor ($1-w$). The values are over-predicted 3%-7%, hence the hull efficiency values are in the similar error level (5%-8%). The similar trend and effect of ESD are described by the simulation and experiment in comparison to conventional rudder and rudder-fin cases. Because of the appearance of a pair of fins and a bulb on the rudder, i.e. RBFs, (1-t) increases around 2%, (1-w) decreases 2% in simulation and 7% in experiment. As concluded for the error, ESD (1-w) trend also shows the major difference between experiment and simulation.

Table 4- 1 Self-propulsion factors

		1-t	1-w	η_H
EFD	Normal	0.7788	0.4468	1.7431
	Fin	0.7953	0.4251	1.8710
CFD	Normal	0.7643	0.4601	1.6612
	Fin	0.7797	0.4527	1.7222
E_{normal} (%)		1.87	-2.96	1.40
E_{fin} (%)		1.97	-6.51	7.96
D_{EFD} (%)		2.11	-4.87	7.34
D_{CFD} (%)		2.02	-1.59	3.67
D(%)=((Normal – Fin) / Normal) * 100 E(%)=((EFD – CFD) / EFD) *100				

4.1.2 More CFD Analysis

Computational self-propulsion factors are validated in the previous section while the detailed flow around the rudder-fin is analyzed in this section. Figure 4-3 plots the axial velocity contours limited to u/U_0=1.1 along several x/L_{PP} sections (x/L_{PP}=0.991~1.004) across the port side and starboard side fin.

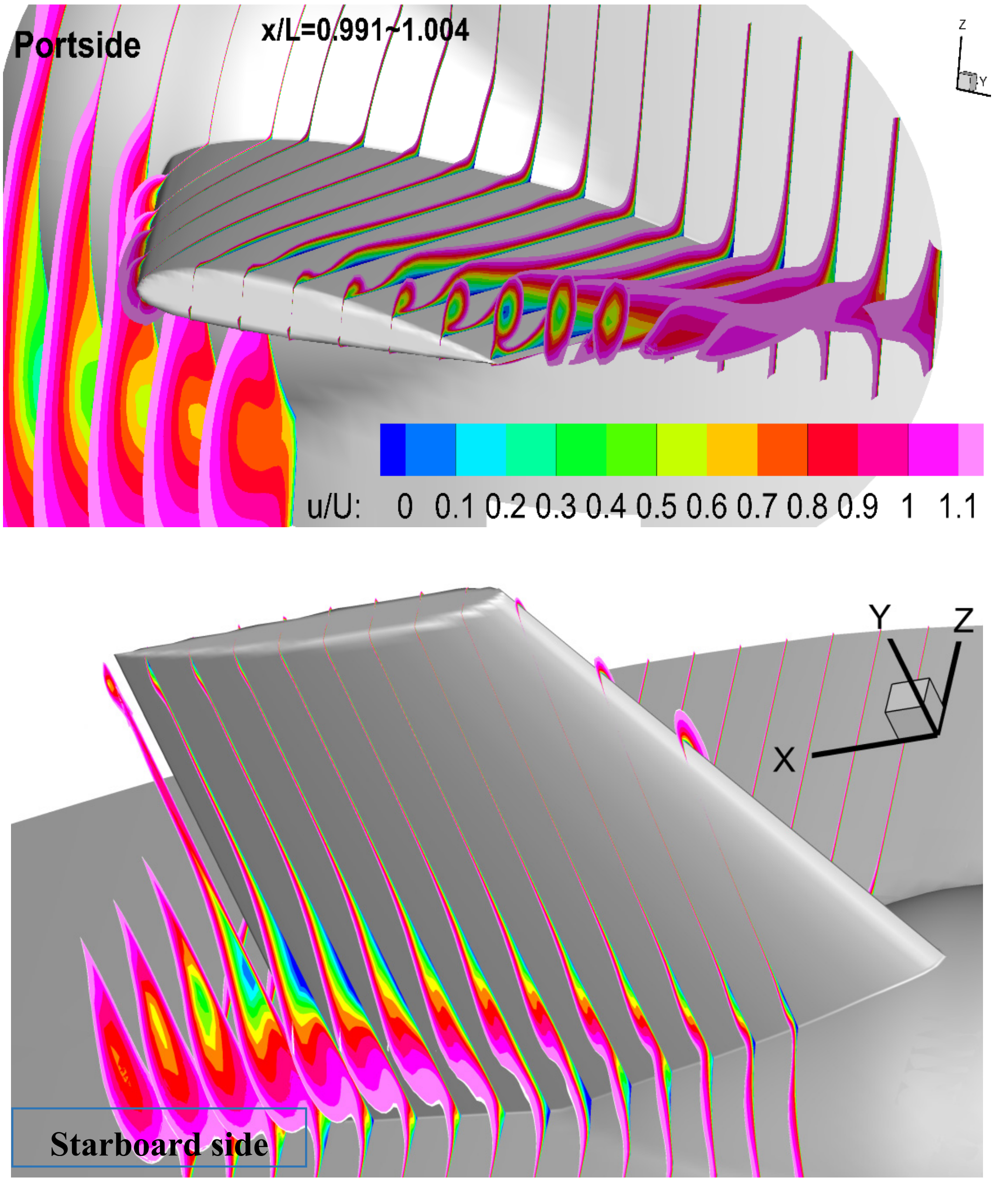

Figure 4- 3 Velocity sections along fin chord-wise direction

On the port side fin, the tip vortex shedding is clearly observed (a contour roll-up with a low velocity core in blue color). The positive pressure difference between upper and lower surfaces is pushing the fin upward. The fluid flows across from pressure side to suction side indicates a lift loss. The hub vortex is mainly attached under the port side fin whilst a part of hub vortex is separated under starboard side. On the other hand, a large area of flow separation under the starboard fin near the root appears. The starboard side tip-vortex is relatively smaller compared with the port side one. It implied the large drag on the fin. Thus, this ESD configuration is not an optimal design, especially for the starboard side fin. It is necessary to understand and improve the flow angle of attack into the fin.

In the following picture, the section is at $x/L_{PP}=1.025$ which layout is same as Figure 4-2. According to the contour color, the axial velocity (u/U_0) of the streamline decreases near the stern because of viscosity and hence accelerated by the propeller. The streamlines are rolled up due to propeller rotation and pass the fins toward the downstream. The flow accelerates passing the fins due to the curvature of the fin-foil as well. Streamlines near the fin-tip would flow into the concave shape of high speed region on the section $x/L_{PP}=1.025$

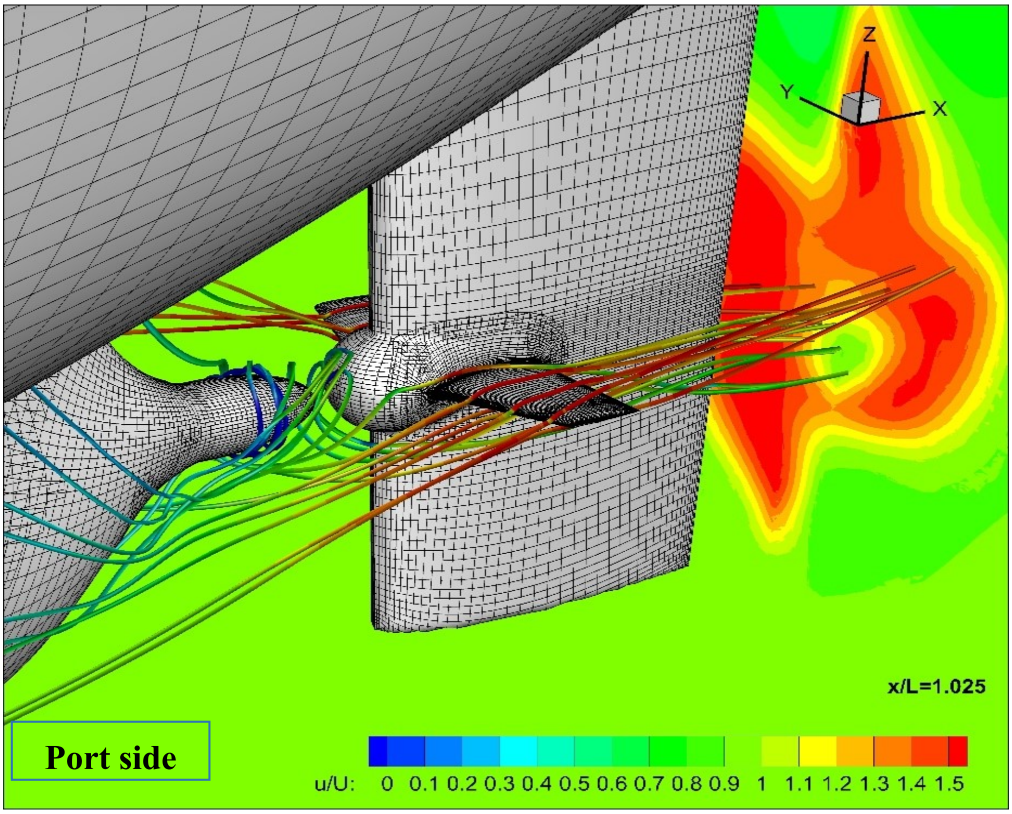

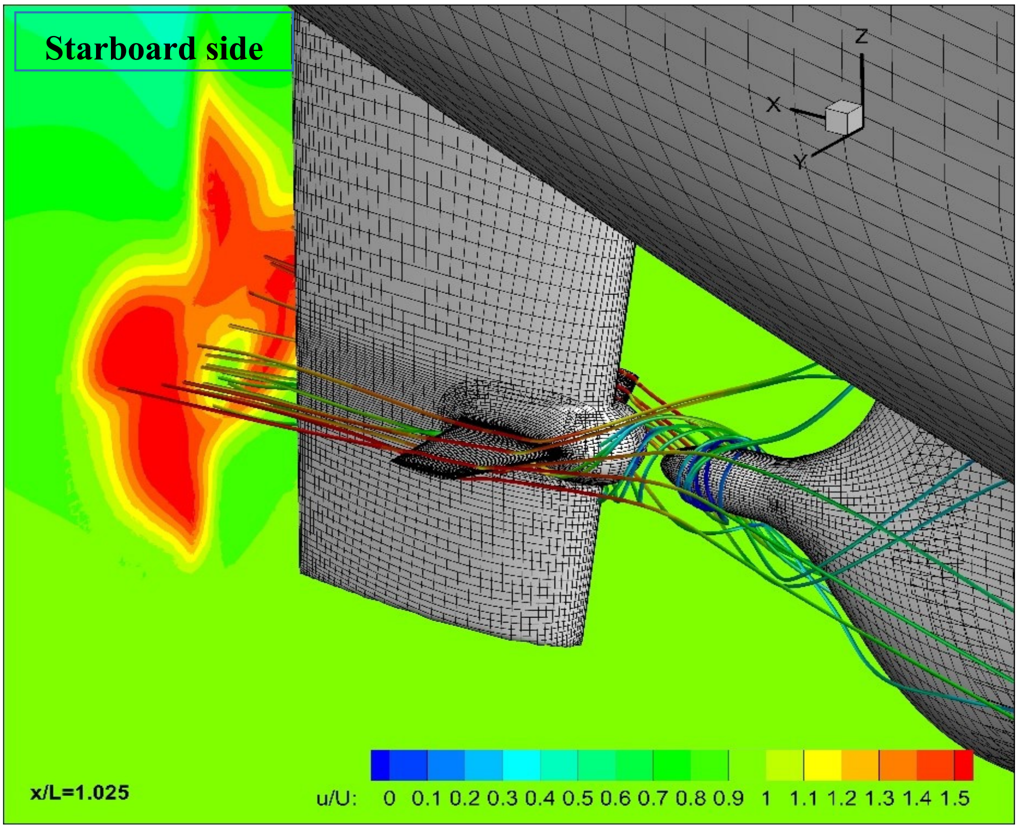

Figure 4- 4 Flow field at x/L_{PP}=1.025 and streamlines

4.2 The CFD results – Improvement of Rudder-Bulb-Fin system

4.2.1 Self-Propulsion Factors

The delivered power required by the propeller to achieve constant speed is given by the following equation (ITTC 2017).

$$P_D = \frac{R.V_S}{\eta_D} \tag{16}$$

Where R is the total resistance

V_S is the vessel speed

η_D is quasi-propulsive efficiency

The delivered power required by the propeller can be reduced as much as possible by three main options, hence resulting in low cost. Reducing the vessel speed is not feasible because it will affect the ship operation. The propeller quasi-propulsive coefficient is composed of hull, open water and relative rotative efficiencies. Besides open water and relative rotative efficiencies, hull efficiency also plays an important role on improvement of propulsion efficiency and protection of the marine environment. The hull efficiency is derived as $\eta_H = 1 - t / 1 - w$ where 1-*t* is the thrust deduction factor and 1-*w* is the wake fraction, and we know that a large thrust deduction factor and a small wake fraction are beneficial effect.

$$\eta_D = \eta_H.\eta_o.\eta_R \tag{17}$$

Where η_H : hull efficiency

η_o : open water efficiency

η_R : relative rotative efficiency

Calculating the total resistance of ship is the first step in order to estimate the required propulsive power, hence understanding of all components of ship resistance is important. The total resistance has many components in rough sea conditions but the main resistance (in this research) acting on the hull is frictional and viscous pressure. The air resistance on ship's above-water hull and superstructure is also ignored. The existence of fin is the cause of raising in the viscous pressure resistance but dropping in frictional resistance value or vice versa. The thickness and size of fin are considered since the appearance of fin accompanied in increasing wetted area. The total resistance with- (R_T) and without propeller (R_0) for model scale is calculated from the predicted total resistance coefficient (C_t) and the relationship is as follows:

$$R = \frac{1}{2} C_t . \rho . U_0^2 . A \tag{18}$$

$$K_T = \frac{T}{\rho n^2 D^4} \tag{19}$$

$$K_Q = \frac{Q}{\rho n^2 D^5} \tag{20}$$

In which, density ρ =998kg/m^3, A is the total surface wetted area for whole ship.

n is number of propeller revolution and D is propeller diameter

The propeller revolution rate equals 16.3 rps which is obtained by the self-propulsion test in the experiment with the fully loaded condition. The final converged thrust and torque coefficients are listed in Tables 4-2 ~ 4-4 to five-digit accuracy which are averaged from the simulate output. By substituting the values of K_T into Eq. 19, the thrust value is also provided in the following tables. While the torque is a function of rps which is 16.3rps for all simulations, the torque takes a constant value.

Table 4- 2 Thrust and torque for small and high changing AOA

Thrust and Torque	K_T	$10K_Q$	**Thrust (N)**
Small Changing AOA			
Ps-1_Sb-1	0.1970	0.2163	4.9381
Ps0_Sb-1	0.1969	0.2162	4.9356
Ps1_Sb-1	0.1978	0.2162	4.9589
Ps2_Sb-1	0.1970	0.2162	4.9359
Ps-1_Sb0	0.1969	0.2163	4.9353
Ps0_Sb0	0.1971	0.2162	4.9393
Ps1_Sb0	0.1975	0.2162	4.9497
Ps2_Sb0	0.1971	0.2162	4.9384
Ps-1_Sb1	0.1970	0.2162	4.9369
Ps0_Sb1	0.1979	0.2163	4.9590
Ps1_Sb1	0.1978	0.2162	4.9568
Ps2_Sb1	0.1969	0.2162	4.9349
Ps-1_Sb2	0.1970	0.2162	4.9365
Ps0_Sb2	0.1970	0.2162	4.9373
Ps1_Sb2	0.1979	0.2163	4.9585
Ps2_Sb2	0.1970	0.2163	4.9375
Ps0_Sb6	0.1975	0.2162	4.9497

For small changing AOA group, with a highest value of thrust coefficient and the lowest resistance, ps0_sb1 (0-degree for port side and rotated 1-degree up for starboard side) design is implying the largest extra thrust and improve the self-propulsion which are shown at the end of this section. Compared with the resistance for conventional rudder case, the resistance of the ps0_sb1 design is reduced by 2.3% (whereas R_T of normal fin can be reduced 1.8 percent)

Table 4- 3 Thrust and torque for twisted fin and cutting starboard fin

Thrust and torque	K_T	$10K_Q$	**Thrust (N)**
Twisted fin	0.1976	0.2162	4.9522
Cutting starboard fin			
Cut0.008	0.1978	0.2163	4.9581
Cut0.007	0.1979	0.2163	4.9585
Cut0.005	0.1978	0.2163	4.9570

Table 4- 4 Thrust and torque for NACA5412

Thrust and torque	K_T	$10K_Q$	**Thrust (N)**
NACA5412			
NACAps0_sb0	0.1977	0.2163	4.9557
NACAps0_sb1	0.1977	0.2163	4.9556
NACAps0_sb6	0.1976	0.2162	4.9518
NACAps1_sb1	0.1977	0.2163	4.9555
NACAps6_sb6	0.1977	0.2163	4.9546
NACA5412 + New Position of Port Fin			
NACAps0-sb0_0.004z0.003x	0.1979	0.2163	4.9595
NACAps0-sb6_0.004z0.003x	0.1979	0.2164	4.9607
NACAps6-sb6_0.004z0.003x	0.1980	0.2164	4.9615

Based on the value of total resistance which is provided by computational output and EFD open water characteristics curve, the self-propulsion factors were determined by Eqs 21~23 and the value illustrated in Figs 4-6 ~ 4-8.

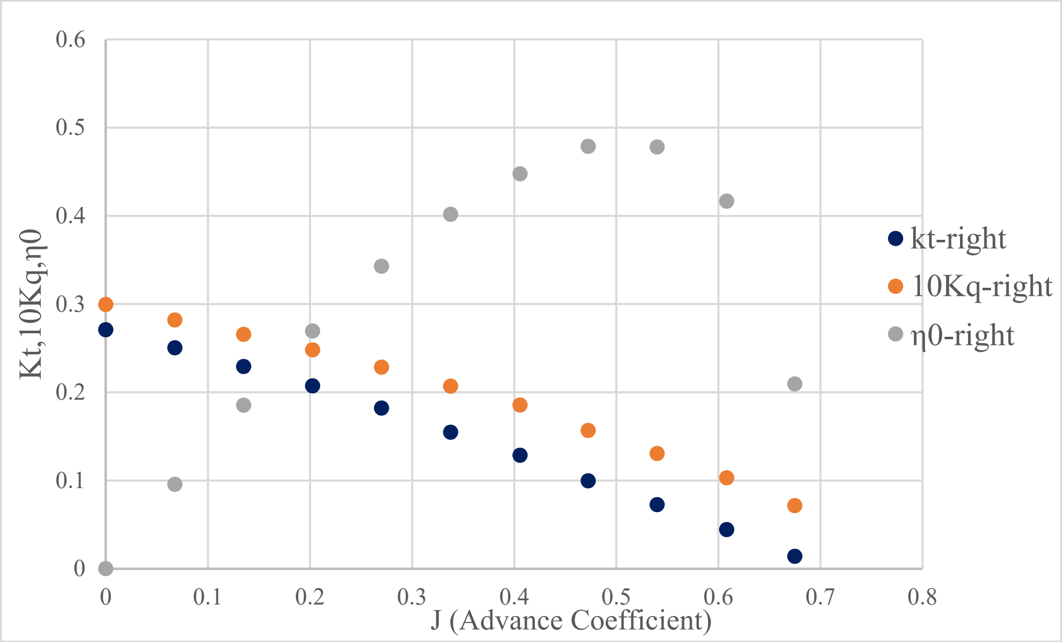

Figure 4- 5 Open water characteristics curve of KVLCC2 clockwise propeller provided by Kishi

$$t = \frac{R_T - R_0}{T} \tag{21}$$

$$1 - w = \frac{J_a}{J_s} \tag{22}$$

$$J_s = \frac{V_s}{nD} \tag{23}$$

Where R_T is total resistance with propeller

R_0 is total resistance in the case of absence propeller

J_a and J_s are the advanced coefficients; J_a is obtained from the open water characteristics curve while J_s equals 0.495

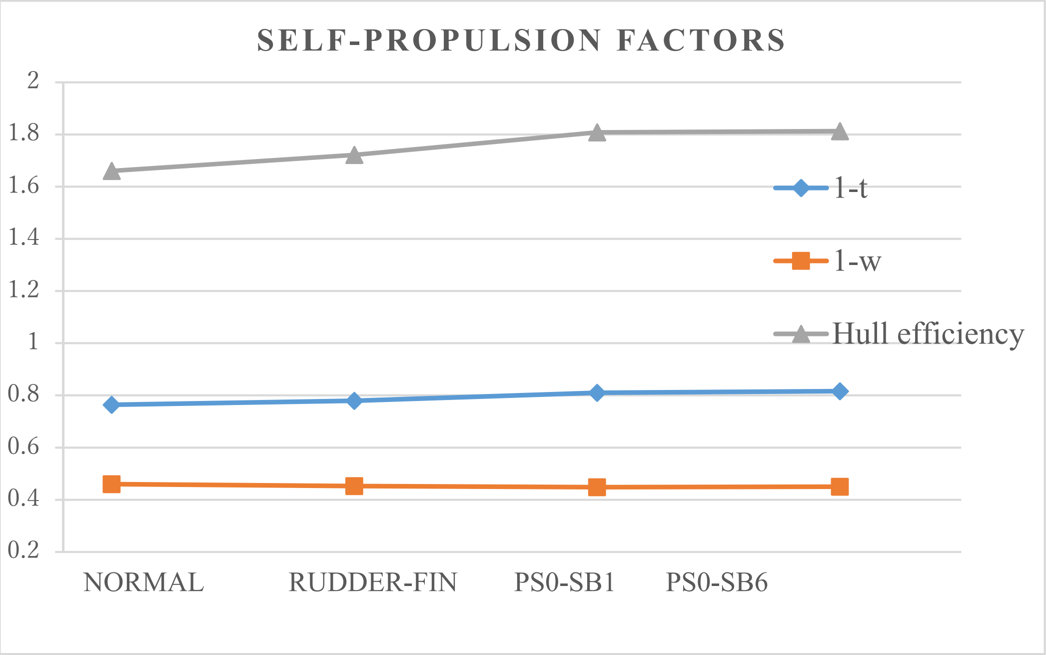

Figure 4- 6 Self-propulsion factors comparison among conventional rudder, rudder-fin, ps0-sb1 and ps0-sb6

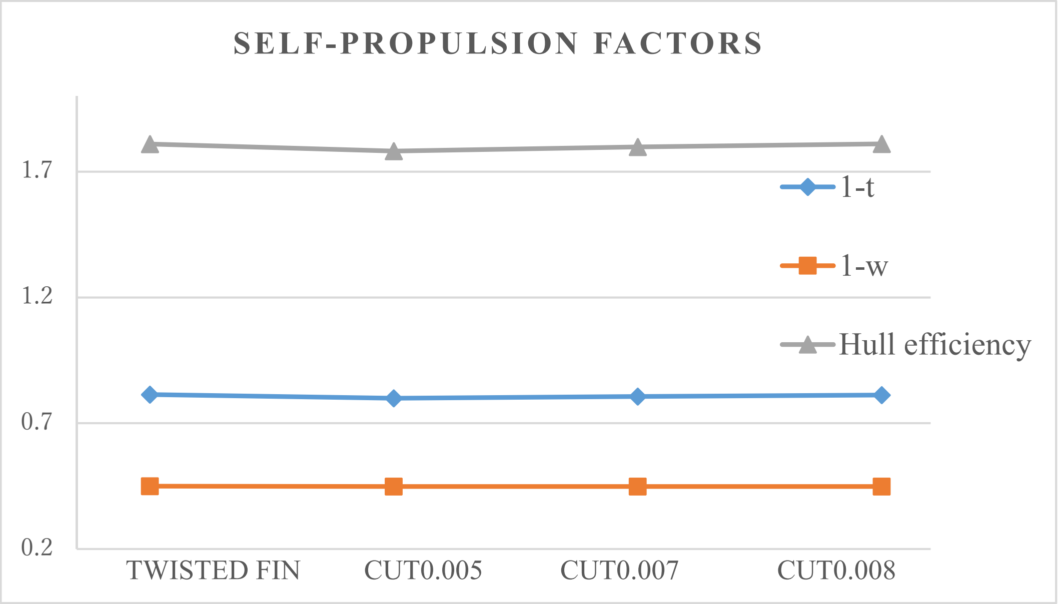

Figure 4- 7 Self-propulsion factors comparison among twisted fin, cut0.005, cut0.007 and cut0.008

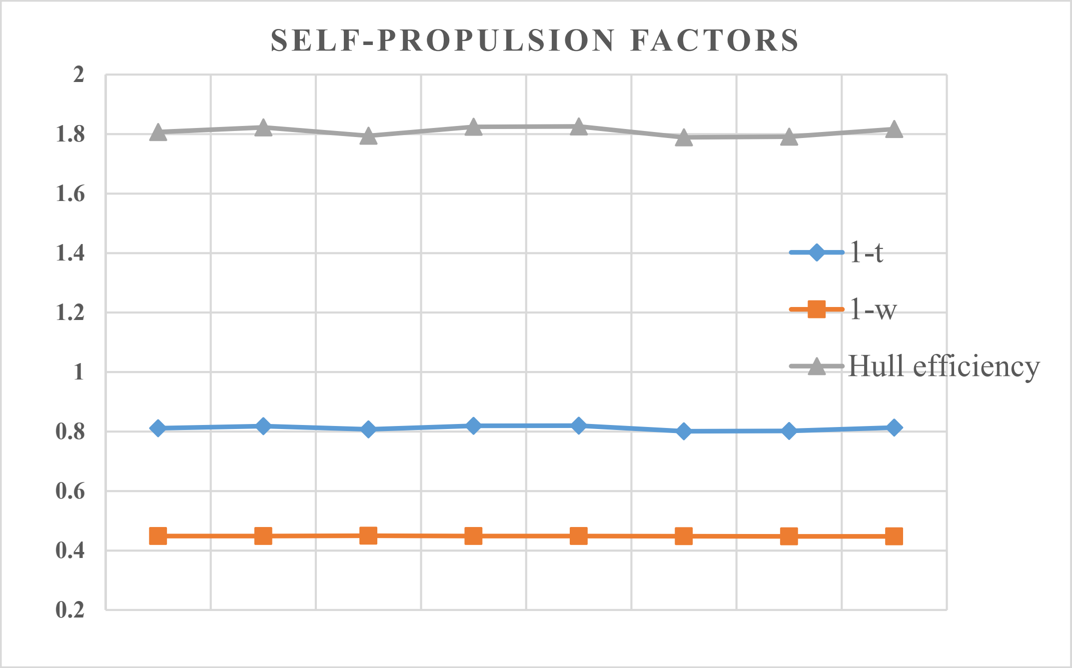

[left to right; NACAps0_sb0, NACAps0-sb1, NACAps0-sb6, NACAps1_sb1, NACAps6-sb6, NACAps0-sb0_0.004z0.003x, NACAps0-sb6_0.004z0.003x, NACAps6-sb6_0.004z0.003x]

Figure 4- 8 Self-propulsion factors comparison among NACA5412 cases

The line graph in Figs. 4-6~4-8 illustrates the self-propulsion factors for conventional rudder, twisted fin, changing attack angle group, cutting starboard side fin group, NACA5412 group cases. The wake factor values remained almost steady for all designs. Thus, an excessive variation in hull efficiency value among those cases is the result of different thrust deduction. The total resistance of NACAps6-sb6 case with propeller could be reduced by 4.36 percent with changes in increasing of (*1-t*) factor, 5.25% and decreasing of (*1-w*) factor by 0.78 percent. Thus, the hull efficiency value of NACAps6_sb6 is highest thus far, in comparison with normal fin. The design with new location of port side fin also proved as one of the optimal designs with high hull efficiency. Flow visualization provides a comprehensive understanding about flow around ship stern in the event of having a pair of horizontal fins and its improvement which is showed in next sections.

4.2.2 Flow field

In fact, many options to choose stations in order to analysis the wake field behind the rotating propeller; in this research, the main interest to show flow field is the downstream area at $x/L_{PP}=1$ (AP) and $x/L_{PP}=1.025$ (behind the trailing edge of rudder) whereas the propeller center is located at the station of $x/L_{PP}=0.9875$. The Figs 4-9 ~ 4-21 show the axial velocity contours (u/U_0) and cross flow vector (v/U_0, w/U_0) for high changing AOA, twisted fin, cutting starboard side, NACA5412 with different changing AOA and position of fin cases. The axial velocities are accelerated by the propeller to 1.6 times ship speed. The basis flow features were similar for almost cases, since the geometries are slightly changed only. Generally, the flow is moving up on port side and down on starboard side due to the propeller rotation. However, the flow at the region around starboard fin-tip trends to going up. From this point of view, the idea of making shorter starboard side fin is considered. The hub vortex would trend to move to the left side and its location is lower due to the rotating hub and bulb. Also, the propeller rotational flow vortex attaches on the port side surface on the rudder and a downward flow is caused on the starboard side surface. The vortices are truncated by the fins, especially the starboard side one. Two eddies appear on the lower and upper starboard fin, a bit away from the rudder, e.g. $y/L_{PP}\sim0.01$, is induced by the downward flow. Some of those designs had been validated by EFD, e.g., ps0-sb1, ps0-sb6 and cut0.008, and further data are available for particular cases which are presented at Appendix A. On the contrary, the result of the rest cases has not been validated by EFD but the accuracy of the numerical method for the similar object had already been proved by comparing with the experimental data which were shown in sections above.

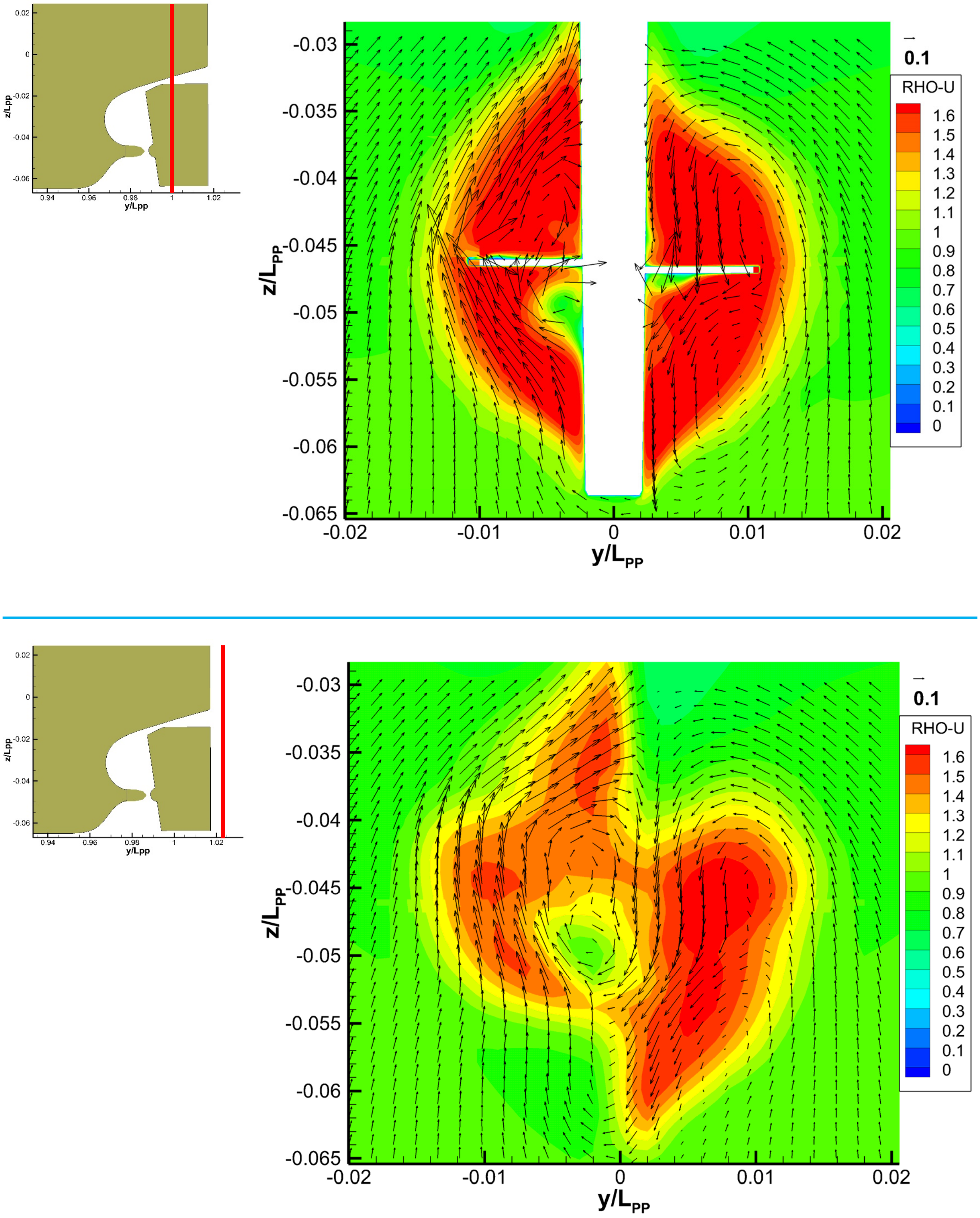

Figure 4- 9 Axial velocity profiles and cross flow vector at x/L$_{PP}$=1 and x/L$_{PP}$=1.025 for ps0-sb6 [looking from stern to bow]

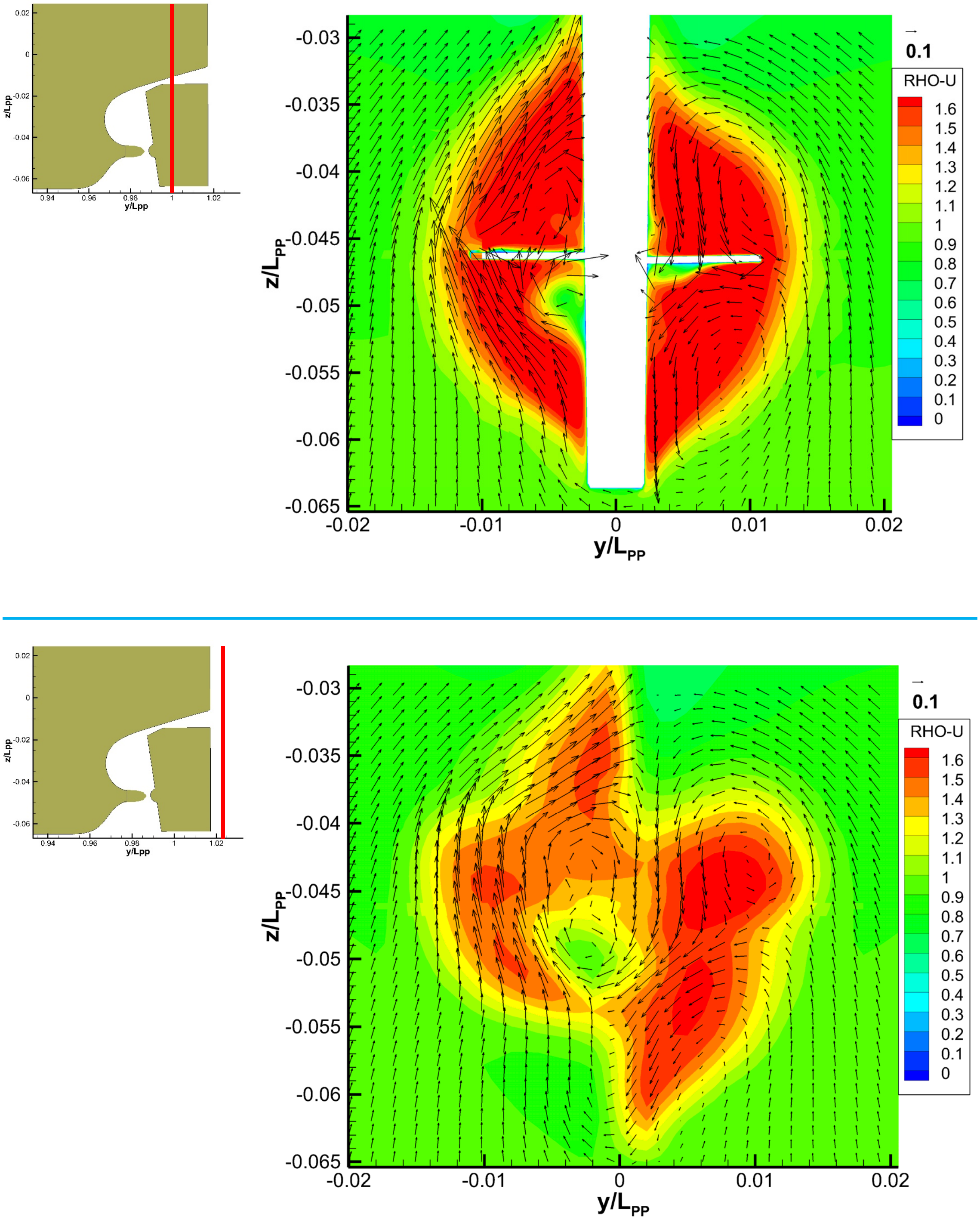

Figure 4- 10 Axial velocity profiles and cross flow vector at x/LPP=1 and x/LPP=1.025 for twisted fin [looking from stern to bow]

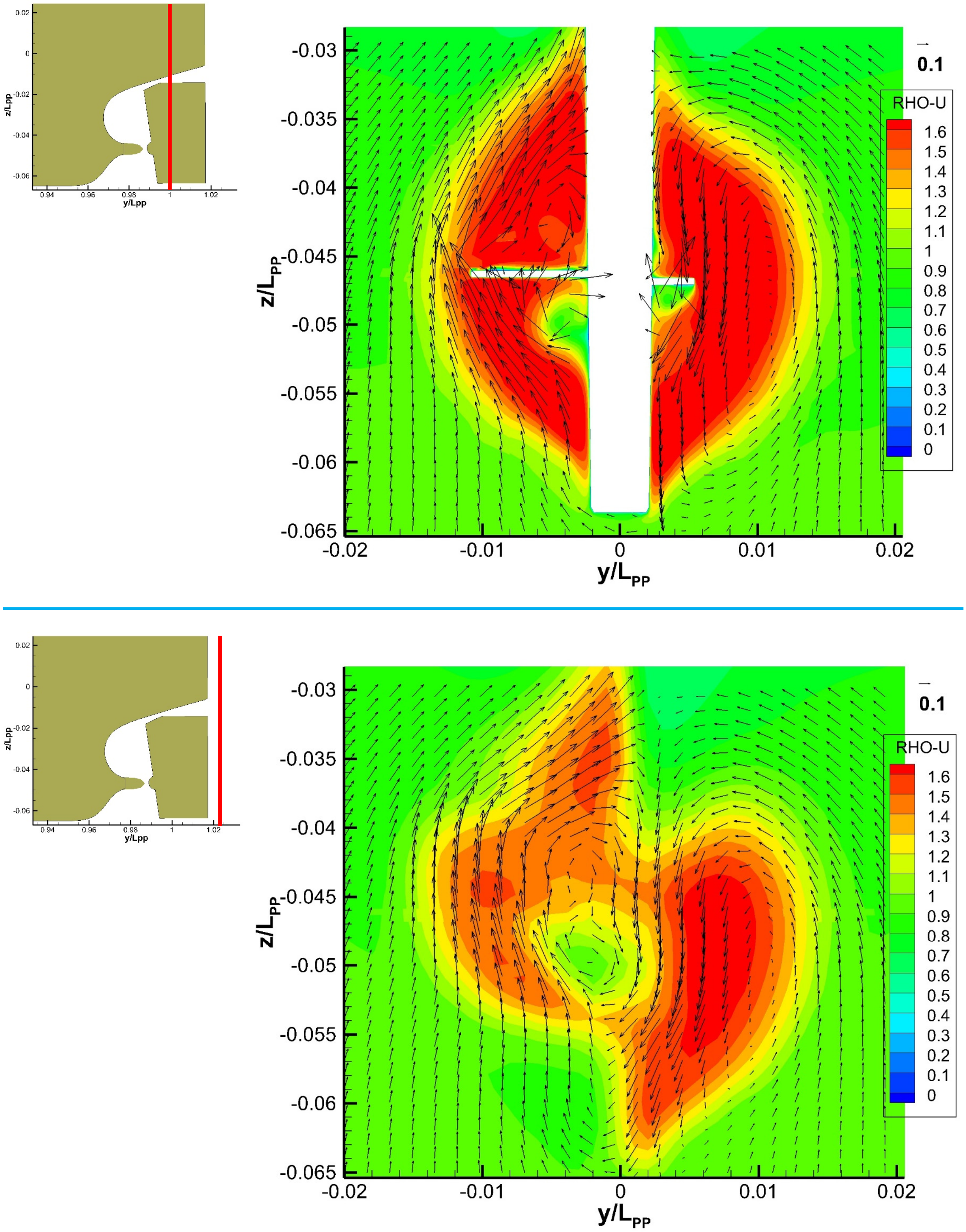

Figure 4- 11 Axial velocity profiles and cross flow vector at $x/L_{PP}=1$ and $x/L_{PP}=1.025$ for fin-cut0.005 [looking from stern to bow]

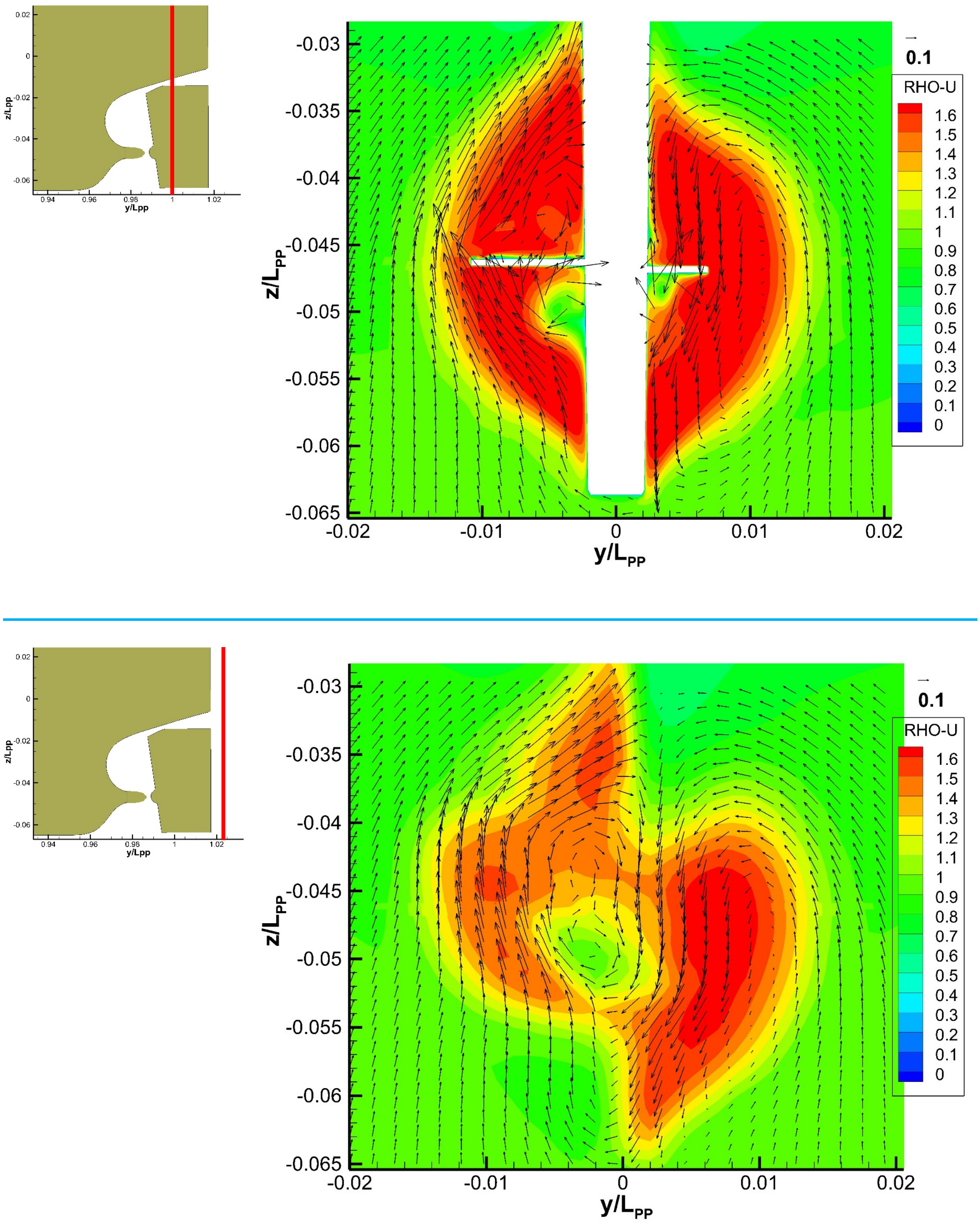

Figure 4- 12 Axial velocity profiles and cross flow vector at $x/L_{PP}=1$ and $x/L_{PP}=1.025$ for fin-cut0.007 [looking from stern to bow]

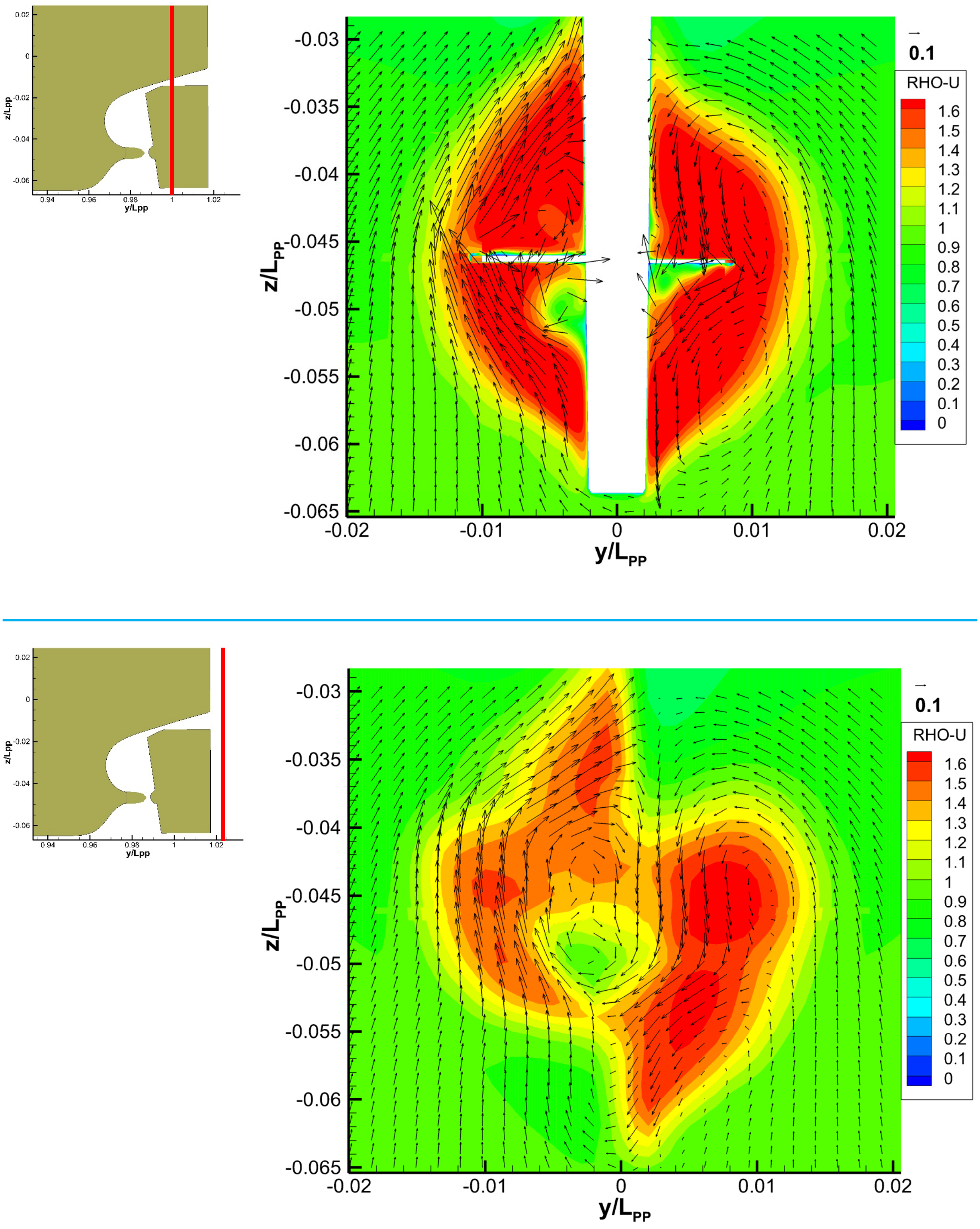

Figure 4- 13 Axial velocity profiles and cross vector at x/LPP=1 and x/LPP=1.025 for fin-cut0.008 [looking from stern to bow]

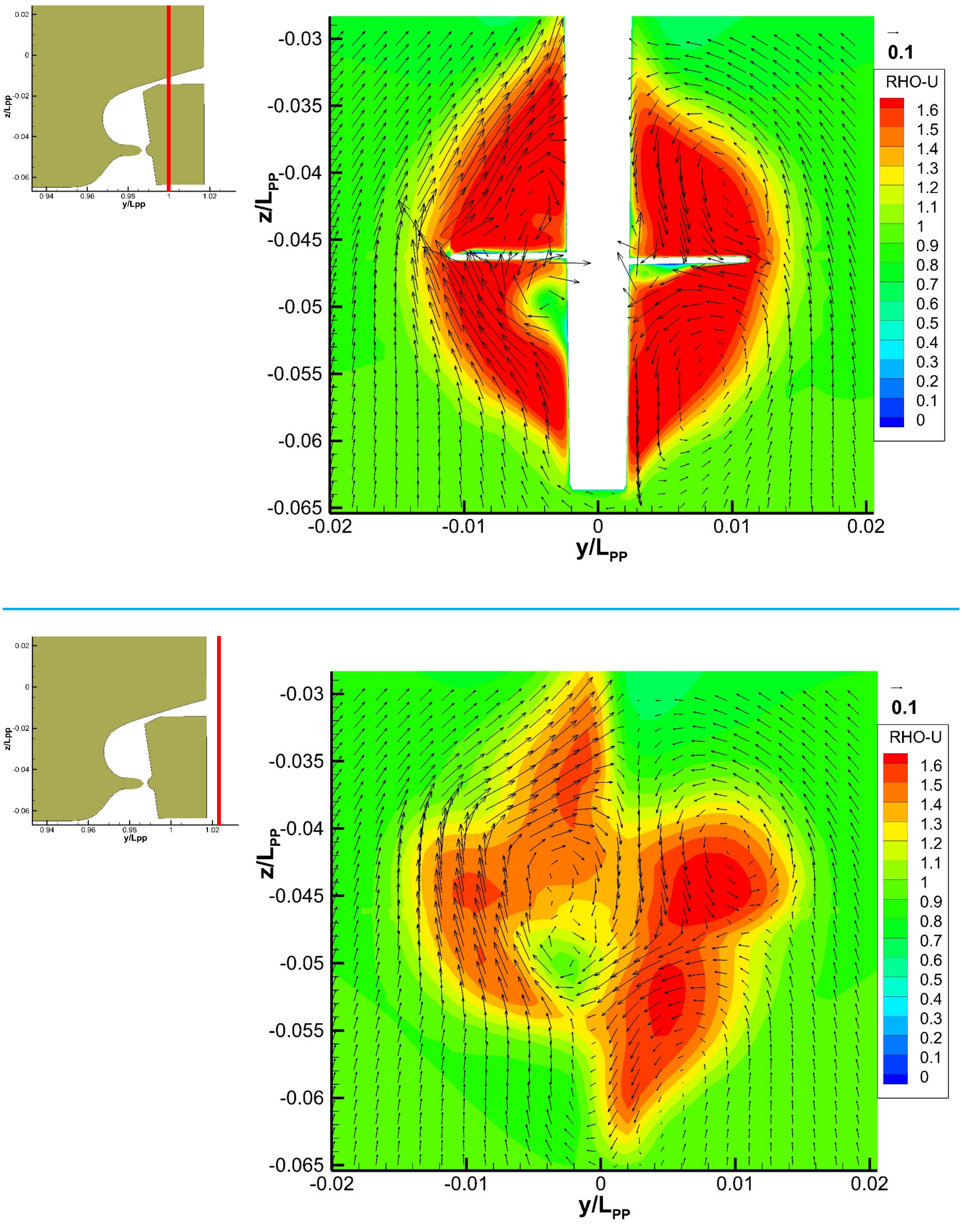

Figure 4- 14 Axial velocity profiles and cross flow vector at $x/L_{PP}=1$ and $x/L_{PP}=1.025$ for NACAps0_sb0 [looking from stern to bow]

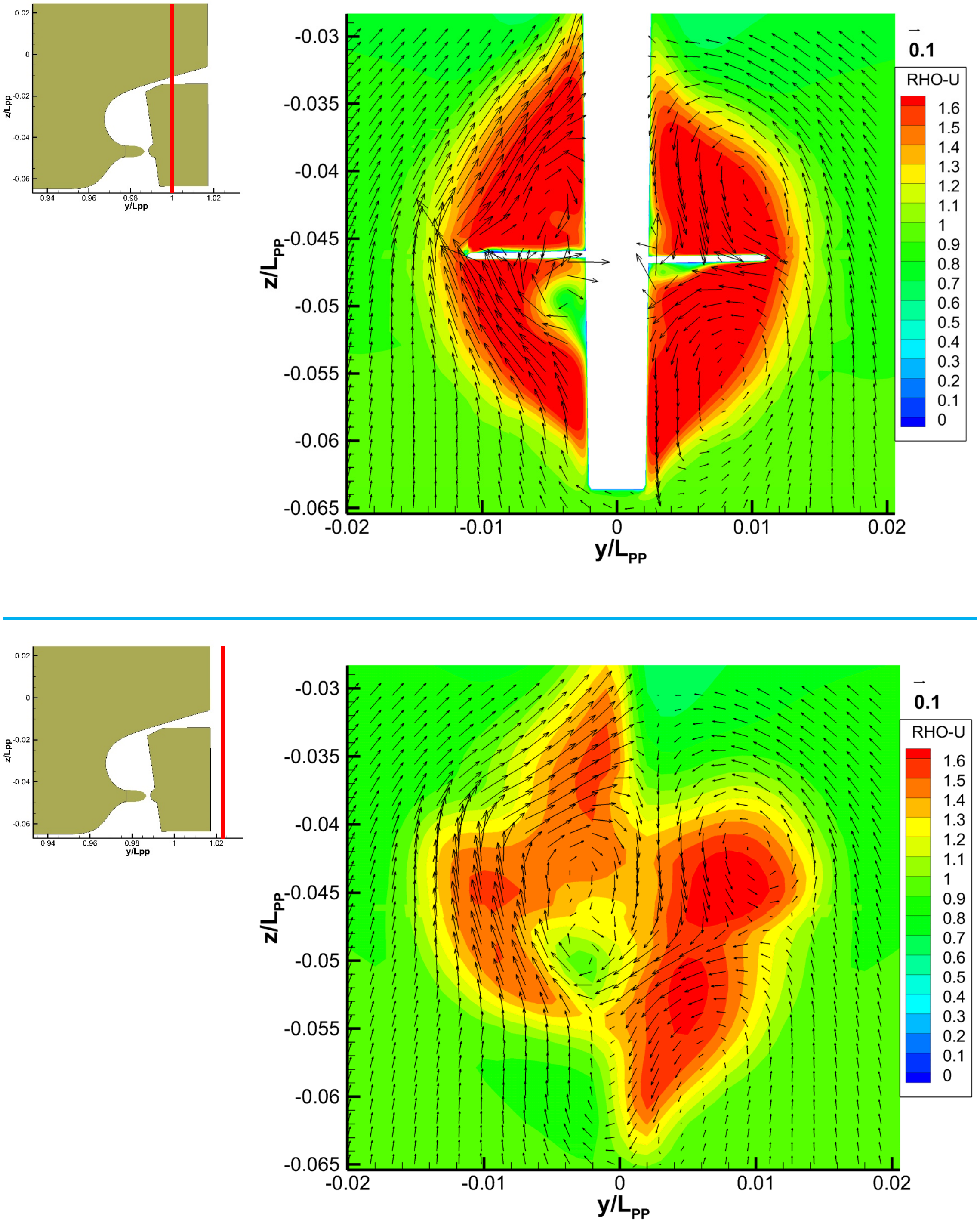

Figure 4- 15 Axial velocity profiles and cross flow vector at x/LPP=1 and x/LPP=1.025 for NACAps0_sb1 [looking from stern to bow]

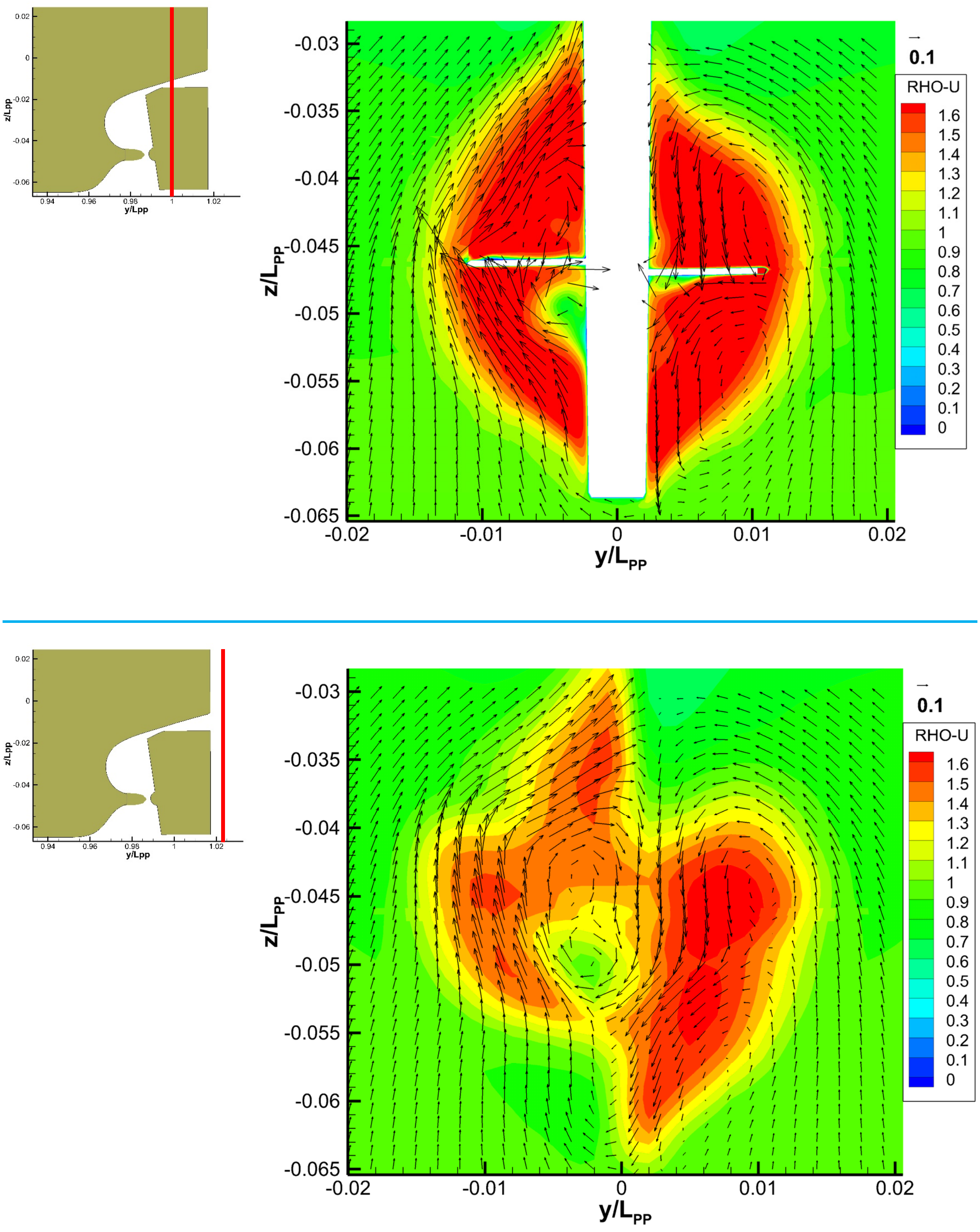

Figure 4- 16 Axial velocity profiles and cross flow vector at $x/L_{PP}=1$ and $x/L_{PP}=1.025$ for NACAps0_sb6 [looking from stern to bow]

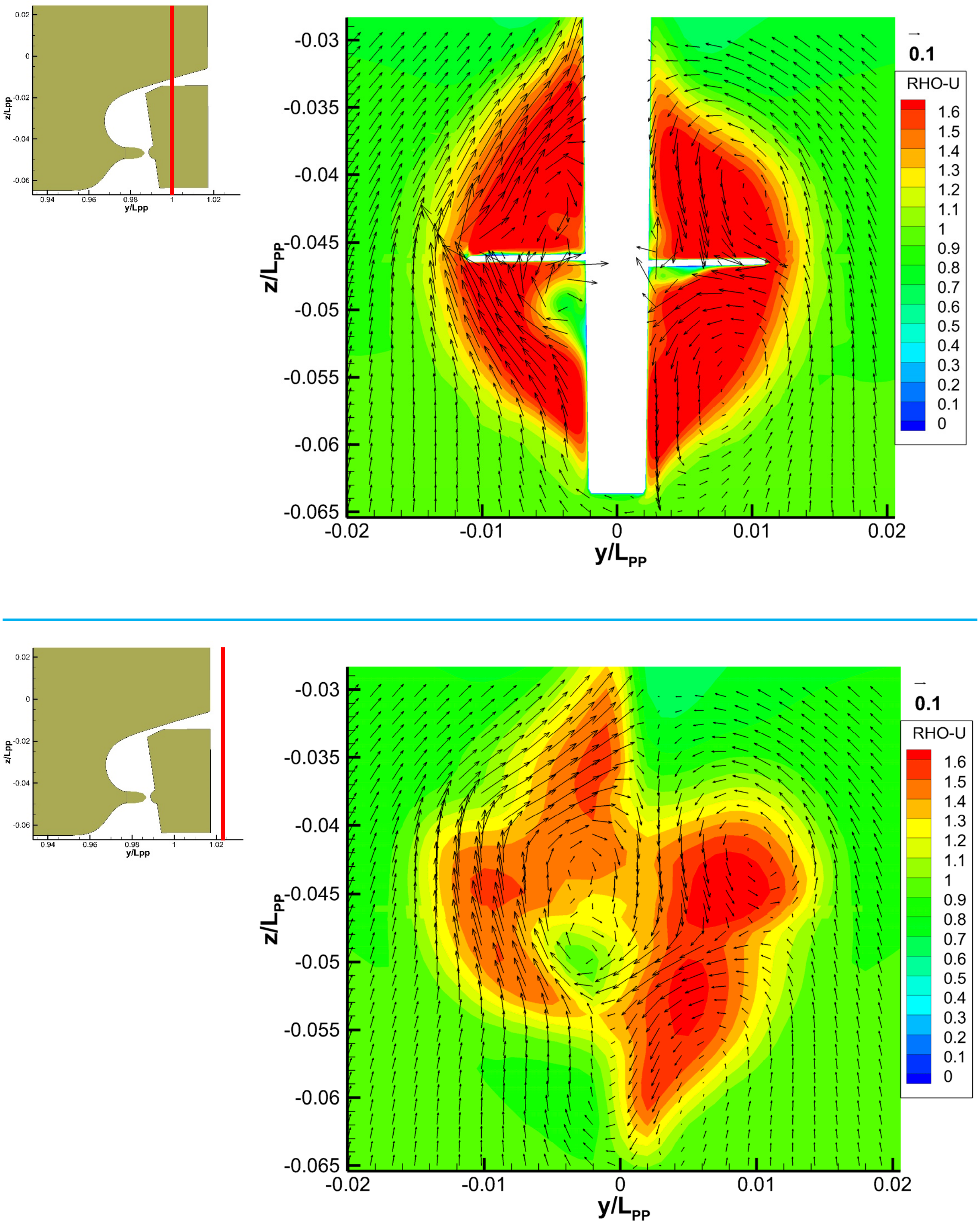

Figure 4- 17 Axial velocity profiles and cross flow vector at x/LPP=1 and x/LPP=1.025 for NACAps1_sb1 [looking from stern to bow]

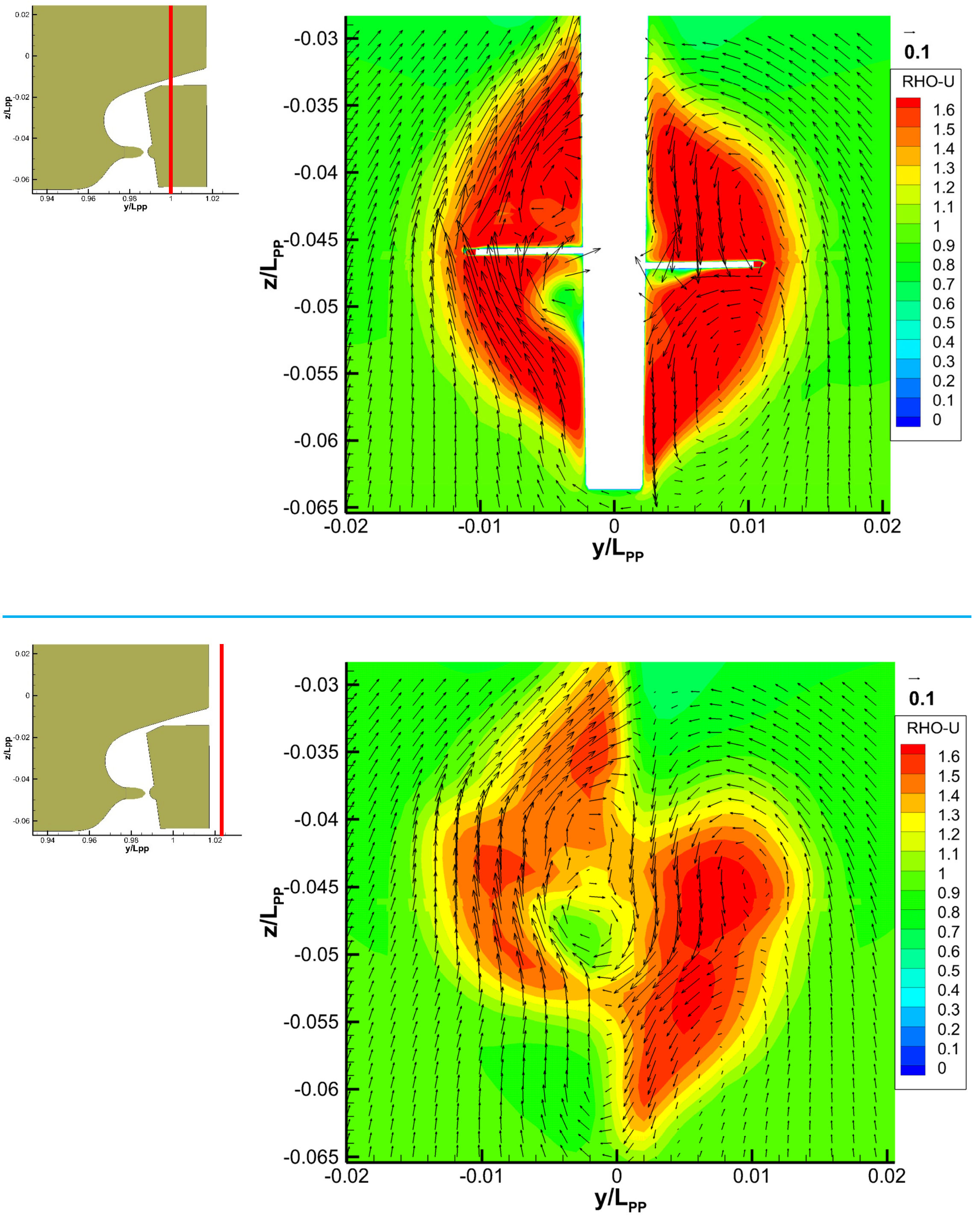

Figure 4- 18 Axial velocity profiles and cross flow vector at x/LPP=1 and x/LPP=1.025 for NACAps6_sb6 [looking from stern to bow]

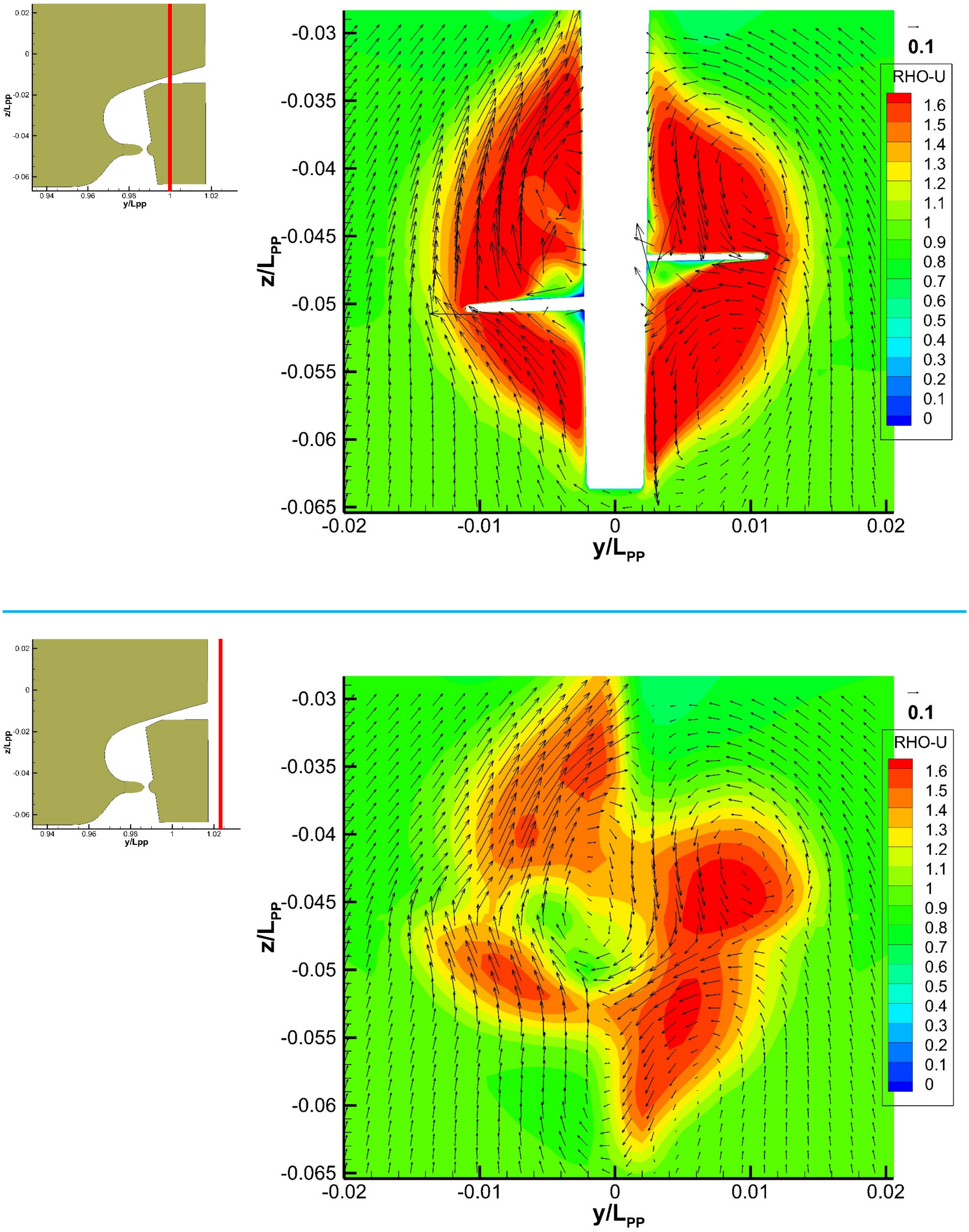

Figure 4- 19 Axial velocity profiles and cross flow vector at x/LPP=1 and x/LPP=1.025 for NACAps0-sb0_0.004z0.003x [looking from stern to bow]

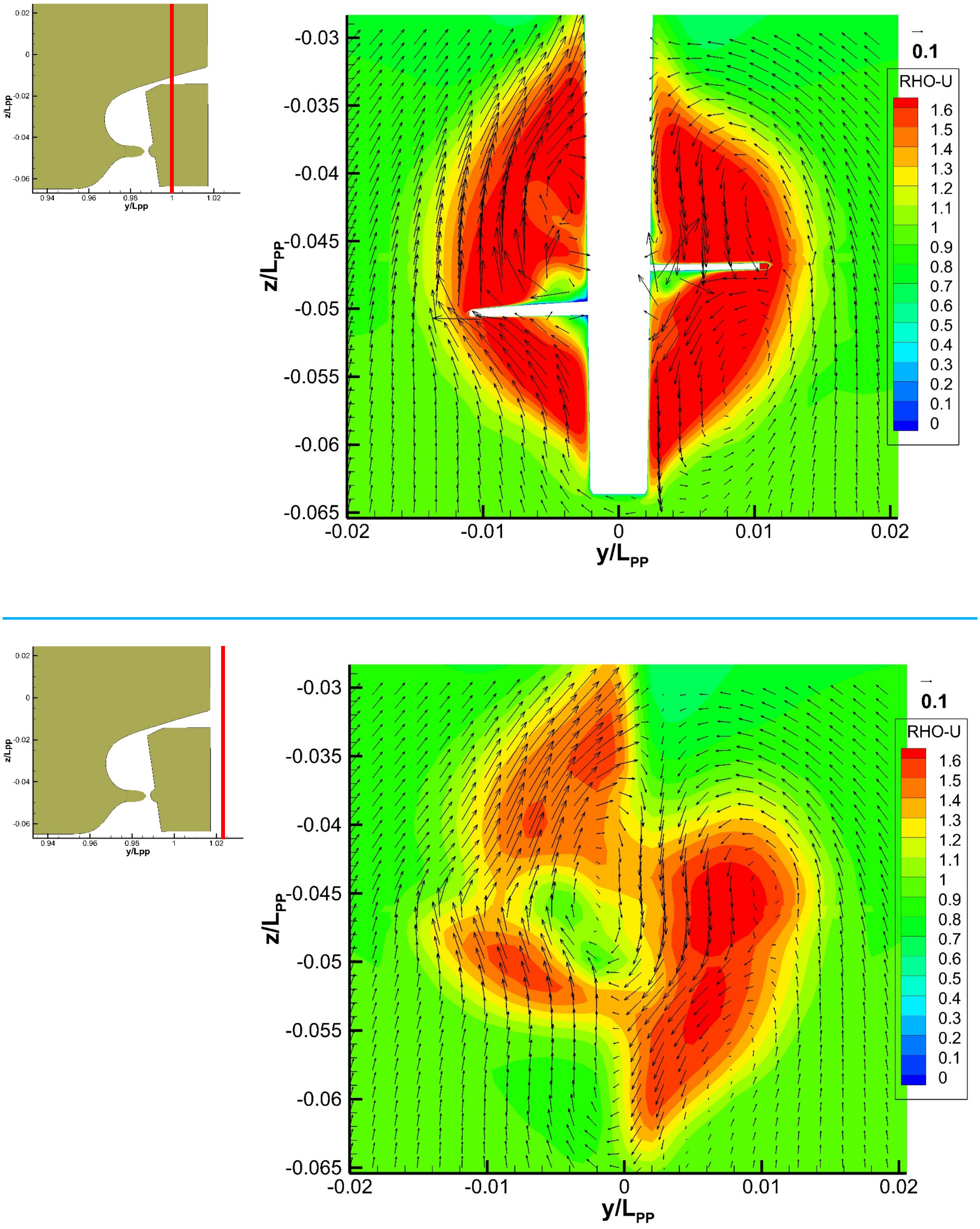

Figure 4- 20 Axial velocity profiles and cross flow vector at x/LPP=1 and x/LPP=1.025 for NACAps0-sb6_0.004z0.003x [looking from stern to bow]

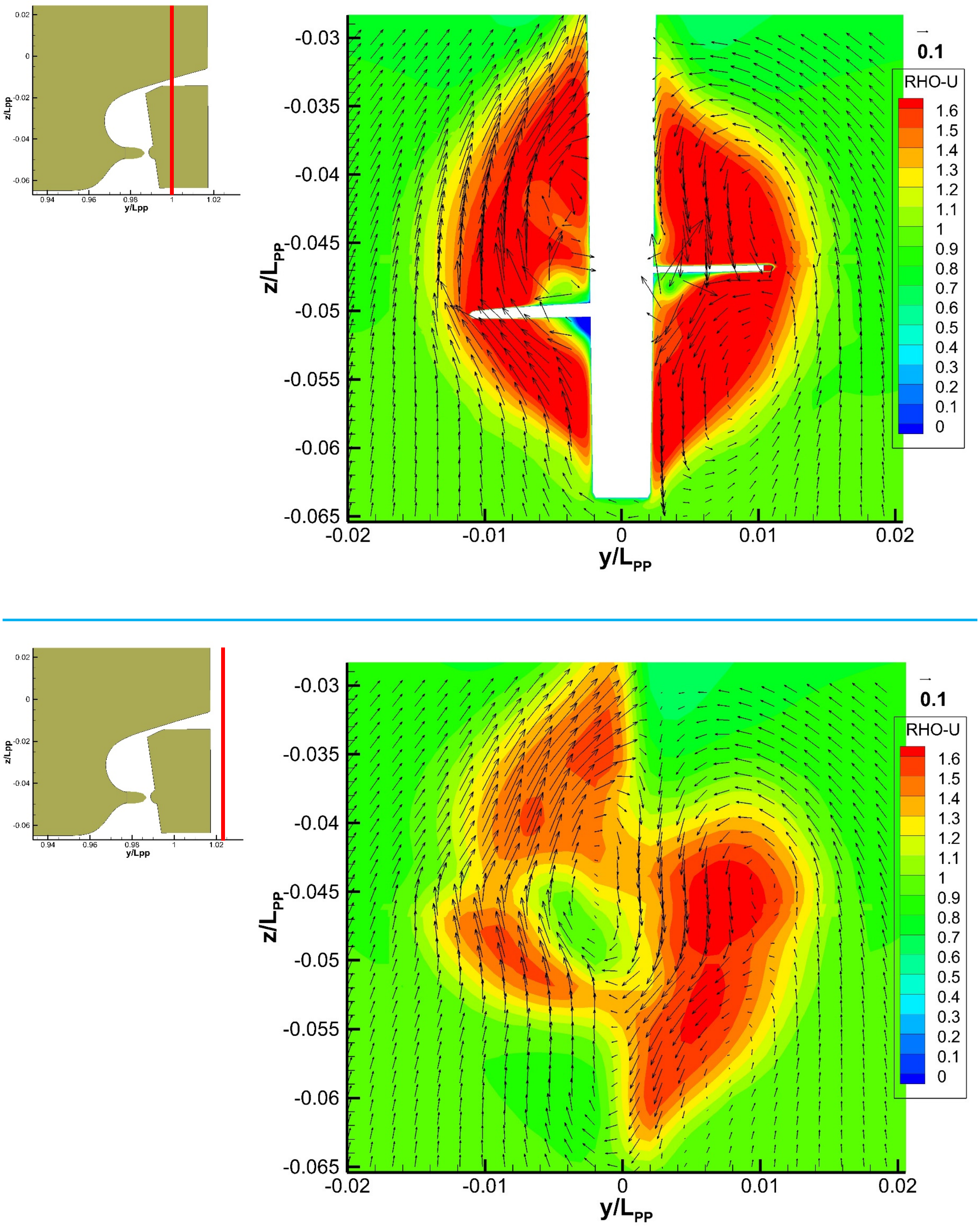

Figure 4- 21 Axial velocity profiles and cross flow vector at x/LPP=1 and x/LPP=1.025 for NACAps6-sb6_0.004z0.003x [looking from stern to bow]

Flow separation has been added in this section as more evidence in order to further strengthen persuasiveness of this study. The flow separation on boundary layer occurs whenever the change in either magnitude or direction of velocity of the fluid. The flow angle might be too large for the fluid to adhere to the fin's surface. Small flow separation means smaller drag and flow field is improved. Figs 4-22 ~ 4-28 show the axial velocity contour (u/U_0) on the sections from y/L_{PP} =0.004 to 0.009 along the fin span-wise direction for starboard side fin of all the cases. The huge flow separations occurred at the middle. The dark blue area (arrow in black in Fig. 4-22) indicates large flow separation and reverse flow. When comparing the size of dark blue area, it is obvious that on section y/L_{PP}=0.00525, the flow separation is smaller for twisted fin and cutting starboard side cases and completely disappear in all the designs of high changing AOA, and of course resulting in reducing drag, as was proved through all factors in the previous sections.

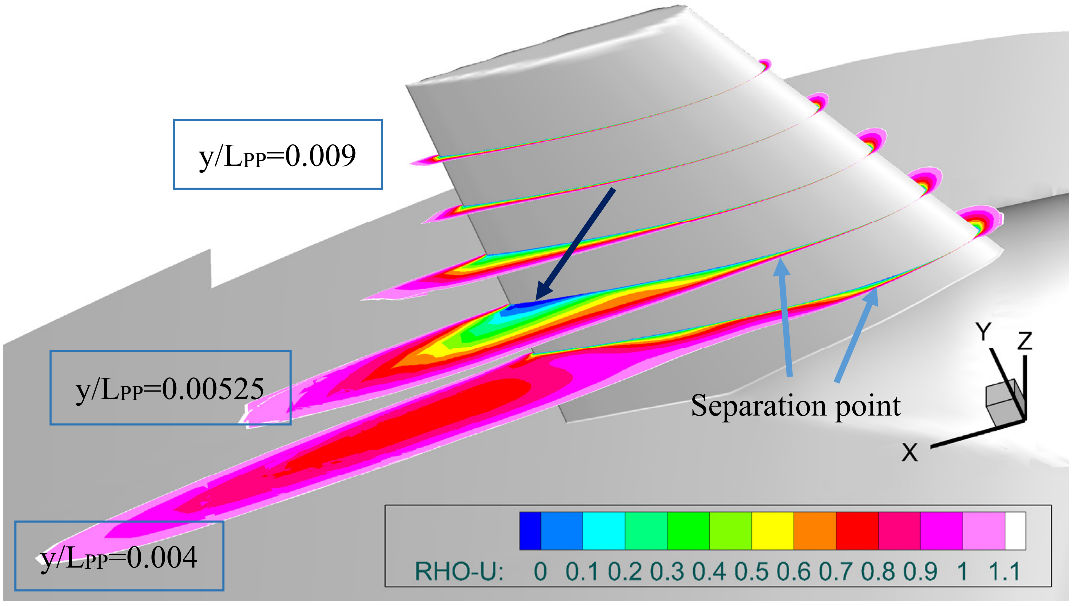

Figure 4- 22 Velocity sections along fin span-wise direction for ps0-sb0

($u/U_0 > 1.1$ flood contour was cut off)

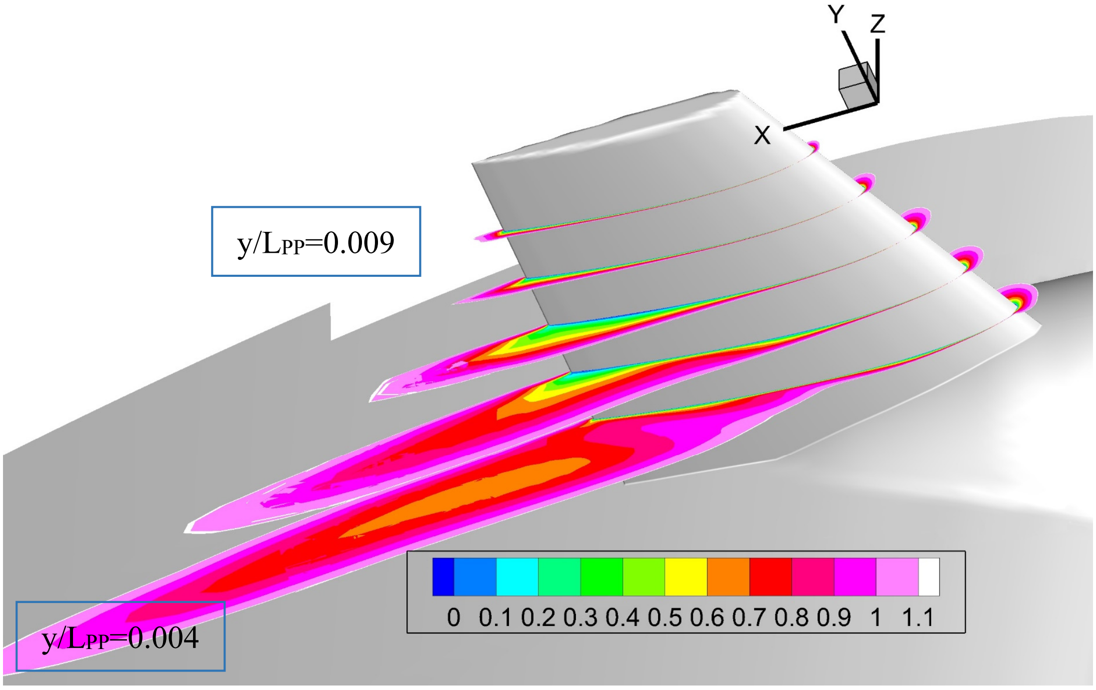

Figure 4- 23 Velocity sections along fin span-wise direction for ps0-sb1

(u/U_0 >1.1 flood contour was cut off)

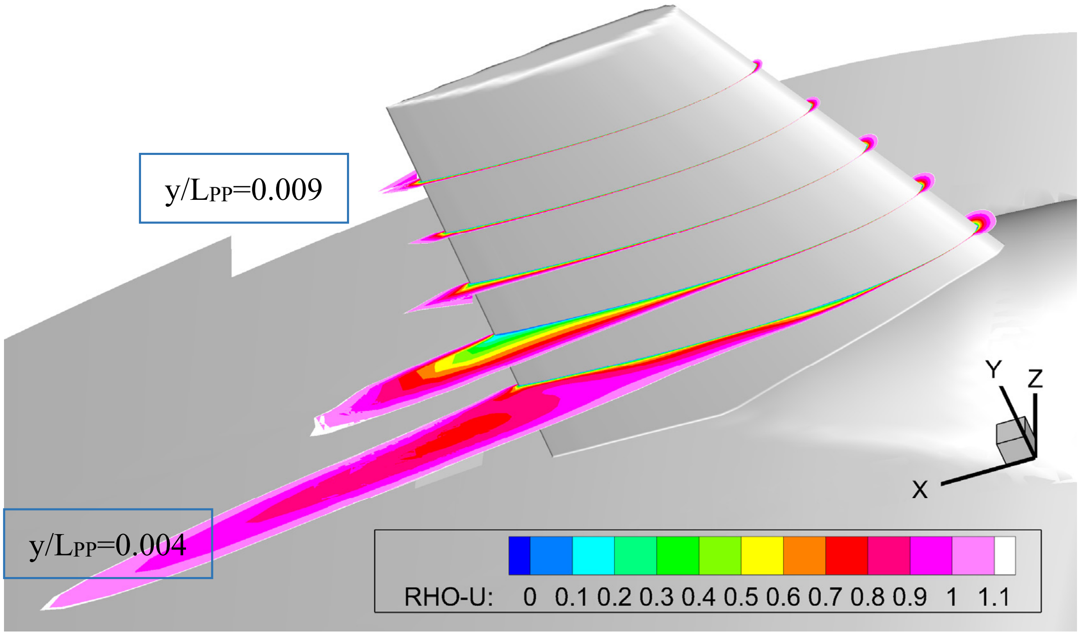

Figure 4- 24 Velocity sections along fin span-wise direction for ps0-sb6

(u/U_0 > 1.1 flood contour was cut off)

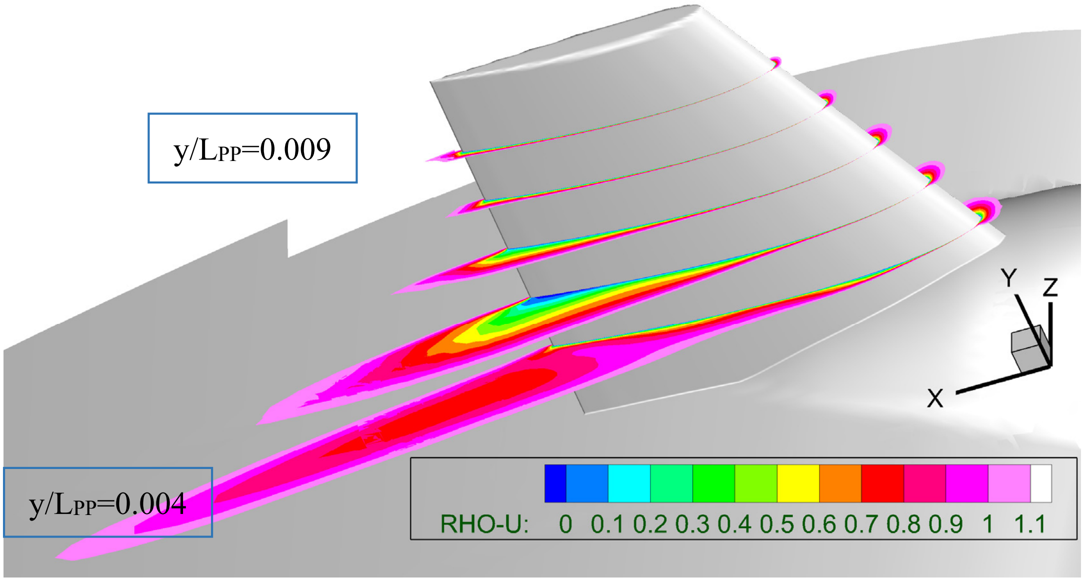

Figure 4- 25 Velocity sections along fin span-wise direction for twisted fin

(u/U_0 > 1.1 flood contour was cut off)

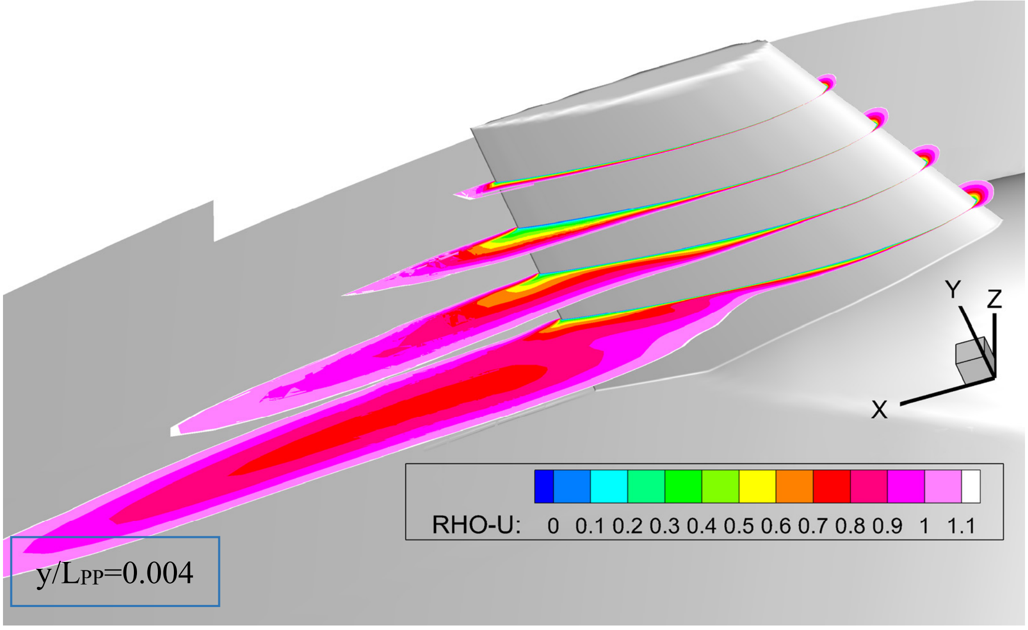

Figure 4- 26 Velocity sections along fin span-wise direction for cut0.008

(u/U_0 > 1.1 flood contour was cut off)

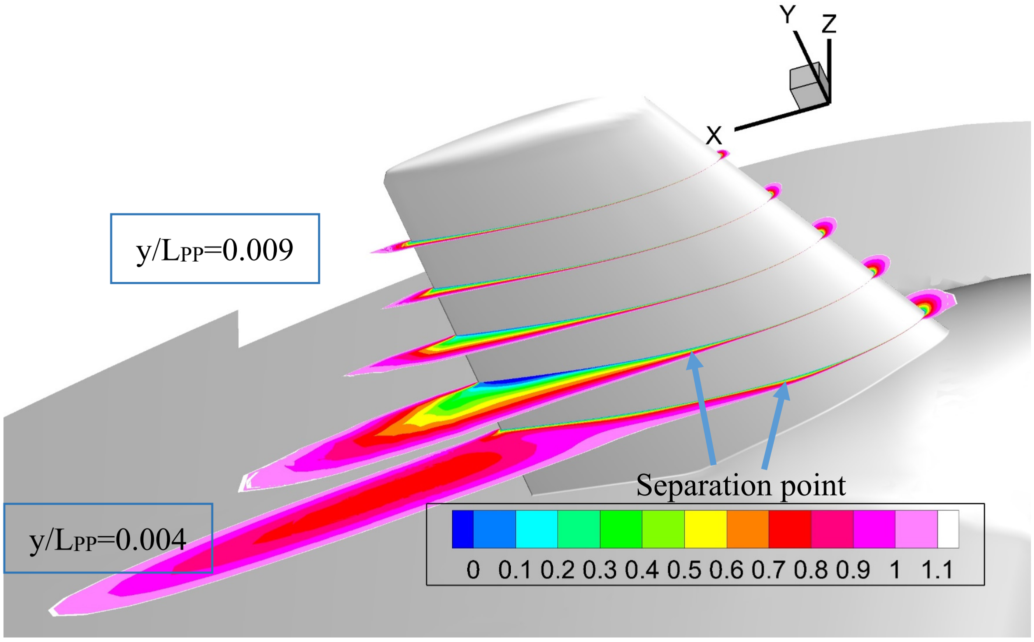

Figure 4- 27 Velocity sections along fin span-wise direction for NACAps0-sb0

($u/U_0 > 1.1$ flood contour was cut off)

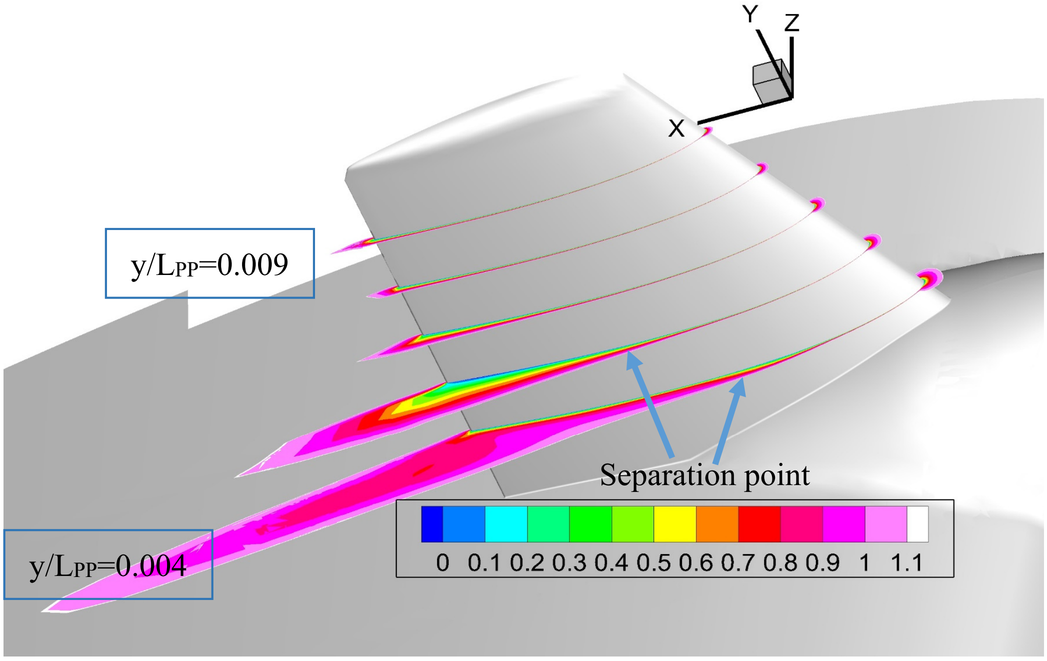

Figure 4- 28 Velocity sections along fin span-wise direction for NACAps6-sb6

($u/U_0 > 1.1$ flood contour was cut off)

From those figures, we can see that the low separation occurs almost on lower surface (upper surface in wing theory definition). Another point needs to be figured out is that the separation point (blue arrow in Fig. 4-22) is quite near the leading edge while the separation point is tended to move down to the trailing edge by NACA5412 (blue arrow in Figs. 4-27~4-28) even in comparison with the same angle of attack. It is undeniable that the effect of new fin-foil and shape of leading edge. Rounding the inlet corner reduces the extent of separation significantly. A "well-rounded" inlet almost eliminates flow separation (Philip et al. 2011).

The Figure 4-29 draws flow separation in 2D plane. Also, the streamline is added in order to see the backflow under fin surface. The flow angle of attack is larger in correspondence to a large flow separation and it is predicted that the largest flow separation mainly occurs around the section of y/L_{PP}=0.005 (fin's center in y-direction). This is the reason for which we need to change the flow attack angle.

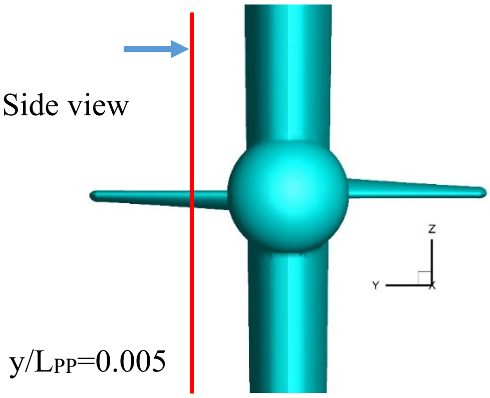

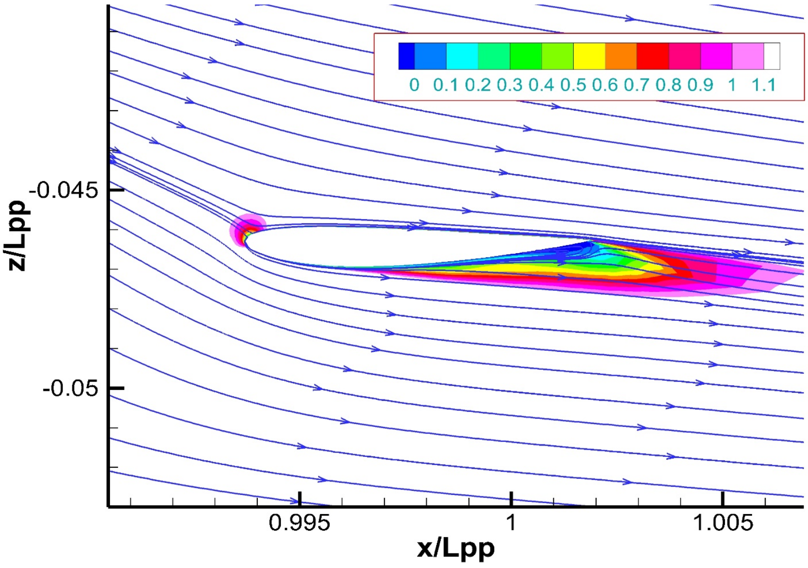

Original fin

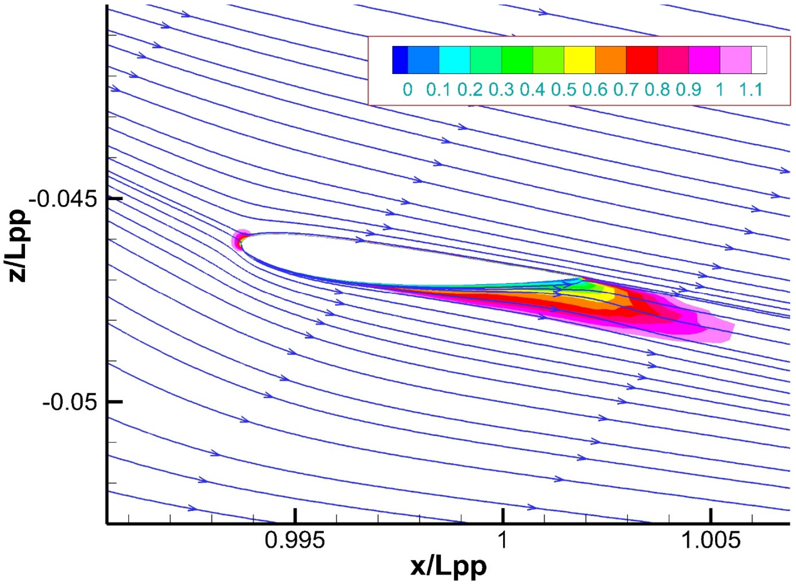

Ps0-sb6

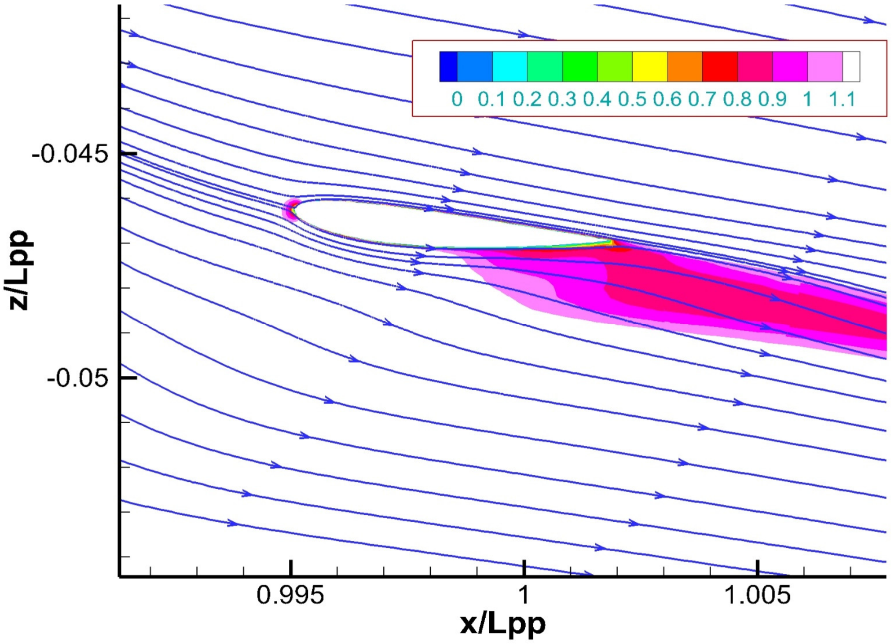

Cut0.007

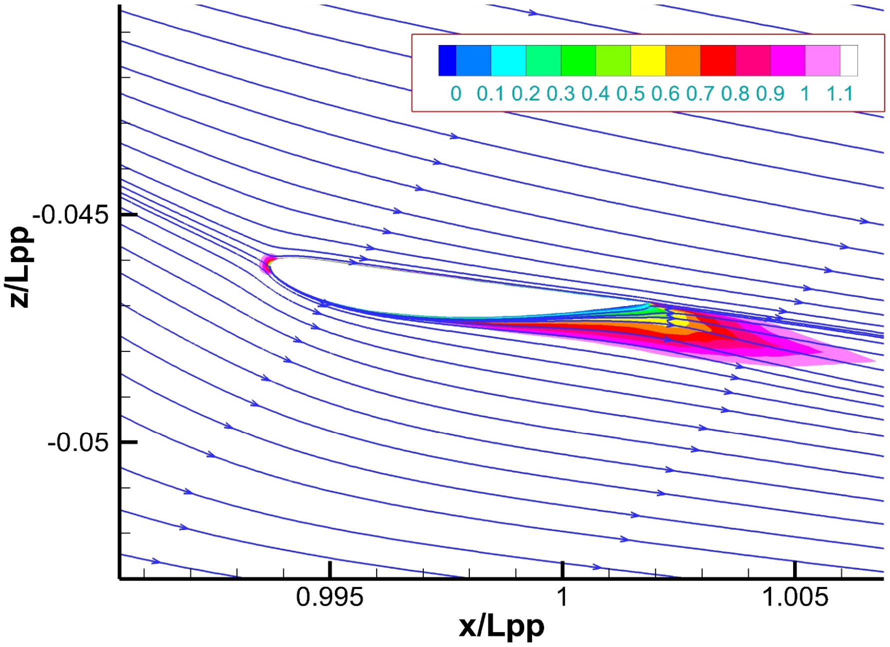

NACAps6-sb6

Figure 4- 29 Velocity contours and streamlines for starboard side

4.2.3 Trim and Sinkage

Computational sinkage (z/LPP) and trim for the KLVCC2 model at the fully loaded condition have been carried out for Froude number equals 0.142. Heave and pitch are obtained by measuring the displacements of two points located respectively close to the fore and the rear perpendiculars. The sinkage and trim with- and without propeller are defined in Fig. 4-30 and their values are shown in the following tables. The ship model is trimmed by bow-down ψ angle. The change of fin geometries is insignificant and hence it does not affect much to heave and pitch motions. The values of sinkage and trim are dependent on the length of ship (non-dimentionalized by LPP) and those values are for a part of the research.

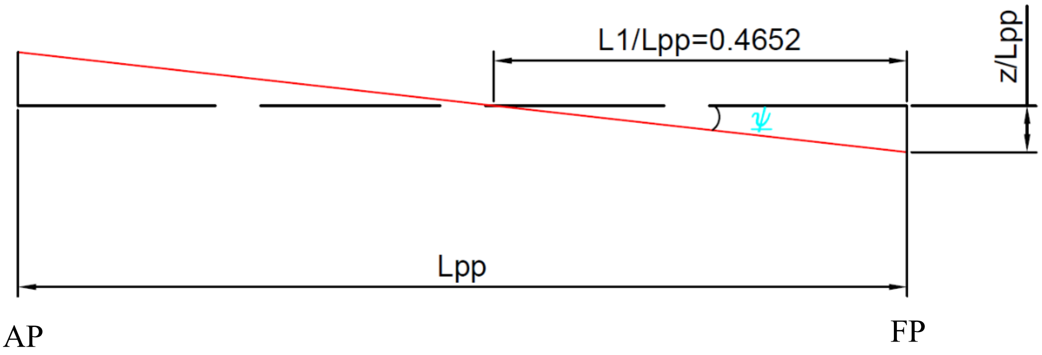

Figure 4- 30 Trim and sinkage condition of KVLCC2

Table 4- 5 Sinkage [with propeller]

Sinkage (z/LPP)		Angle of Attack (deg.) [port side]			
		-2	-1	0	1
Angle of Attack (deg.) [starboard side]	-2	-0.000976	-0.000973	-0.000976	-0.000978
	-1	-0.000979	-0.000976	-0.000976	-0.000978
	0	-0.000976	-0.000977	-0.000977	-0.000980
	1	-0.000974	-0.000978	-0.000978	-0.000978

Table 4- 6 Trim [with propeller]

Trim (rad.)		Angle of Attack (deg.) [port side]			
		-2	-1	0	1
Angle of Attack (deg.) [starboard side]	-2	-0.00205	-0.00205	-0.00206	-0.00204
	-1	-0.00203	-0.00203	-0.00205	-0.00204
	0	-0.00205	-0.00205	-0.00204	-0.00205
	1	-0.00203	-0.00205	-0.00202	-0.00204

Table 4- 7 Sinkage [without propeller]

Sinkage (z/L_{PP})		Angle of Attack (deg.) [port side]			
		-2	-1	0	1
Angle of Attack (deg.) [starboard side]	-2	-0.000950	-0.000962	-0.000951	-0.000963
	-1	-0.000962	-0.000963	-0.000963	-0.000955
	0	-0.000951	-0.000961	-0.000954	-0.000963
	1	-0.000954	-0.000961	-0.000957	-0.000962

Table 4- 8 Trim [without propeller]

Trim (rad.)		Angle of Attack (deg.) [port side]			
		-2	-1	0	1
Angle of Attack (deg.) [starboard side]	-2	-0.00220	-0.00217	-0.00219	-0.00217
	-1	-0.00217	-0.00217	-0.00217	-0.00219
	0	-0.00219	-0.00217	-0.00219	-0.00217
	1	-0.00219	-0.00217	-0.00217	-0.00217

4.2.4 Pressure Distribution

Wide understanding related to pressure problem is one of the keys for designers to develop new projects. The pressure is the most dynamic variable in fluid mechanics; of course following the velocity. Pressure drag is caused by the different pressure along upper and lower fin surfaces as it travels through the fluid. The Figs 4-31 ~ 4-36 show the pressure distribution on the rudder-fin surface of those cases and it can be observed that those pictures display two high-pressure regions near the leading edge of the rudder as well as two high-pressure areas on the upper starboard surface and the lower port side fin surface which correspond to the axial inlet velocities. In general, the negative pressure on those surfaces dissipated when changing the attack angle to meet the efficient working angle. The normal fin and NACAps0_sb0 cases have the strong negative-pressure (blue region) on the upper port side and lower starboard side; on the other hand, the negative pressure on those surfaces dissipated in the case of NACAps0_sb6 and especially NACAps6_sb6 on both sides. The low-pressure region is small and therefore considerable changes in drag; in other words, the dissipation of negative pressure is the cause of improvement of propulsive efficiency.

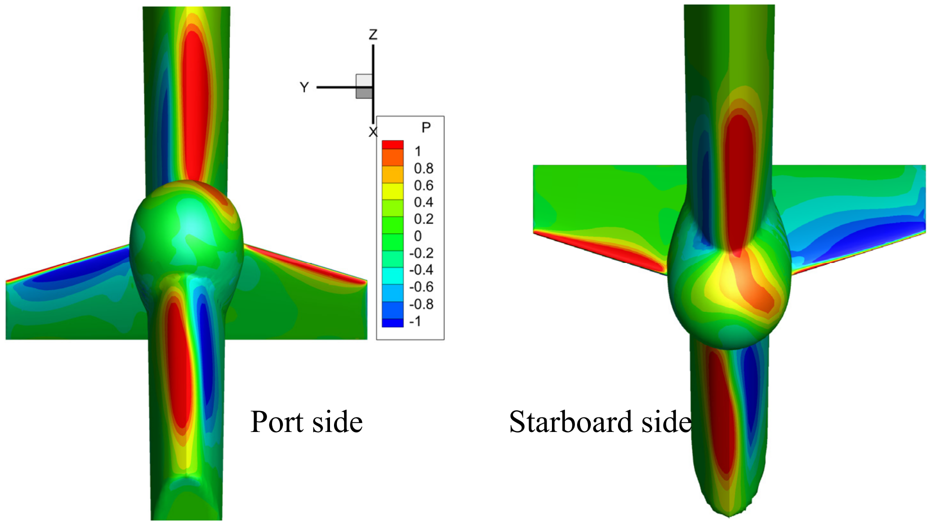

Figure 4- 31 Pressure distribution on rudder-fin surface for normal fin

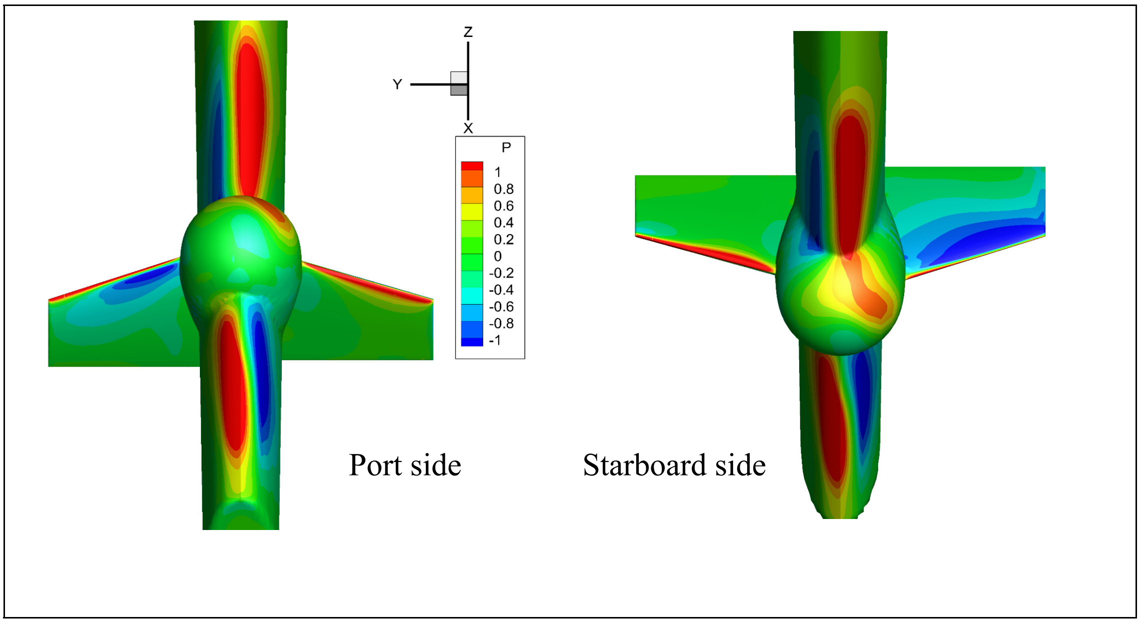

Figure 4- 32 Pressure distribution on rudder-fin surface for ps0-sb6

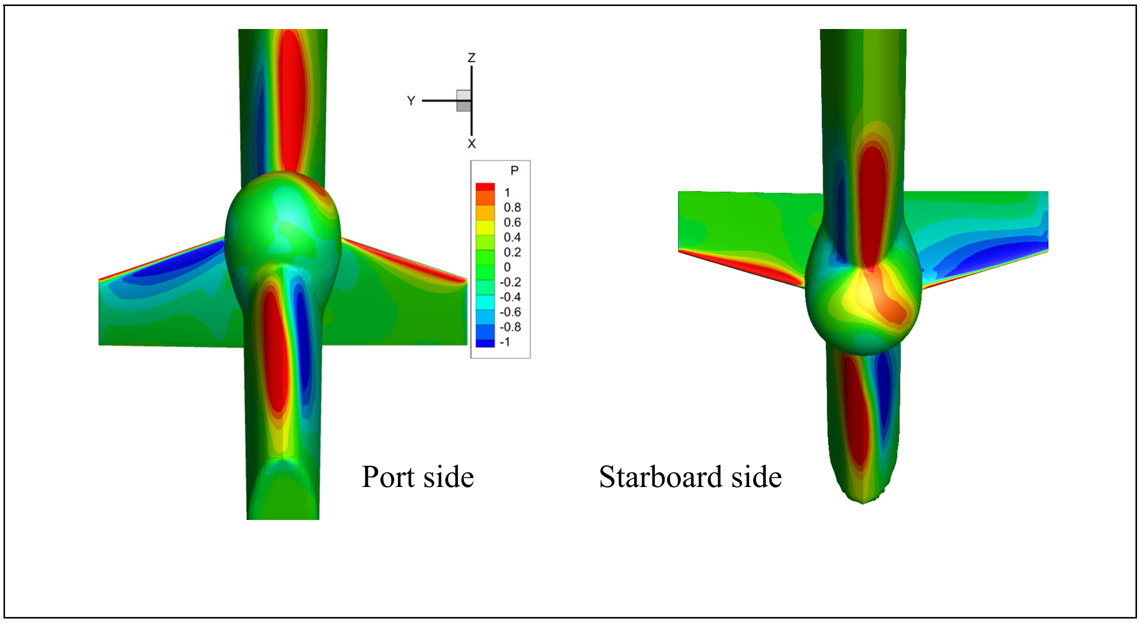

Figure 4- 33 Pressure distribution on rudder-fin surface for twisted fin

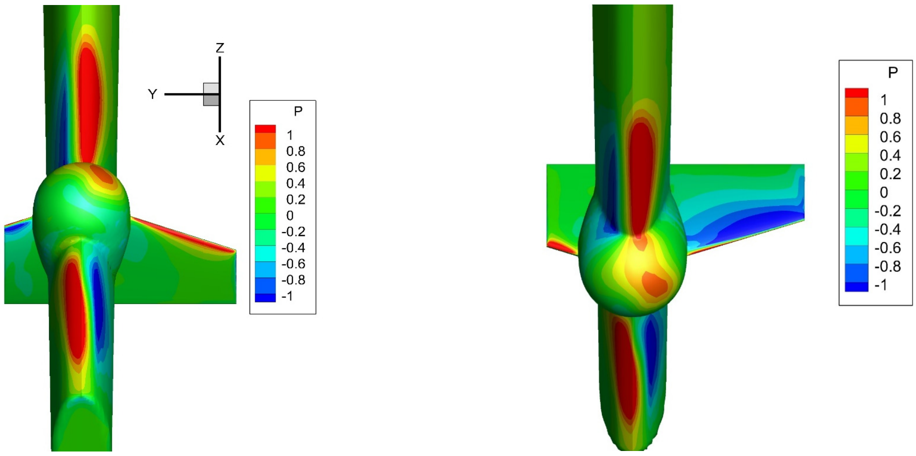

Cut0.005

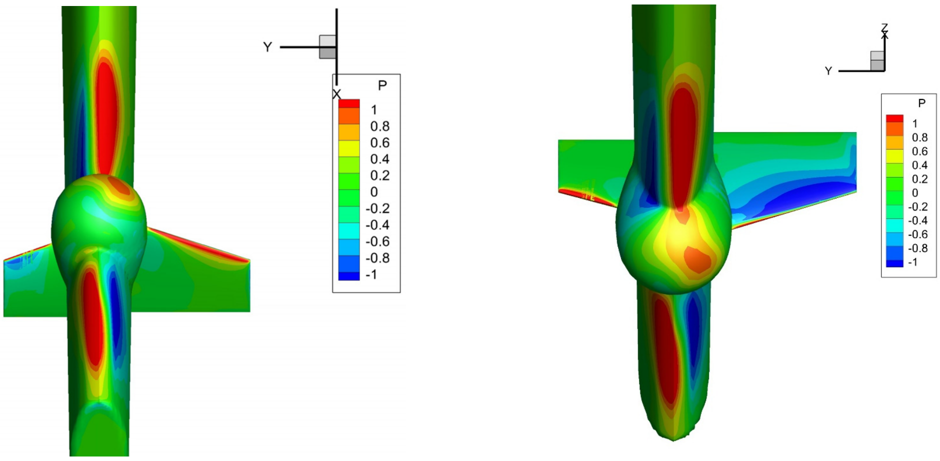

Cut0.007

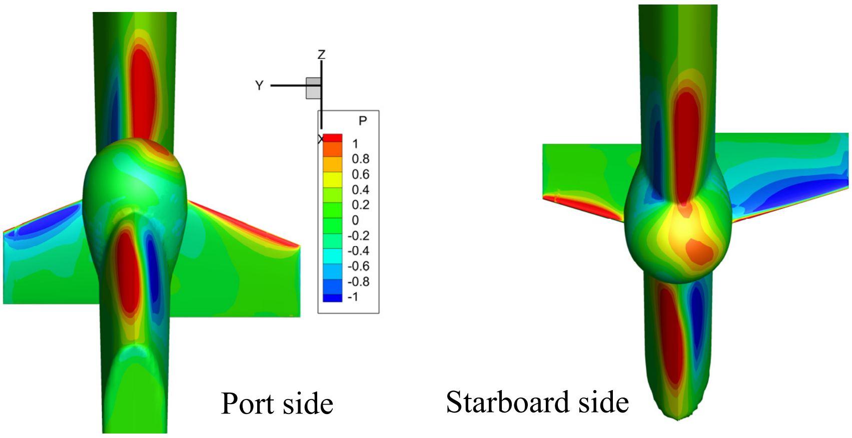

Cut0.008

Figure 4- 34 Pressure distribution on rudder-fin surfaces for cutting starboard side

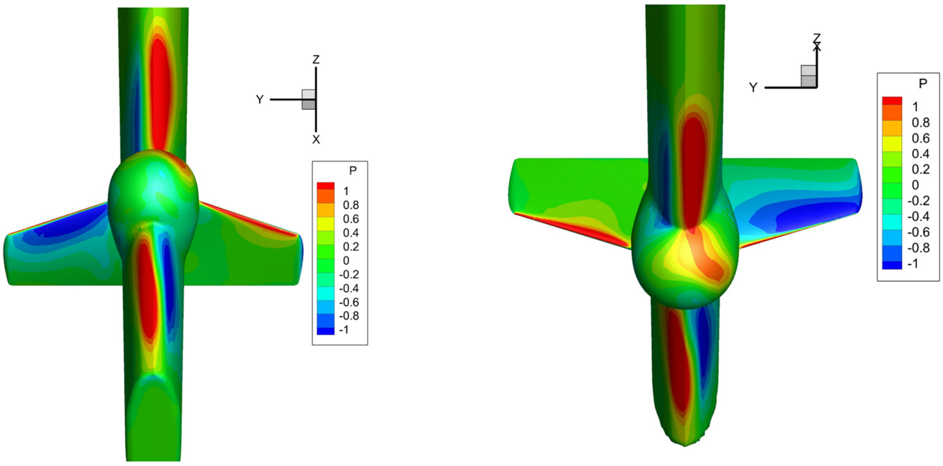

NACAps0_sb0

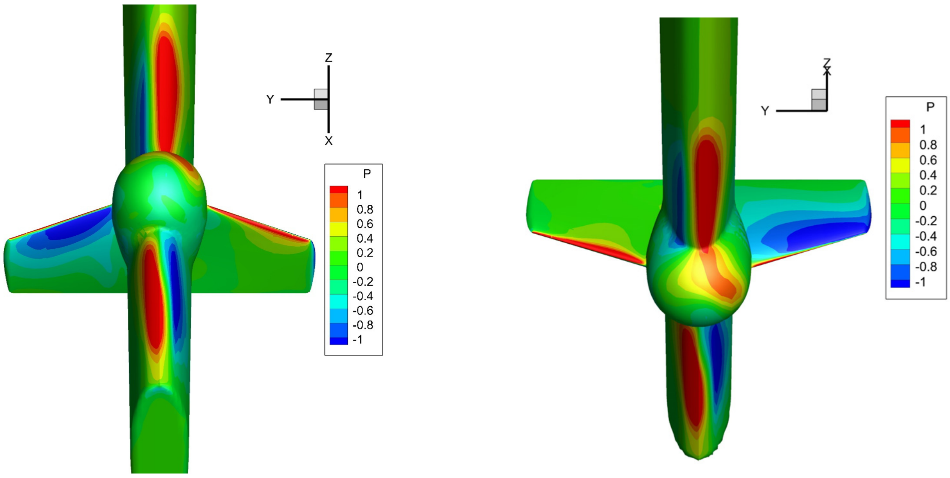

NACAps0_sb1

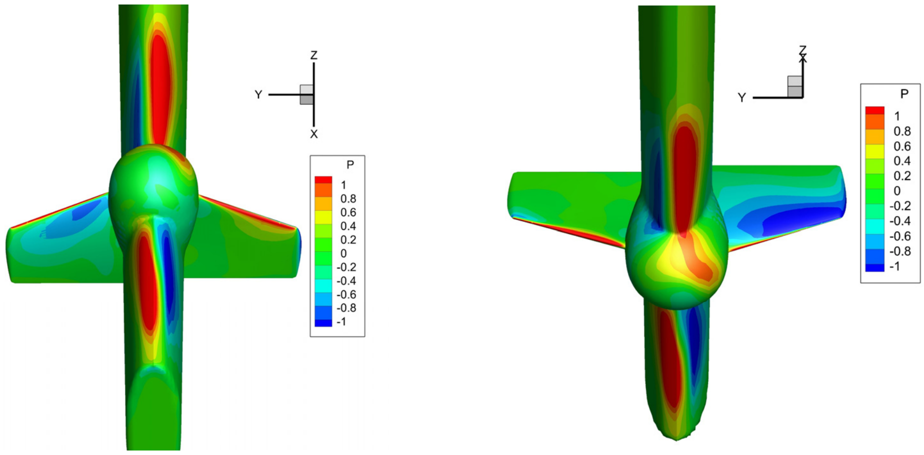

NACAps0_sb6

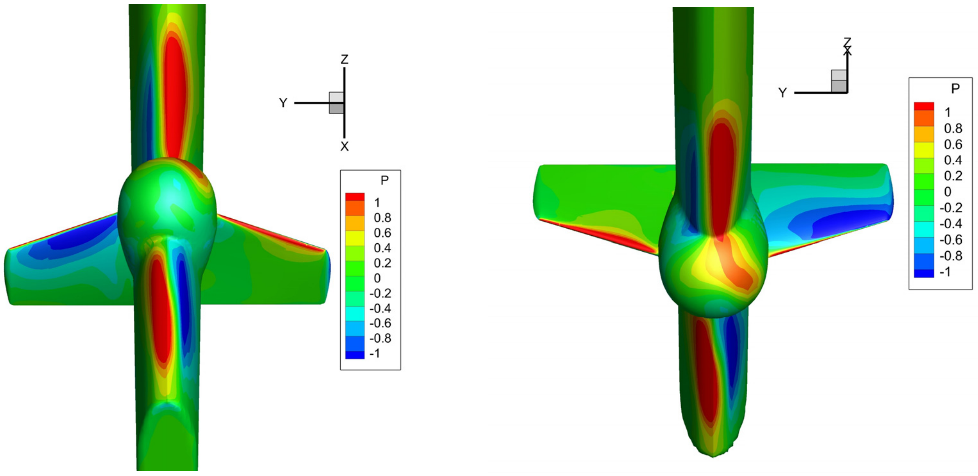

NACAps1_sb1

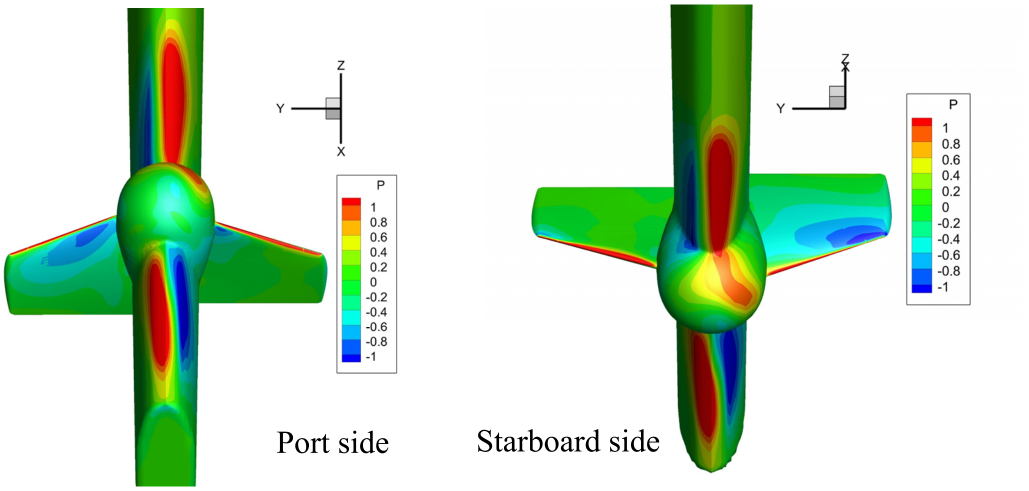

NACAps6_sb6

Figure 4- 35 Pressure distribution on rudder-fin surfaces for NACA5412

The pressure distribution around the bulb head for cutting starboard side case (Fig. 4-34) and new positions of fin cases (Fig. 4-36) are smaller than the others. The flow was accelerated by propeller and probably hit the rudder-bulb first. Like the effect of the different hull aft end shapes, the different fin geometries lead to different wake distribution. The exit flow at downstream (fin position) is shifted in different form from others since shape of fin (cutting for starboard) and location of fin was changed.

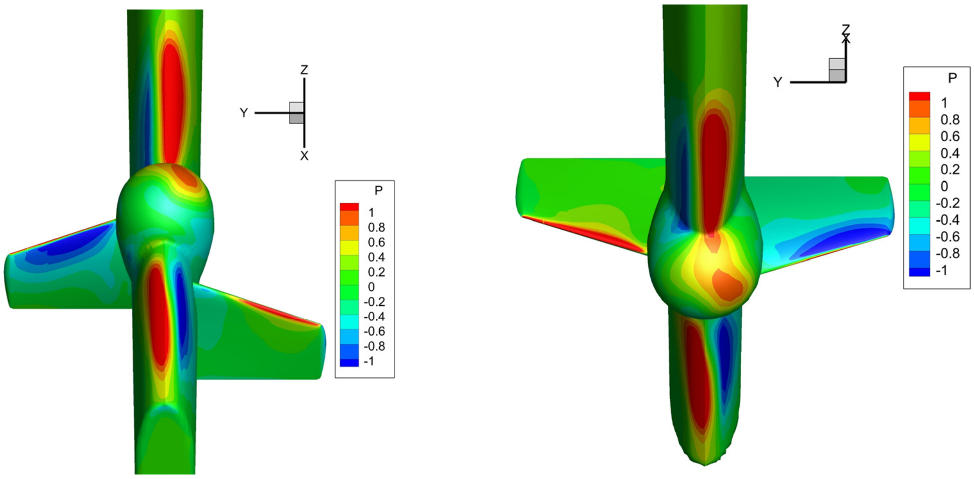

NACAps0-sb0_0.004z0.003x

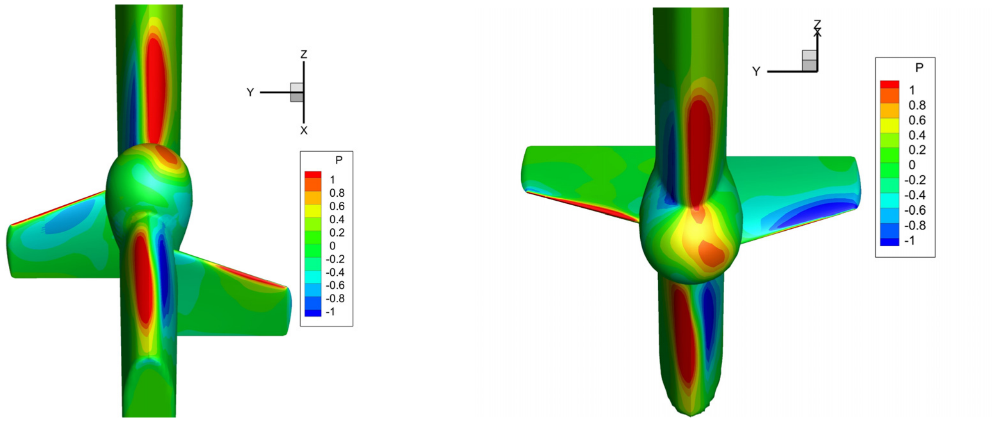

NACAps0-sb6_0.004z0.003x

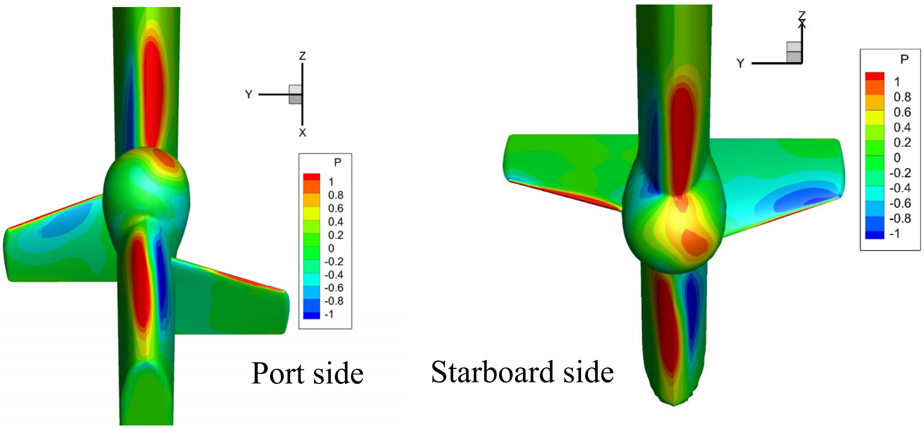

NACAps6-sb6_0.004z0.003x

Figure 4- 36 Pressure distribution on rudder-fin surfaces for new position of fin

4.2.5 Vortex Shedding

S_{ij} is known as the rate-of-strain tensor and Ω_{ij} is the vorticity tensor. The Q-Criterion is one of the three invariants of the velocity gradient tensor and obtained by Eq. 26, written below. The Q-criterion represents the local balance between shear strain rate and vorticity magnitude, defining vortices as areas of which the strain-rate magnitude is smaller than the magnitude of vorticity.

$$S_{ij} = \frac{1}{2}\left(\frac{\partial u_i}{\partial x_j} + \frac{\partial u_j}{\partial x_i}\right) \tag{24}$$

$$\Omega_{ij} = \frac{1}{2}\left(\frac{\partial u_i}{\partial x_j} - \frac{\partial u_j}{\partial x_i}\right) \tag{25}$$

$$Q = \frac{1}{2}\left(\left|\overline{\Omega_{ij}}\right|^2 - \left|\overline{S_{ij}}\right|^2\right) \tag{26}$$

In order to understand the turbulence structure, the structures are illustrated in Figs. 4-37 ~ 4-40 using the Q-Criterion with Q=5000 colored according to axial velocity contours for conventional rudder, normal fin, NACAps0_sb0 and NACAps6-sb6_0.004z0.003x. The Q-Criterion iso-surface is visualized only for those cases because the Q-Criterions are not large difference among cases in the same group. The main turbulence structure to be captured well in the simulation. Due to the use of average effect in body-force model of the propeller, only the ring-shape can be seen in the following figures. The tip-vortex shedding can be only created by real propeller as mentioned by Win et. al (2014). However, one of the feature is that the body-force propeller included the rotating hub, hence the hub vortex can be seen. It is clearly seen that the hub vortex was split by the fins. However, the port side fin does not affect to the main port hub vortex (arrow in red). The port side fin location is observed that higher than the position of port hub vortex. The bigger hub means the propulsion energy of the propeller decreases. This is reason why the port side fin was moved to new location in order to minimize the effect of hub vortex.

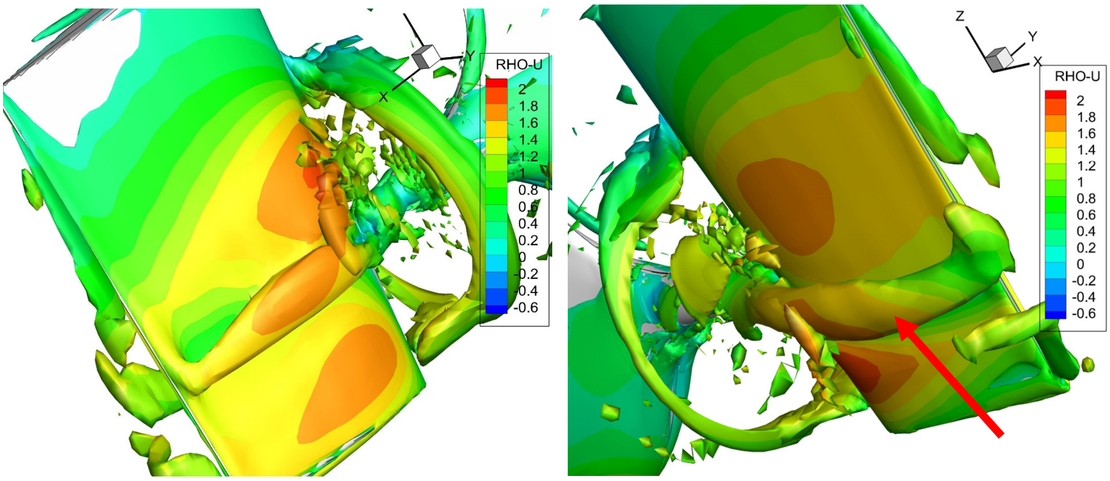

Figure 4- 37 Turbulence structures of flow around stern for conventional rudder [left for starboard side and right for port side]

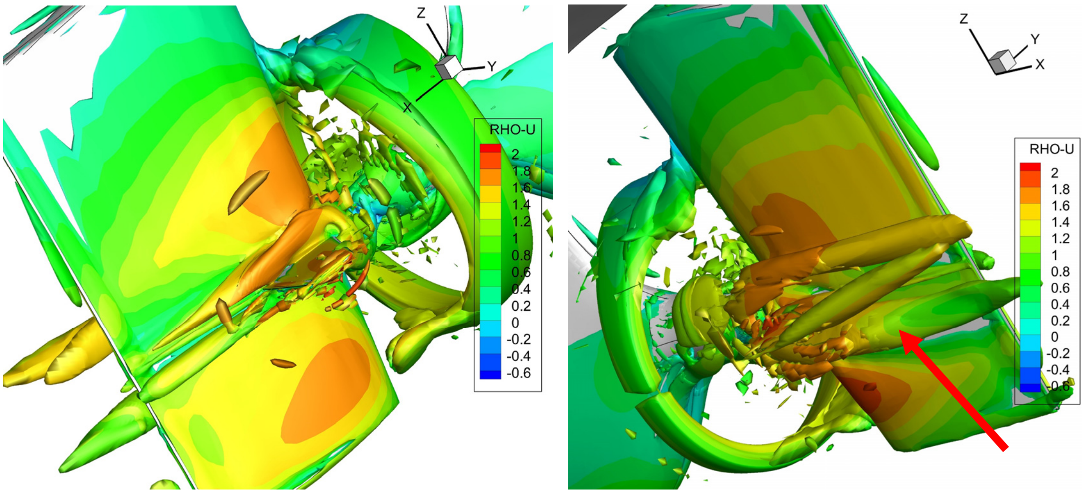

Figure 4- 38 Turbulence structures of flow around stern for ps0-sb0 [left for starboard side and right for port side]

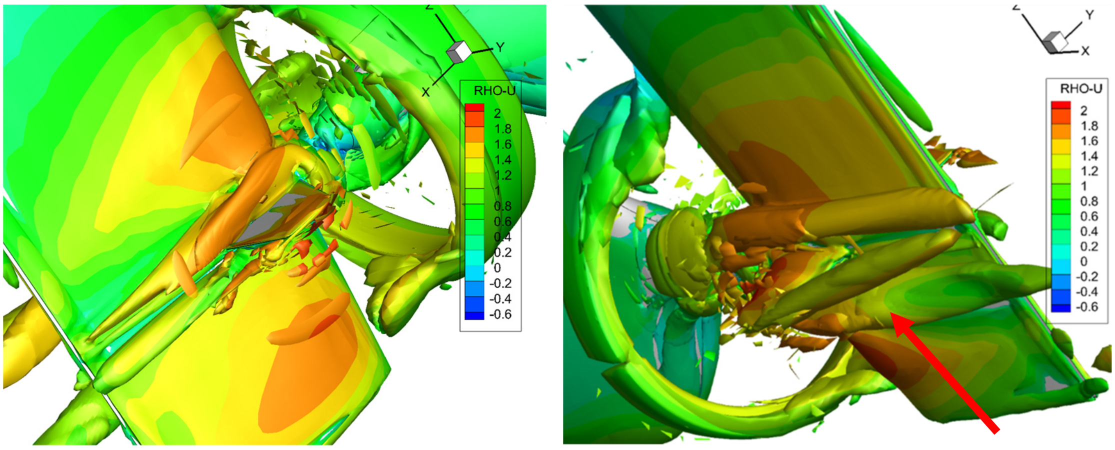

Figure 4- 39 Turbulence structures of flow around stern for NACAps0_sb0 [left for starboard side and right for port side]

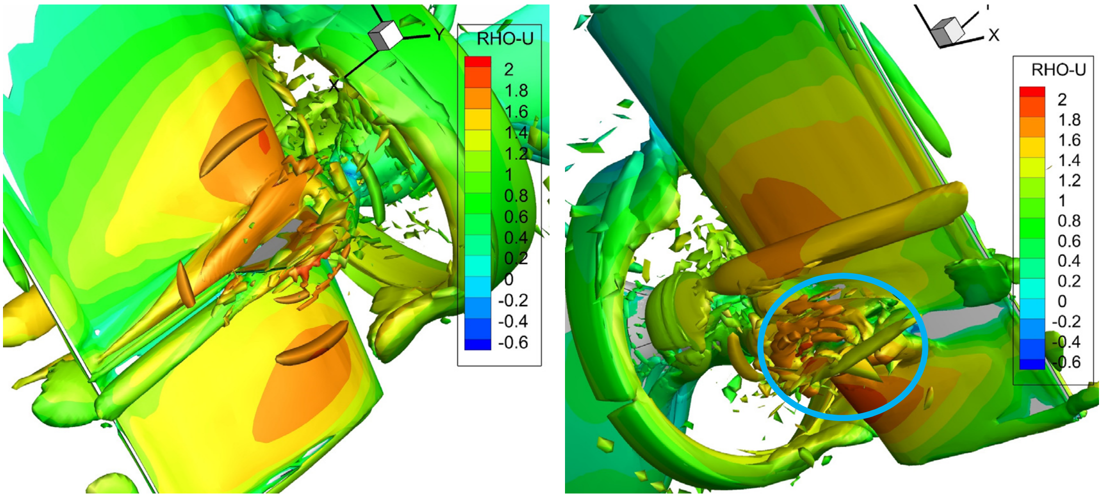

Figure 4- 40 Turbulence structures of flow around stern for NACAps6-sb6_0.004z0.003x [left for starboard side and right for port side]

The main hub vortex was totally eliminated by the new position of port side fin which is clearly seen in Fig. 4-40 (circle in blue). Thus, the port side fin plays two important roles; one is providing the lift into ship power and the other is splitting the hub vortex. From that point of view, changing the position of port side fin or adding small fin on port side (in which the hub vortex is located) are necessary to make the fluid flows smoothly.

CHAPTER 5: CONCLUSIONS AND FUTURE WORKS

5.1 Conclusions

The energy-saving device studied in the present work was a bulbous rudder appended with a pair of horizontal fins applied to KVLCC2 tanker in calm water condition. Several cases with different fin geometries had been designed and hundreds of simulations had been simulated using CFDShip-Iowa version 4.5 code and carried out by the Linux Cluster with 124 processors (in total 756GB physical memory (7 nodes)). Intel Fortran compiler and OpenMPI are used for parallel computation. The body-force propeller model which provides the propulsive force for the ship was used throughout this research. The numerical results including flow field and self-propulsion factors had been validated by experimental data for conventional rudder (in the absence of fin) and normal fin cases. The improvements of rudder-bulb-fin system were also designed and simulated, hence the best designs for each group of improvement were investigated. In some cases, the numerical result has not been validated by EFD but the accuracy of the numerical method for the similar object (e.g., ps0-sb1, ps0-sb6, cut0.008, twisted fin), had already been proved by comparing with the experimental data which were shown in some sections of this dissertation.

The following points are the result of summarization the salient features for each group in this research:

- The thrust deduction factor of rudder-fin case increases around 2% compared with the conventional rudder case. The detailed flow was further analyzed around the fins. The obvious tip vortex shedding was found on the port side fin. The hub vortex was twisted toward the port side under the bulb-fin. A huge flow separation was observed below the starboard side. In general, the result of rudder-fin shows more benefit than those of conventional rudder through this research in all aspects; in others word, the rudder-bulb-fin system should be installed on vessels as an energy-saving device to improve the quasi-propulsive coefficient. One more advanced feature is that the system is not only for new ship but can be also easily applied to existing vessels.

- Through the detailed CFD flow field analysis, the larger extra thrust and smaller flow separation were discovered on the optimal design. The variation of flow attack angle along the foil span-wise was found, large flow separation regions occurred under the starboard fin around the middle span. It becomes smaller near the tip and the root. The best energy-saving effect, 2.3% total resistance reduction, had been found by changing the angle of attack of the fin. The changing angle is zero degree for port side and rotated 1-degree up for starboard.
- The designs of high changing attack angle (6-degree) and twisting fin cases could be enhanced higher hull efficiency by reducing the wake factor and raising the thrust deduction factor (1-*t*), hence a result of increasing the propulsion performance. Although, the twisting fin proved as one of the best designs through self-propulsion factors, the application to real ship faced to difficult problem in the process of designing and constructing.
- The new geometry of rudder-fin on changing length of starboard fin had been designed and simulated. The results proved that the shorter starboard fin length brings more benefit into thrust; namely the resistance reduced and the hull efficiency

increased in comparison with normal fin. That is a good point on the way reducing propulsive losses. The wetted area is slightly decreased by making shorter the length of starboard fin which directly effects to total resistance.

- The research again pointed out that the fin-foil and attack angle have a large effect on generating lift by horizontal fins, namely NACAps6-sb6, hence a results of increasing the propulsion performance. The total resistance of NACAps6-sb6 case with propeller could be reduced by 4.36 percent with changes in increasing of (*1-t*) factor, 5.25% and decreasing of (*1-w*) factor by 0.78 percent. Thus, the hull efficiency value of NACAps6_sb6 is highest thus far, in comparison with normal fin.
- Inside the propeller disk area, the hub vortex is generated by the propeller acceleration flow, mainly shifted to the port side and other vortexes appear on the starboard side of rudder. From that point of view, this problem can be completely solved by a design of new position of port side fin. The main hub vortex was eliminated by the new position of port side fin. The port side fin plays two important roles; one role is creating the thrust into ship power and the other is splitting the hub vortex.

5.2 Future works

The conclusions have been summarized the salient features of the research in the section above whilst this part points out necessary things that need to be done in the near future. By combining of theoretical fluid mechanics and the analyzed data presented in this dissertation, the future works have been proposed. Generally, each design related to attack angle, shorter starboard fin and using new mean camber line in this dissertation brings back the benefits via a certain way. Thus, a design with a combination among those features is one of the best, most functional methods on the path of conquering the optimal designs. In addition, although the new position of fin case has not proved yet as one of the best energy-saving devices through self-propulsion factors, the hub vortex is totally truncated by the port side fin. From this point of view, the original position of port side fin should be kept and added small fin at new fin's position (in which the main hub vortex located) in order to totally eliminate the hub vortex.

As is well known, there are many kinds of energy-saving devices around ship stern are developed with different method approach and its advantages are also proven. Since the improvements of energy-saving device are always necessary, a combination design among energy-saving devices is bearing in author's mine. It can be the combination between a rudder-bulb-fin system and a duct before the propeller, a system with cap-fins on propeller boss and a rudder-fin system. Those designs can be even tested on another kinds of ships.

Finally, since the condition in this study is for calm water, it is necessary to be tested in another conditions, for example in waves by both CFD and EFD.

REFERENCES

Anthony F. Molland, Stephen R. Turnock, Dominic A. Hudson (2011), “Ship Resistance and Propulsion”, Cambridge University Press.

Choi, YB (2008) "Energy Saving Devices," *SNAME Tech Section 2008-2009*, Greece.

Dinham, PT, Ahn, H, Banks, J, Hinatsu, M, Khorasanci, M, Lee, I, Perlin, M, Takai, M, D (2017) “The specialist Committee on Energy Saving Methods”, *Proceedings of 28th ITTC*, Vol II, 661-720.

Hoang CL (2009), “Effect of air lubrication method on frictional resistance reduction in real ship experiment”, *Doctoral Dissertation*, Graduate School of Engineering, Osaka University.

Ira H. Abbott and Albert E. Von Doenhoff (1949) “Theory of Wing Sections”, Dover Publications, INC, New York.

International maritime Organization (IMO). Buhaug, Corbett, J.J., Eyring, V., Endresen, Faber, J., Hanayama, S., Lee, D.S., Lee, D., Lindstad, H., Markowska, A.Z. and Mjelde, A., 2009. “Second IMO GHG study” IMO, London, UK.

Kawakita, C, Takashima, R, and Sato, K (2012) "CFD on Cavitation around Marine Propellers with Energy-Saving Devices," *MHI Tech Review*, 49(1), 63-67.

Kajihama, T, Okada, Y, Okazaki, A, Katayama, K, and Tachikawa, T, (2016) "Innovative energy saving device designed by virtual prototyping method," *10th Symp on High-Performance Marine Vehicles*, HIPER’16.

Kim, JH, Choi, JE, Choi, BJ, and Chung, SH (2014) "Twisted Rudder for Reducing Fuel-Oil Consumption," *Int J Nav Archit and Ocean Eng*, 6, 715-722.

Kishi Junichiro (2018) “The EFD and CFD Study on various Rudder-Bulb-Fin System in Ship and Propeller Wake Field”, *Master Thesis*, Graduate School of Engineering, Osaka University.

Matsumoto, D and Sakamoto, T (2009) “Finned Rudder”, Patent EP2110311A3

Nguyen, TV, Ikeda, Y (2016) “Hydrodynamic Characteristics of High Lift Rudders with Wedge Tails,” *Asia-Pacific Hydrodynamics conf,* AP-hydro, Hanoi, 238-245.

Paterson, EG, Wilson, RV, and Stern, F (2003) "General-purpose parallel unsteady RANS ship hydrodynamics code: CFDSHIP-IOWA," *IIHR Technical Report* No. 432.

Philip J.Pritchard (2011), “Fox and Mcdonald’s Introduction to Fluid Mechanics”, The 8th edition, John Wiley and Sons, Inc

Simonsen, C and Stern, F (2005) "RANS Maneuvering Simulation of Esso Osaka with Rudder and a Body-Force Propeller", *Journal of Ship Research*, Vol.49(2), 98-120.

Wilson, R, Carrica, PM, and Stern, F (2006) "Unsteady RANS method for ship motions with application to roll for a surface combatant," Computers and Fluids, 35, 501-524.

Truong TQ, Toda Y (2019) “The CFD and EFD Study of Rudder-Bulb-Fin System in Changing Cambered Foil and AOA Applied to KVLCC2 Tanker”, *The 11th International Workshop on Ship and Marine Hydrodynamics*, IWSH, Hamburg, Germany.

Truong TQ, Ogawa S, Toda Y (2019) “Improvement of Rudder-Bulb-Fin System”, *The Japan Society of Naval Architects and Ocean Engineers, JASNAOE*, Nagasaki, Japan

Truong TQ, Wu PC, Kishi J, Toda Y (2018) “Improvement of Rudder-Bulb-Fin System in Ship and Propeller Wake Field of KVLCC2 Tanker in Calm Water,” *Proceedings of 28th International Offshore and Polar Engineering Conference, Hokkaido, ISOPE*, Vol III, 184-190

Truong TQ, Wu PC, Aoyaki K, Koike K, Akiyama Y and Toda Y (2017) “The EFD and CFD Study of Rudder-Bulb-Fin System in Ship and Propeller Wake Field of KVLCC2 Tanker in Calm Water”, *Proceedings of 27th International Offshore and Polar Engineering Conference*, San Francisco, ISOPE, 823-830

Tokgoz E (2015), “A CFD study on the Propeller-Hull Interaction Flow in Waves using Body-Force Distribution Model”, *Doctoral Dissertation*, Graduate School of Engineering, Osaka University.

Win YN (2014), “Computation of the Propeller-Hull and Propeller-Hull-Rudder Interaction Using Simple Body-Force Distribution Model”, *Doctoral Dissertation*, Graduate School of Engineering, Osaka University.

Yan Naing Win, Ping-Chen Wu, Keisuke Akamatsu, Hiroshi Okawa, Frederick Stern, Yasuyuki Toda (2016), “RANS Simulation of KVLCC2 using Simple Body-Force Propeller Model with Rudder and without Rudder”, *Journal of the Japan Society of Naval Architects and Ocean Engineers*, Volume 23, 1-12.

Hori Masatoshi (2017), “数値計算技術を利用した船舶省エネルギー装置の設計手法に関する研究”, *Doctoral Dissertation*, Graduate School of Engineering, Osaka University.

Munehiko Hinatsu (2015)、“船舶における省エネ技術について”、生産と技術　第67　第2号

Webpage https://www.pointwise.com/

Webpagehttps://global.kawasaki.com/en/mobility/marine/technology/energy_saving.html.

Webpage https://www.nakashima.co.jp/eng/product/ultimate_rudder.html

Webpage http://www.simman2008.dk/KVLCC/KVLCC2/tanker2.html

APPENDIX A: Comparison between CFD and EFD

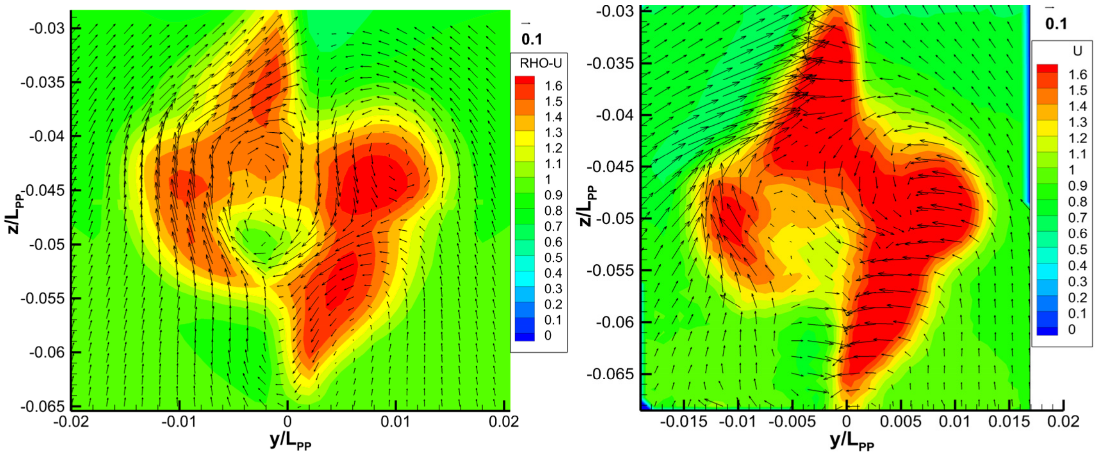

Appendix A- 1 Flow field at x/L_{PP}=1.025 comparison between CFD and EFD for ps0-sb1

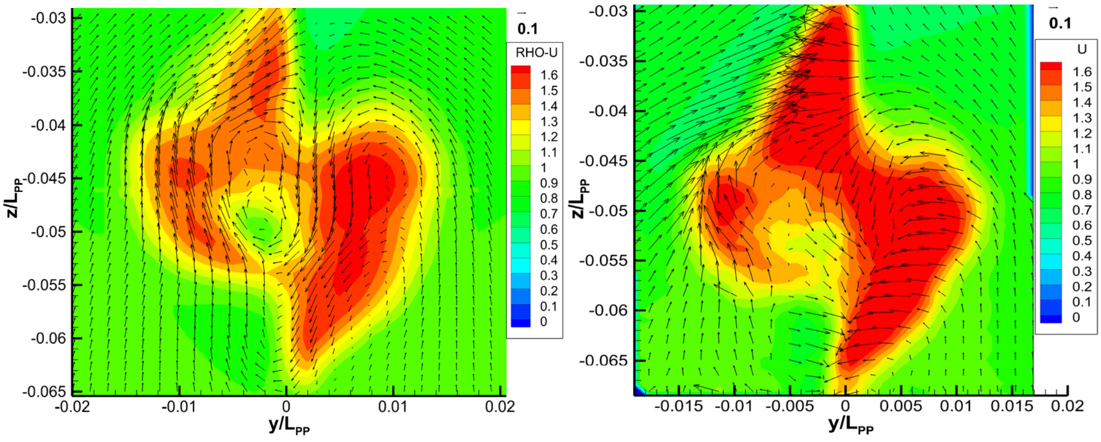

Appendix A- 2 Flow field at x/L_{PP}=1.025 comparison between CFD and EFD for ps0-sb6

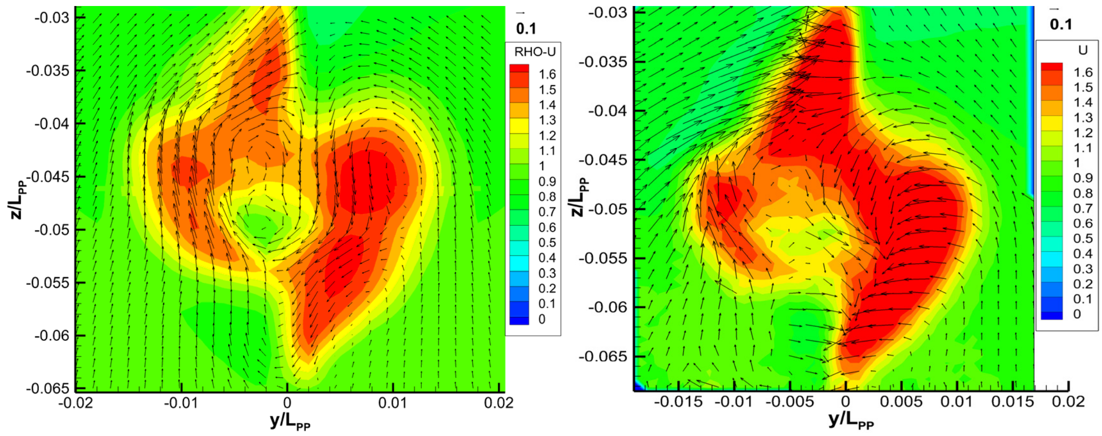

Appendix A- 3 Flow field at x/L_{PP}=1.025 comparison between CFD and EFD for cut0.008

APPENDIX B: Flow separation on various sections [starboard side]

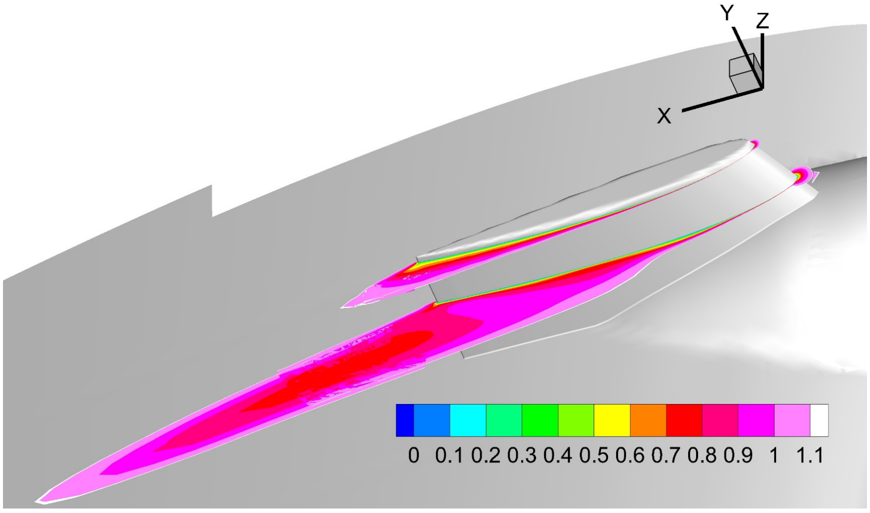

Appendix B- 1 Velocity sections along fin span-wise direction for cut0.005

(u/U$_0$>1.1 flood contour was cut off)

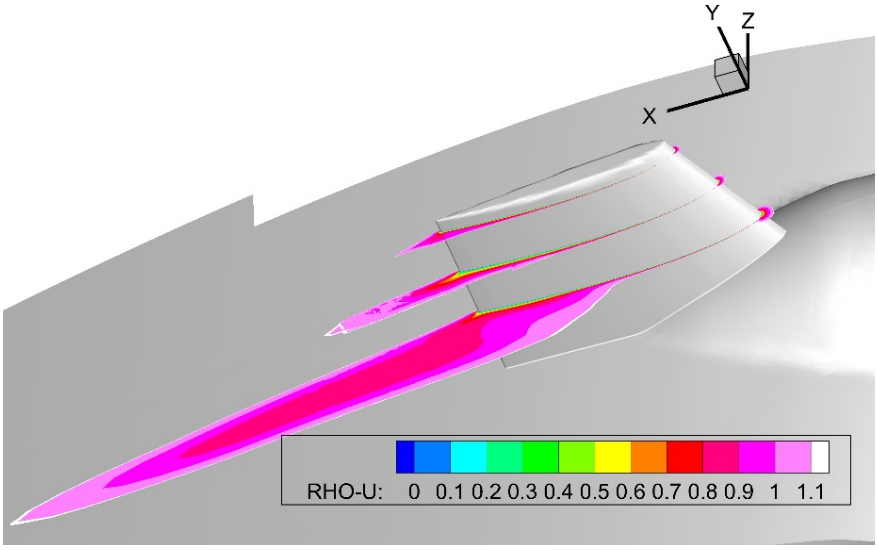

Appendix B- 2 Velocity sections along fin span-wise direction for cut0.007

(u/U$_0$>1.1 flood contour was cut off)

ACKNOWLEDGEMENTS

First and foremost, I would like to express my sincere gratitude to my supervisor, Professor Yasuyuki Toda for giving me a chance to become one of the students of Osaka University in general as well as to work in this research in particular; always supports me with his knowledge, patience, and kindness, without his guidance and persistent help this project could not have been possible. I also would like to thank all the professors in our Department of naval Architecture and ocean Engineering for sharing their valuable knowledge, especially the committee members and professors; Prof. Toda, Prof. Suzuki, Prof. Hinatsu, and Prof. Umeda who reviewing this paper and giving valuable comments.

I also appreciate the support and unending love from all members in our laboratory and especially Assistant Prof. Ping-Chen Wu for spending his time to help me and a shoulder on which to learn in the early stages of this research.

Many thanks must also be conveyed to the Ministry of Education, Culture, Sports, Science and Technology Japan (MEXT) scholarship which has supporting me financially for this project.

Last but not least, the author wishes specially to thank my family and friends because of their cooperation and mental support during my research time.

LIST OF PUBLICATIONS

Truong TQ, Toda Y (2019) “The CFD and EFD Study of Rudder-Bulb-Fin System in Changing Cambered Foil and AOA Applied to KVLCC2 Tanker”, The 11th International Workshop on Ship and Marine Hydrodynamics, IWSH, Hamburg, Germany

Truong TQ, Ogawa S, Toda Y (2019) “Improvement of Rudder-Bulb-Fin System”, The Japan Society of Naval Architects and Ocean Engineers, JASNAOE, Nagasaki, Japan

Truong TQ, Wu PC, Kishi J, Toda Y (2018) “Improvement of Rudder-Bulb-Fin System in Ship and Propeller Wake Field of KVLCC2 Tanker in Calm Water,” Proceedings of 28th International Offshore and Polar Engineering Conference, Hokkaido, ISOPE, Vol III, 184-190

Truong TQ, Wu PC, Aoyaki K, Koike K, Akiyama Y and Toda Y (2017) “The EFD and CFD study of Rudder-Bulb-Fin System in Ship and Propeller Wake Field of KVLCC2 Tanker in Calm Water,” Proceedings of 27th International Offshore and Polar Engineering Conference, San Francisco, ISOPE, 823-830.

Ping-Chen Wu, Truong Quang Tho, Aoyagi K, Koike K, Akiyama Y, Toda Y (2016), “The EFD and CFD study of the bulbous rudder with asymmetric horizontal fins with different angles of attack in ship and propeller wake field of KVLCC2 tanker”, Asia-Pacific Hydrodynamics conference, Hanoi, Vietnam, September, (as a presenter).

CURRICULUM VITAE

Education

Doctoral Course, Naval Architecture and Ocean Engineering 2016 – present

Osaka University – Japan

Adviser: Prof. Yasuyuki Toda

Areas of research: Ship resistance and propulsion, Computational fluid dynamics

Current topic: A study on rudder-bulb-fin system applied to KVLCC2 in calm water

Scholarship by MEXT (Japanese government scholarship) (2016-2019)

Master Degree, Naval Architecture and Ocean Engineering 2016

Osaka University – Japan

Adviser: Prof. Yasuyuki Toda

Areas of research: Ship resistance and propulsion, Computational fluid dynamics

Topic: The EFD and CFD study of the bulbous rudder with asymmetric horizontal fins with different angles of attack in ship and propeller wake field of KVLCC2 tanker

Scholarship by MEXT (Japanese government scholarship) (2014-2016)

Bachelor Degree, Ship Engineering and Fluid Mechanics 2014

Hanoi University of Science and Technology – VietNam

Topic: Establishing technology process for 12500-ton cargo ship

Work Experience

2012.3 – 2012.8	Collaborator (part-time) at Hanoi transportation company
2013.2 – 2013.5	Internship at Hanoi shipbuilding joint-stock company
2017.4 – 2017.9	Teaching Assistant (part-time) at Osaka University